Design of porous nanostructured solid catalysts

Abildstrøm, Jacob Oskar

Publication date:
2016

Document Version
Publisher's PDF, also known as Version of record

Design of porous nanostructured solid catalysts

Department of Chemistry

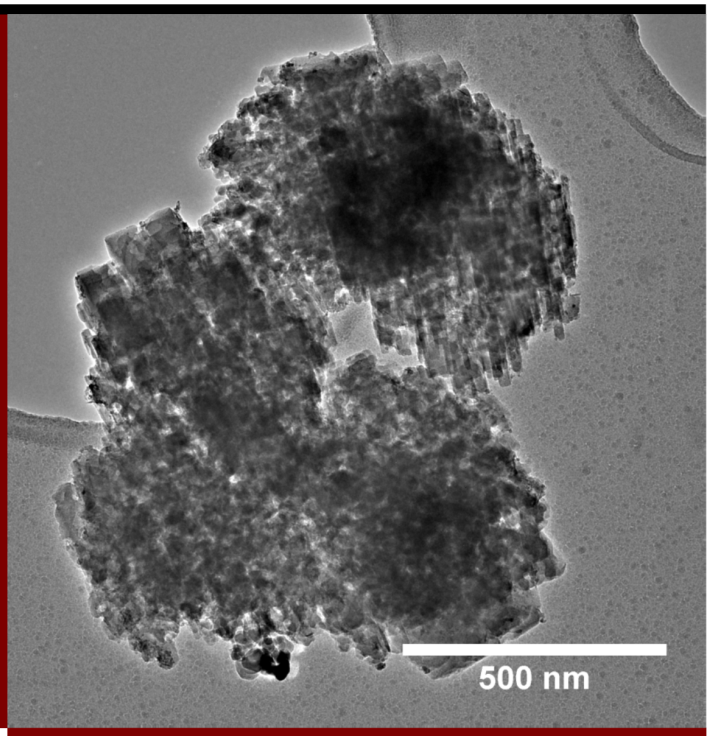

Written by Jacob Oskar Abildstrøm
DTU Chemistry – PhD Thesis
November 2016

DTU Chemistry
Department of Chemistry

Preface

This thesis is submitted in candidacy for the Ph.D. degree from the Technical University of Denmark (DTU). The thesis is based on work carried out at the Centre for Catalysis and Sustainable Chemistry (CSC) at DTU Chemistry, from March 2013 to November 2016 under supervision of Associate Professor Søren Kegnæs and Professor Anders Riisager. The project was funded by the Danish National Research Foundation and the Technical University of Denmark.

I am grateful to have had Associate Professor Søren Kegnæs as my supervisor. Through knowledgeable and friendly guidance, the years spent in his group have not only been with a purpose to grow as a scientist, but also as a human. I would also like to thank Professor Anders Riisager, Associate Professor Susanne Mossin and Professor Rasmus Ferhmann for help and support during my studies and for creating an open and inspiring research atmosphere at CSC. I must also acknowledge the tremendous effort of Dr Jerrik Mielby. The willingness to always help and shed light on new and interesting subjects have been a bountiful experience of chemical know-how.

I am thankful grateful to Professor Dr Ferdi Schüth for giving me the oportunity to visit his group at Max-Planck-Institut für Kohlenforschung (KOFO) during my external stay in Germany from January 2014 to July 2014. At KOFO, I would also like to thank Dr Claudia Weidenthaler for XPS analysis and Dr Feng Wang for the scientific discussions, inspiration and collaboration.

I must also thank Nedjeljko Seselj who performed all electrochemical measurements. The amount of work put into testing our idea was invaluable. I would like to thank everyone at DTU Centre for Catalysis and Sustainable and DTU Chemistry for good company and to provide a professional work environment. I would especially like to mention Mayra Melián, my office mate through nearly the whole PhD.

This thesis would not have been possible, if it were not for Maria Elibeth Bøg Dyrlund. Her constant support, encouragement, patience, and love.

Jacob Oskar Abildstrøm
Lyngby, November 2016

Abstract

This thesis aims at developing and characterize novel porous nanostructered materials for heterogeneous catalysis. The catalysts are prepared with the goals of increased activity and stability in mind. This will result in lessened waste of precious elements, starting materials, and energy, for a more sustainable chemical industry.

Chapter 1 gives a short introduction to the effect of heterogeneous catalysis upon the current chemical industry. The scope of the thesis will also be sketched.

Chapter 2 is a description of the methods used in the thesis, to characterize the materials produced. These include X-ray powder diffraction, physisorption analysis, and electron microscopy. This include common use, and possible pitfalls.

Chapter 3 is an introduction to zeolites and their properties, mainly shape selectivity and catalytic activity. The diffusion limitations imposed by the porous system in zeolites will be examined as well, and strategies on how to overcome this limitations will be presented.

Chapter 4 describes the synthesis of mesoporous zeolites with a carbon secondary hard template. The carbon is generated through the decomposition of methane over nickel nanoparticles. This is done as an in situ process, directly upon the silica source for the zeolite. This method is significantly cheaper than previously reported for carbon templates. This increases the feasibility of utilizing mesoporous zeolites for various applications. The mesoporous zeolite possessed a greater total pore volume, while still matching its conventional counterpart in terms of crystallinity and acidity. Samples of conventional and mesoporous zeolites were tested in a model catalytic reaction. Here, the mesoporous zeolite exhibited much higher conversion, which is contributed to the enhanced diffusion.

Chapter 5 explains the fundamentals of fuel cells, as a mean to transform chemical energy into electricity. The focus is on proton exchange membrane fuel cells (PEMFC), as the main technique explained. The chapter will also cover degradation mechanisms of the catalyst employed in PEMFC, such as carbon corrosion and particle agglomeration.

Strategies on how to increase resistance towards these degradation mechanisms, such as particle encapsulation, employing graphitic support, and heteroatom doping, will be described. Lastly, a possible PEMFC catalyst based on platinum dispersed on a nanoporous polymer is reported.

Chapter 6 is the examination of a novel catalyst for PEMFC. The synthesis strategy aims at high durability and activity. The basis of the catalyst is the yolk-shell particles consisting of small platinum nanoparticles and a shell of nitrogen doped carbon with graphitic elements. The carbon shell will be activated with potassium hydroxide to generate some microporosity in the shell, to improve the diffusion of reactants. The catalyst is extensively characterize with respect to both the platinum nanoparticles and the carbon shell. Lastly the catalyst is employed in the electrooxidations of methanol, ethanol, and formic acid.

Resumé

Målet med denne afhandling, er at udvikle og karakterisere nye materialer til heterogen katalyse. Disse katalysatorer er ment til brug i syrekatalyserede reaktioner, og elektrokemiske processer. Katalysatorerne er produceret efter et ønske om at forøge aktiviteten og stabiliteten. Dette vil resulterer i mindre spild af dyrebare materialer, udgangsstoffer og energi.

Kapitel 1 giver en kort introduktion til betydningen af heterogen katalyse på den nuværende kemiske industry. Afhandlingens omfang vil også blive opridset her.

Kapitel 2 er en beskrivelse af et udsnit af de metoder der er blevet brugt til at karakterisere materialerne der er blevet produceret. Dette omhandler blandt andet pulver røngtdendiffraktion, fysisorptions analyse og elektron mikroskopi. Disse metoders almindelig brug og potientielle faldgruber vil blive diskuteret.

Kapitel 3 introducerer zeolitter og deres egenskaber, hovedsageligt størrelses-selektivitet og katalytiske aktivitet. De diffusions begrænsninger de porøse systemer pålægger zeoliter vil også blive undersøgt, og strategier til at overkomme disse begrænsninger vil blive præsenteret.

Kapitel 4 omhandler synthesen af mesoporøse zeolitter ved brug af en sekundær hård kultemplat. Kullet er produceret via en dekomposition af metan over nickel nanopartikler. Dette er gjort ved en in situ process der deponerer kultemplaten direkte på silica kilden til zeolitten. Denne metode er markant billigere end andre metoder til mesoporøsitet der benytter kultemplater. Den lavere pris sandsynliggøre ibrugtagen af mesoporøse zeolitter i forskellige applikationer. Ved denne metode blev der produceret en mesoporøs zeolit, der dels havde et stort pore volumen, og samtidig matchede den konvetionelle zeolit på områder som krystallinitet og syrestyrke. Prøver af den konventionelle og mesoporøse zeolit blev testet i en katalytisk model reaktion. Her udviste den mesoporøse zeolit en betydelig højere konvertering, som blev begrundet med den forbedrede diffusion.

Kapitel 5 gennemgår de grundlæggende koncepter bag brændsels cellers transformering

af kemisk energi til elektricitet. Fokus bliver lagt på proton exchange membrane fuel cells (PEMFC). Kapitlet gennemgår også de degraderingsmekanismer der forekommer i katalysatoren i en PEMFC, såsom kulkorrosion og partikel agglomerering. Strategier til hvordan man kan forøge modstandskraften overfor degraderingsmekanismerne, så som indkapsling af nanopartikler, grafitisk bæremateriale og doping med heteroatomer, vil blive beskrevet. Slutteligt, en mulig PEMFC katalysator baseret på platin fordelt på en nanoporøs polymer er rapporteret.

Kapitel 6 er undersøgelsen af en innovativ katalysator til PEMFC. Målet bag syntese strategien er høj stabilitet og aktivitet. Konceptet for katalysatoren er at indkapsle små platin nanopartikler med en skal af nitrogen dopet kul, der indeholder grafitiske elementer. Kul skallen vil blive aktiveret med kaliumhydroxid for at frembringe mikropore i skallen for at øge diffusionen af reaktanter. Katalysatoren er karakteriseret i forhold til både platin nanopartiklerne og skallen af kul. Til sidst vil katalysatoren bliver brugt i elektrooxidation af methanol, ethanol og myresyre.

Contents

Chapter 1.

Introduction

This chapter touches upon the significance of solid catalysts in the chemical industry. The outline of the thesis will be stated.

Heterogeneous catalysis have an immense impact on today's society, allowing us to convert raw materials into valuable chemicals and fuels in a feasible, efficient, and environmentally benign manner. Solid catalysts have numerous applications in areas such as energy production, petroleum industry, the production of chemicals and pharmaceuticals, and environmental technologies. It has been estimated that 90% of all chemical processes use solid catalysts.[1] By improving the catalytic processes, it is possible to lower the energy requirements, make better use of natural resources, reduce amount of by-products formed, and eliminate contaminant waste.

Because of stricter environmental regulations and the continuing depletion of fossil resources, the future chemical industry must gradually rely on renewable resources such as biomass for production of bulk and fine chemicals. As a consequence of this, heterogeneous catalysis is finding new applications in emerging areas such as fuel cells, green chemistry, nanotechnology, and biotechnology. Indeed, continued research into heterogeneous catalysis is required to allow us to address increasingly complex environmental and energy issues facing our industrialized society.

1.1. Scope of the thesis

This thesis aims at developing and characterizing novel nanostructured solid catalysts. The main focus will be in two different types: mesoporous zeolites as solid acid catalysts and platinum nanoparticles in nitrogen doped carbon spheres for fuel cell applications.

Zeolites are commonly applied in petroleum refining and petrochemical industry. Their usefulness originates of their structure which contains a large pore volume based on micropores and possible acid sites. Their effectiveness is however hampered by these micropores which decreases diffusion of reactants and products. This in turn leads to low conversion rates, and the deactivation of the zeolite catalyst. By generating additional porosity these drawbacks can be reduced. So far, the procedures to synthesize these types of zeolites are cumbersome and expensive. Chapter 4 explores an innovative route to feasibly synthesize mesoporous zeolites.

Fuel cell are highly regarded as an sustainable energy source. However, in order to be industrial viable, the activity and stability of the platinum catalyst will have to be improved. In Chapter 6, several techniques on how to increase both the activity and durability of the Pt catalyst are tested. The general synthesis approach, is to encapsulate isolated Pt nanoparticles in hollow nitrogen doped spheres, of partly graphitic carbon. The small size of the Pt and the structure of the carbon support, should give rise to enhanced activity and durability.

In addition, a nanoporous polymer based on polyphenylene will be mentioned. The material was developed at Max-Planck Institute für Kohlenforschung, and multiple variations of it were prepared during an external stay there in the spring of 2014.

1.2. Polyphenylene, a nanoporous polymer

One major ambition in catalysis is to combine the advantages of molecular catalysts and heterogeneous processes. The hope is to maintain, or even improve, the reactivity and selectivity of the molecular catalysts, while facilitating product recovery and catalyst recycling.[2,3] A material class that have seen increased interest in light of this, is nanoporous polymers.[4] One such nanoporous polymer catalyst has been developed at Max-Planck Institute für Kohlenforschung, based upon a polyphenylene backbone. The catalyst is synthesised by a Pd catalysed Suzuki coupling reaction between 1,2,4,5-tetrabromobenzene and benzene-1,4-diboronic acid, which resulted in the direct formation of small palladium nanoparticles that were evenly distributed throughout the porous polyphenylene network, see Figure 1.1.

The cross-linked three-dimensional polyphenylene have a surface area of >1000 m^2 g^{-1} and a total pore volume of 0.46 m^3 g^{-1}, based on micropores (<1.5 nm) and supermicropore (1.5-2 nm). The polyphenylene is highly stable and able to withstand temperatures

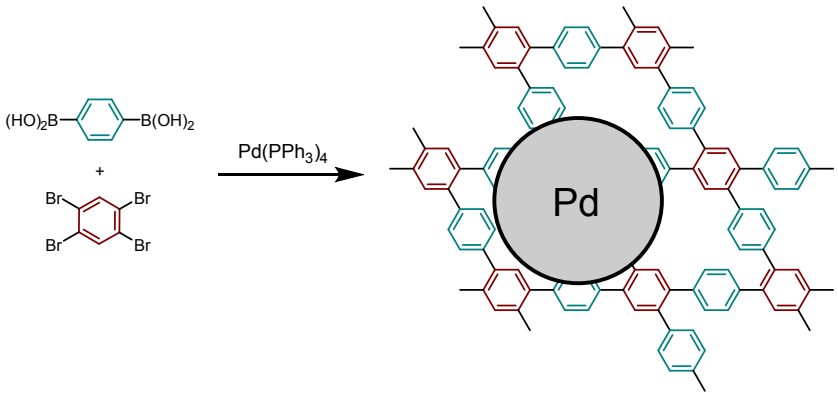

Figure 1.1.: *The synthesis of prepared by Suzuki coupling of 1,2,4,5-tetrabromobenzene and benzene-1,4-diboronic acid.*

up to 400 °C in air and up to 600 °C in Ar.[5]

The Pd/PPhen was applied as a catalyst in several Suzuki coupling reations, where it showed remarkable catalytic activity compared to other carbon supported Pd nanoparticles. It is suggested that the superior activity stems from the PPhen unique conjugated aromatic structure, which was not present in the other supports. The PPhen may allow for strong interactions with the substrate, similarly to the proposed effect of conjugated aromatic ligands in C-C coupling reactions catalysed by palladium complexes.[5]

The nature of the catalytic species in Suzuki coupling reactions are still debated. Recently, several groups have reported palladium clusters in solution near the solid catalyst to responsible for the catalytic activity.[6]

In order to explore the possibilities emerging with this type of support, several different metal nanoparticles were deposited on the clean PPhen. These were intended to be applied in reactions such as biomass conversion, Fischer-Tropsch process One of the applications, was to utilize the polymer as a support for proton exchange membrane fuel cell (PEMFC). The large surface area, sp^2 hybridized carbon, and modular framework, makes it an excellent candidate for a PEMFC catalyst support. A more detailed review of this application is given in Section 5.5.

1.3. Experimental section

1.3.1. Synthesis of Pd/PPhen

The 2.7 wt% Pd/PPhen catalyst were prepared according to the following procedure: 1,2,4,5-tetrabromobenzene (0.765 g, 1.94 mmol) and benzene-1,4-diboronic acid (0.645

g, 3.89 mmol) were added to 60 ml dimethylformamide. The mixture was degassed through three freeze-pump-thaw cycles. K_2CO_3 (2.0 M, 7.5 ml) and $Pd(PPh_3)_4$ (0.225 g, 0.19 mmol) were added with subsequent three freeze-pump-thaw cycles. The mixture was then purged with Ar and heated to 150 ℃for 20 hours under stirring. The product was precipitated in water and washed with water, dichloromethane and methanol and then dried at 60 ℃.

1.3.2. Synthesis of PPhen

To producte the palladium free PPhen, Pd/PPhen was subjugated to sequential leaching treatments. Pd/PPhen (1.0 g) was mixed with HCl (6 M, 10 ml) and H_2O_2 (37%, 10 ml), heated to 60 ℃, and stirred for 2 hours. This procedure was repeated three times. After each cycle, the solid was washed once with water and once with methanol. Lastly the solid was allowed to dry at 60 ℃.

Chapter 2.

Characterization

This chapter gives a short introduction to some of the methods commonly used to characterize the solid catalysts produced in this thesis. The methods reviewed involve X-ray powder diffraction, physisorption, and different types of electron microscopy.

2.1. X-ray powder diffraction

XRPD is a widely used analytic method for structural characterization of crystalline materials. The method is based on diffraction, which occurs when an incident radiation interacts with an ordered solid and the wavelength of the electron magnetic radiation is in the same order as the distance between the crystal planes. It is used to identify crystal structure and detect impurity phases. Such information can be useful when determining possible active species, structure-activity relationships and optimizing the catalyst synthesis procedure.

2.2. Gas physisorption

A key parameter for solid catalysts, is the accessibility to and from the active sites for molecules. This method provides information on surface area and the volume and size distribution of possible micro-, meso- and macropores. According to the IUPAC definition, porous materials are microporous if the pores are $<$2 nm, mesoporous if the pores are 2-50 nm and macroporous if the pores are $>$50 nm. Physisorption data is often presented in an adsorption isotherm that shows the amount of adsorbed gas over an interval of partial pressures at constant temperature. The shape of the isotherm depends on both the adsorbate and the adsorbent. The N_2 physisorption isotherms are classified into six types by IUPAC. These are presented in Figure 2.1, and briefly described below.[7]

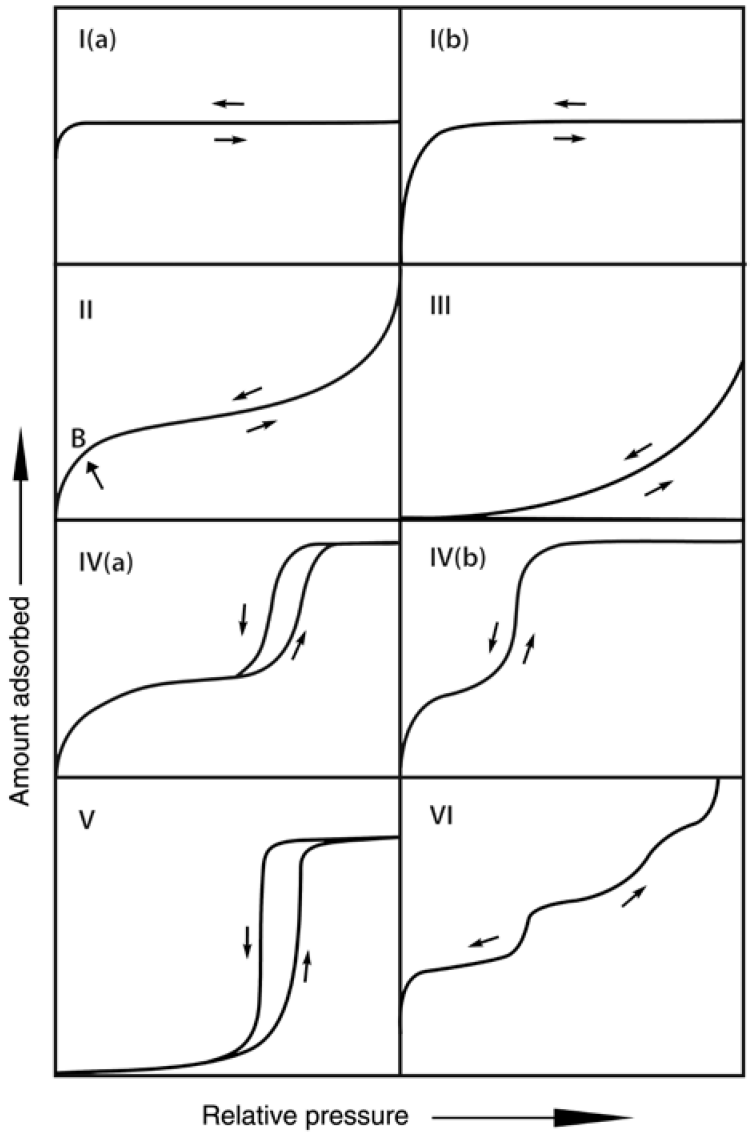

Figure 2.1.: *IUPAC classification of physisorption isotherms.* [7]

- Type I isotherms are characterised by the limiting uptake, which happens at relative low pressure and is controlled by the accessible micropore volume, and not the internal surface area. The steep uptake at very low p/p^0, is due to enhanced adsorbent-adsorptive interactions in narrow micropores of molecular dimensions. Type I(a) isotherms are given by microporous materials having mainly narrow micropores. If the absorbent contains a broader range of micropores and possibly narrow mesopores, below 2.5 nm, a type I(b) isotherms will be observed.

- The type II isotherm is typical for nonporous or macroporous materials. The knee, Point B, of the isotherm corresponds to the point where the adsorption is equivalent to a monolayer and multilayer adsorption begins to take place.

- The type III isotherms contains no Point B and therefore no identifiable monolayer formation. This occurs in materials with weak adsorbent-adsorbate interactions, and is often observed in nonporous or macroporous solid.

- The type IV isotherms are most common when analyzing mesoporous materials. The hysteresis loop between the adsorption and desorption branches, is a very characteristic feature for this type of isotherm, and is attributed to capillary condensation taking place in mesopores.

- The type V share some similarities with type III at low relative pressures. This is again a sign of weak adsorbent-adsorbate interactions. At higher p/p^0, molecular clustering is followed by pore filling.

- The type VI isotherm shows a layer-by-layer adsorption on highly uniform nonporous material. Type VI isotherms are typically obtained from Ar or Kr physisorption on graphitized carbon black.

As mentioned above, the hysteresis loop observed in type IV isotherms is typically caused by capillary condensation in mesoporous materials. Figure 2.2 shows the classification of the five types of hysteresis loops.[7] The type H1 loop is commonly detected in porous materials with a narrow size distribution, such as templated silicas and mesoporous carbons.

H2 loops are found in samples that contain a complex pore structure. The steep desorption branch of H2(a) can be attributed to either pore-blocking in a narrow range of pore necks, or to cavitation-induced evaporation. This type of hysteresis loop is given

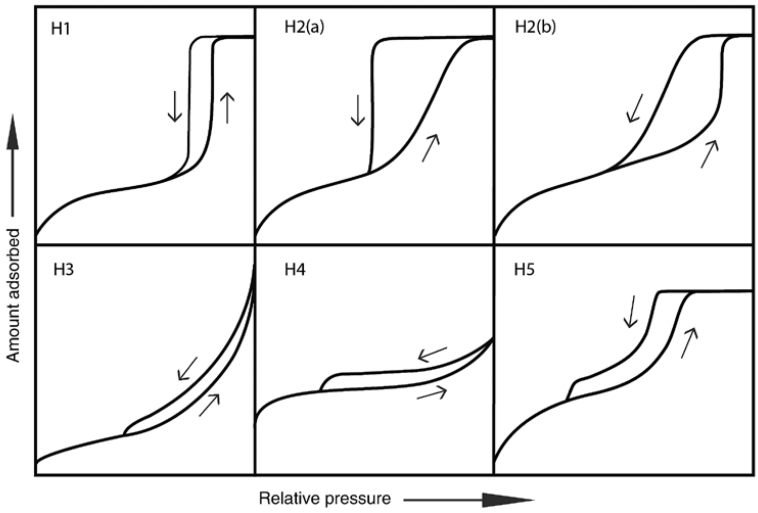

Figure 2.2.: *IUPAC classification of hysteresis loops.*[7]

by many silica gels and some ordered mesoporous materials. The Type H2(b) loop is also associated with pore blocking, but the size distribution of neck widths is much larger than in H2(a).

H3 loops are given by non-rigid aggregates of plate-like particles, but also if the pore network consists of macropores which are not completely filled with pore condensate. The H4 loop are often found with aggregated crystals of zeolites, some mesoporous zeolites, and micro-mesoporous carbons. Although the Type H5 loop is unusual, it has a distinctive form associated with certain pore structures containing both open and partially blocked mesopores.

The H3, H4, and H5 loops all share a common feature of a sharp step-down of the desorption branch. The closure point is often determined largely by the adsorbate rather than the porosity of the adsorbent (e.g. p/p^0=0.42 for nitrogen at 77 K). Calculations based on the desorption branch alone may therefore lead to an artificial narrow peak in the pore size distribution.[8]

2.3. Electron microscopy

Electron microscopy is a widely used technique for imaging of solid materials. Electron microscopy uses a focused high energy beam of electrons, that is directed onto a sample. Due to the shorter wavelength of electrons than visible light, the use of an electron beam results in much higher magnification than can be achieved using optical spectroscopy.

Electron microscopy are frequently used for the analysis of solid catalysts, as it allows for visualization of the catalyst morphology, and possible determination of any nanoparticles present in the sample.[9] In this thesis, two types of electron microscopy is used, scanning electron microscopy (SEM) and transmission electron microscopy (TEM). The two methods are identical in the sense that they both utilizes an electron beam to produce an image, the methods of producing the images are however different. SEM is based on the scattering of the electron beam by the atoms of a material. The electrons which are reflected by the sample and emitted secondary electrons, are detected to give a map of the surface topography of the sample. With TEM the electron beam is transmitted through the sample, which gives a two-dimensional image that is magnified and projected on a fluorescent phosphor screen or recorded using a chargecoupled device (CCD) camera.

2.3.1. Scanning electron microscopy

SEM is based on the scattering of high-energy electrons by the atoms of a material. In the SEM microscope the electron beam is emitted from an electron source and accelerated to 1-30 keV. The region of the specimen that is penetrated by the electron beam is referred to as the interaction volume. Even though radiation is generated within the entire interaction volume, the radiation will only be detected if it leaves the sample. A schematic of the interaction volume is given in Figure 2.3. The secondary electrons have less energy than the backscattered electrons, but originate from a region that is only a little larger than the incident beam and therefore gives a good resolution. The X-rays are not easily absorbed, and the detected X-rays will therefore originate from almost the entire interaction volume.[10] The depth of the interaction volume is very dependent upon the type of sample and acceleration voltage of the electron beam. Heavy atoms will decrease the penetration depth of the electron beam, and a high accelerated voltage will penetrate the sample deeper. These factors must be taken into account when performing SEM, as a high penetration depth will result in more information about the bulk of the sample compared to the surface.

When analyzing solids with SEM, it is important to be aware of the impact of the electron beam on the sample as noted above. In an example from Castellino et al., SEM was done on a fresh vanadium catalyst, Figure 2.4A, and a sample exposed to phosphoric acid (P100), Figure 2.4B.[11] The group concluded, that the P100 sample had been physically deactivated, and had lost some of the porous structure present in the fresh sample. The electron microscopy images in Figure 2.4 supports this argumentation.

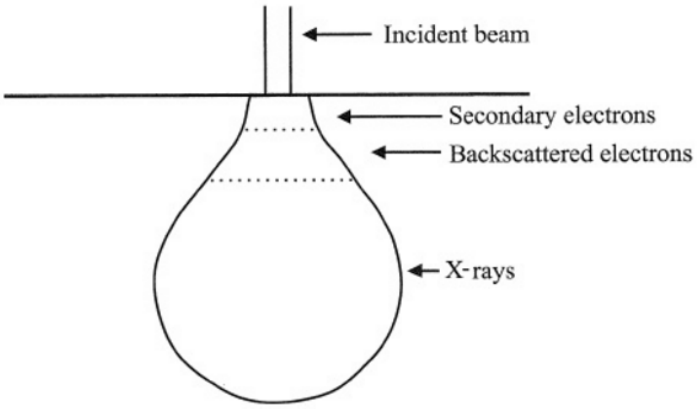

Figure 2.3.: *The interaction volume and the regions from where secondary electrons, backscattered electrons, and X-rays may be detected.*[9]

There is however a crucial difference between the two. The image of the deactivated sample is taken at an acceleration voltage of 20.0 keV, while the fresh sample was analyzed at 5.0 keV. This difference will result in a lower resolution of the P100 surface, as more electrons are generated at the bulk of the sample compared to the fresh sample. The group did however perform several complimentary techniques, that supported the claim of physical deactivation of the catalyst when exposed to H_3PO_4.

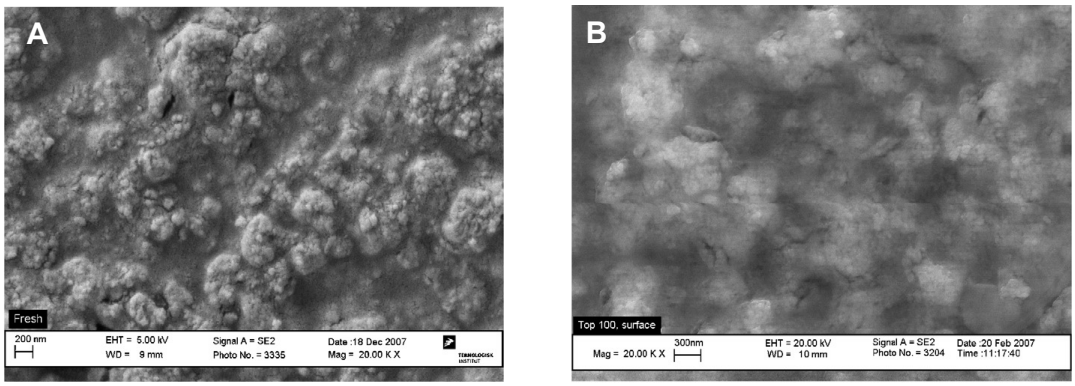

Figure 2.4.: *SEM images of a fresh vanadium catalyst sample (A) taken at 5.0 keV, and (B) an identical catalyst after being exposed to H_3PO_4, taken at 20.0 keV.*

2.3.2. Transmission electron microscopy

Transmission Electron Microscopy (TEM) is based on electrons of high energy (80-300 keV) that pass through a thin solid sample. If the sample is thin enough, most of the primary electrons will pass through the sample. Their range and energy spread will

however be different, due to elastic and inelastic scattering within the sample. It is only the electrons that go directly through the sample, that creates the image of the species. This is known as bright field imaging. Regions of the sample which are thicker, or have a higher density, will scatter more strongly and be viewed darker in the resulting image.

Due to the nature of TEM, some general guidelines must be followed when using this technique for analysing samples. Because of the very small sample size at high magnification, it is mandatory to study several areas to ensure that the images recorded are truly representative for the sample. In addition, one must bear in mind that the images acquired through TEM are two-dimensional projections of three dimensional objects, it is therefore necessary to pay attention during the interpretation of shapes and spatial relationships. TEM images are based on the transmitted electrons, so it is important to remember that dark areas (low intensity) of the image can both be due to the scattering of electrons from heavy elements, or a thick area of the sample. So TEM pictures show contrast based on mass and thickness of the sample. It is important to remember that the beam of electrons is of quite intense energy. Destruction or alteration of some type of samples are possible during imaging, which will create a non-representative image. To counter this, it is advised to lower the acceleration voltage of the beam, even though it will lead to a lower resolution. Another possibility is to not remain over the part of the sample for a longer period of time.[10] During imaging of small metal nanoparticles on support, it is sometimes preferable to defocus the beam. This can cause the relative contrast of the metal nanoparticles to enhance, while the contrast of the lattice fringes of the support are suppressed.[12] By obtaining these out-of-focus images, it is impossible to obtain accurate size measurements because of the poor image resolution.

Chapter 3.

Zeolites

This chapter gives an introduction to solid acid zeolite catalysts. The well known limitation of intra-zeolitic diffusion will be discussed, as well as the current progress in the field of preparing mesoporous zeolite catalysts.

Zeolites are a class of solid materials, heavily used in todays chemical industry. Here they are applied in such various areas as ion exchange, adsorbants, and solid catalysts.[13] The majority of the large scale catalytic applications of zeolites, are within the fields of petroleum refining and petrochemical industry.[14] Zeolite catalysts are also being increasingly adopted in processes such as: environmental applications, biomass conversion, methanol to gasoline (MTG), and in the transformation of petrochemical raw materials such as coal, gas, and oil into a wide array of products.[15,16]

The reason for the usefulness of zeolites, can be ascribed to their many unique physical properties. Zeolites are crystalline alumina silicates, built from tetrahedral TO_4 units (T = Si or Al). The framework of a zeolite can be thought of as made up from a number of secondary building blocks, forming a crystalline solid with a high surface area, outstanding thermal stability, and well-defined system of pores.[17] The diameters of the pores are determined by the number of T-atoms in the ring surrounding the pore. The pores are defined as: small-pore (up to 8 T-atoms), medium-pore (up to 10 T-atoms), large-pore (up to 12 T-atoms), and extra large-pore (up to 20 T-atoms).[18] 8-, 10-, an d 12-rings are most common in zeolites. This gives the micropores in zeolites diameters of around 4-8 Å, which are in the same order as small organic molecules. Since zeolites can be used to separates molecules based on their size, zeolites are also known as molecular sieves.

Figure 3.1 shows a MFI structured zeolite, and gives an impression of the uniform

micropores that are present inside the crystal structure. In principle, the MFI zeolite can be built from secondary building units of 12 T atoms (emphasised in black).

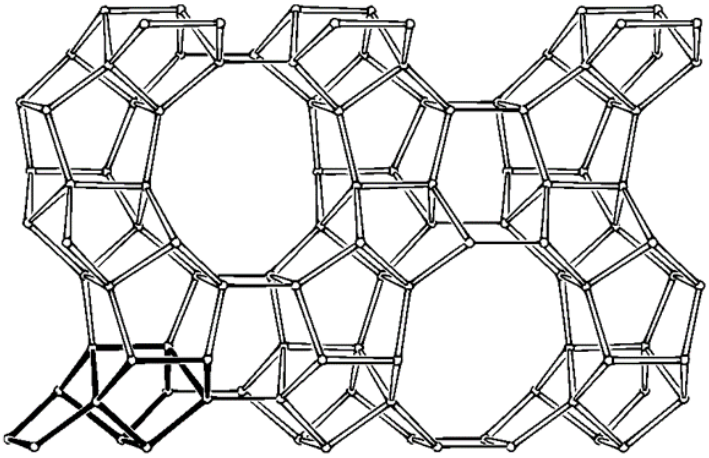

Figure 3.1.: *The connection mode of a MFI zeolite. Oxygen atoms are omitted for clarity. Adapted from IZA.*[19]

Currently there are 218 different framework types of zeolites. Each zeolite has been granted a three letter code, such as CHA for chabazite. For natural occuring zeolites the code is based on the mineral name, such as STI for stilbite. The naming of synthetic zeolites are more complicated. One example being the structure of the well-known ZSM-5 (five) zeolite has the three-letter code MFI. As this code provides no chemical composition information, other names have been applied to synthetically produced zeolites to circumvent this challenge. For instance SAPO-34 and SSZ-13 are both type CHA framework, the first containing P as some T-atoms, while SSZ-13 has a Si/Al ratio not found in nature.

Aluminum in the zeolite framework is a trivalent metal which is tetrahedrally coordinated. This introduces a negative of charge which must be compensated for by an organic or inorganic cation (such as an alkali or alkaline-earth cation). Figure 3.2 shows a representation of an Al-containing zeolite, where the negative charge is compensated for by a proton. By exchanging the cations, it is possible to modify the chemical and catalytic properties of a given zeolite. It is this ability that is the basis for the massive application of zeolites as ion exchangers and solid acid catalysts.[20–22]

The micropores present in the zeolite introduce shape selectivity which are of paramount importance in their catalytic applications. Indeed, the microporous channels, with dimensions in the range of small reactant molecules, provide zeolites with size- and shape

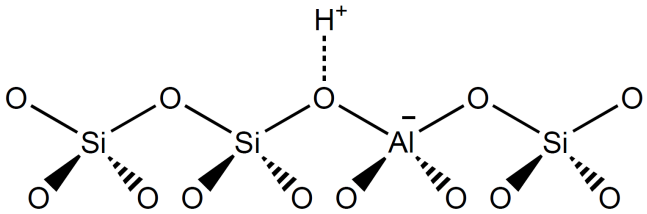

Figure 3.2.: *Schematic representation of a Brønsted acid site in an Al-containing zeolite.*

selectivity towards reactants, products or transition states.[23] The shape selectivity involving reactants and products is due to mass transport discrimination and is related to molecular sieve effect.[24] Transition state selectivity occurs when the geometry of the pores favors one transition state over several possible.

It is possible to synthesize zeolites without aluminum, or containing elements such as B, Fe, Ga, Ge, P, Sn, Ti, or V. While these are properly defined as zeotypes, they will be mentioned as zeolites in the remainder of the thesis. The addition of these hetero atoms in the framework, changes the catalytic properties of the zeolite, as well as its stability. The inclusion of germanium has for example been found to have a strong structure-directing influence on the zeolite, as it favors the formation of double four-membered-rings.[25,26] Recently, Sn-containing zeolites have received a great deal of research interest due to their ability to convert sugars into important platform molecules.[27] By substituting Ti for Si in pure silica zeolites, it is possible to perform selective oxidation reactions, such as the hydroxylation of phenols, epoxidation of alkenes, and ammoxidation of ketones.[28–30] These titanium silicalites are commercially used in several industrial processes.

3.1. Diffusion in zeolites

Despite the shape selective advantages of microporous zeolites, the pores are also the origin of some complications. Because the micropores are of the same order of magnitude as small molecules, the micropores can impose mass transfer limitations that significantly reduces the transport of molecules to and from the active sites. The rate of diffusion in a zeolites micropore, is often termed (intracrystalline) configurational diffusion and is common in solids. It is characterized by low diffusivities, which can be up to 2–3 orders of magnitude smaller than molecular- and Knudsen diffusion, see Figure 3.3.[31] This creates three disadvantages: Firstly, the delayed transport of reactants may favor further conversion of these molecules into unwanted side products. For some catalytic

applications, this way lead to severe deactivation such as coke formation, or polymerization of by-products.[32] Secondly, the slow transport will result in poor utilization of the zeolite crystals, as only a small fraction of the zeolite crystal will be utilized during the chemical reaction.[31] Finaly, the slow diffusion can ultimately determine the reaction rate of the overall process.[33] In addition, this hinders the application of zeolites in reactions with bulkier molecules. Therefore large efforts have been made in order to increase the accessibility of active sites to larger molecules and to reduce the impact of intracrystalline diffusion on catalyst lifetime.

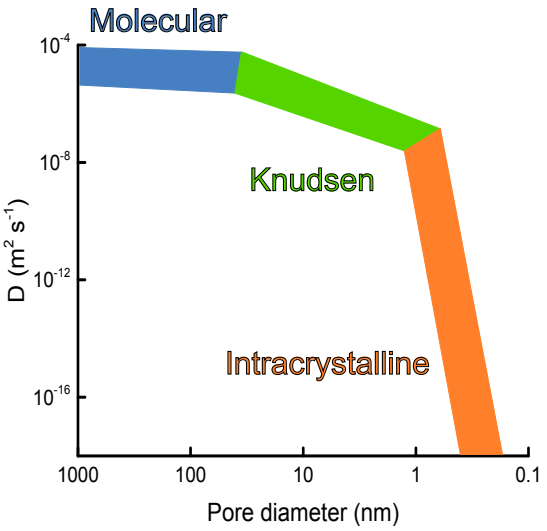

Figure 3.3.: *Effects of pore diameter on molecular diffusivity.*

The utilization of a catalyst is classically described by the effectiveness factor η, Equation 3.1, which relates the observed reaction rate with the intrinsic chemical rate. $\eta \to 1$ represents a situation where the observed reaction is free from any diffusion limitations.

$$\eta = \frac{r_{observed}}{r_{intrinsic}} = \frac{\tanh(\phi)}{\phi} \tag{3.1}$$

where r is the reaction rate. The effectiveness factor is a function of the Thiele modulus, ϕ, which is defined by

$$\phi = L\sqrt{\frac{k_m c_s^{n-1}}{D_E}} \tag{3.2}$$

Here, L is the diffusion path length, k_m is the rate constant of the reaction, c_s is the concentration at the surface of the pellet, n is the reaction order, and $D_{A,eff}$, the effective

diffusion coefficient. On one hand, a small Thiele modulus indicates that the reaction rate is low and the microkinetics is limiting the overall reaction. On the other hand, a large Thiele modulus indicates a low diffusion rate and a diffusion limited reaction.

In light of this, it is clear that there are two ways to enhance the utilization of a zeolite. One approach is to decrease the intracrystalline diffusion path length (L) in the pore system. This can be done e.g., by reducing the crystal size of a known zeolite,[34] or exfoliating layered zeolites.[35] The other approach is to increase the effective diffusivity, D_E , by increasing the pore size of the zeolite. This can either be done by synthesizing zeolites with large pores, or by introducing an additional pore system, such as meso- and/or macropores.

3.2. Strategies to improve molecular diffusion in zeolites

There are two major pathways to improve the diffusion in zeolites. One approach is to shorten the diffusion path length, while the other is to increase the intracrystalline diffusivity. There are multiple synthesis strategies on how to achieve this. The strategies explained in this thesis as shown in Figure 3.4. A secondary template (a), is a sacrificial scaffold that directs the formation of an additional porosity during the zeolite growth. This is done without it becoming a part of the zeolite framework during crystallization. Afterwards the template is removed without any loss of the structural features. This strategy can result in both nanosized zeolites or zeolites containing meso- and/or macropores. The name secondary template, is a results of the common zeolite structure directing agent (SDA) being thought of as the primary template. Secondary templating is often distinguished as either "hard" or "soft", based on the nature of the template. Hard secondary templates are often carbon materials, e.g. carbon particles,[36] aerogels,[37] or plant materials. Soft secondary tempates cover materials such as polymers, surfactants or large silylating agents.[38] Here, only the hard secondary templates will be detailed further.

(b) concerns the growth of nanozeolite aggregates forming a mesoporous network. Thus bypassing the need for any intricate, and often expensive, template.

These two first strategies are often termed as "bottom up" processes, focusing on the synthesis of a mesoporous zeolite. In contrast, post synthesis modification of an existing zeolite is termed "top down" processes. It is in this category that we find the last two strategies. Dematallation (c) is the extraction of framework metals. The most studied

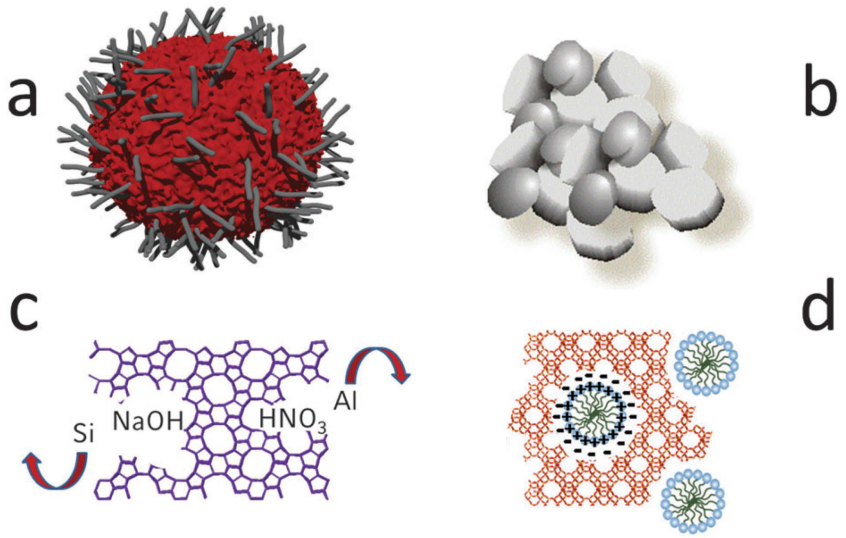

Figure 3.4.: *An overview of the methods for enhancing molecular diffusion in zeolites: (a) utilizing a hard template in form of an inert matrix, (b) formation of nanosized zeolites without any template, (c) post-synthetic dissolution of metal species from zeolites, (d) demetallation and recrystallization after synthesis.*[39] *Based on.*[40]

methods are dealumination and desilication. By adding a secondary soft template either during or after desilication, it is possible to recrystallize the silica species (f). This methods generates well-defined mesopores and largely avoids the loss of material. The rest of this chapter will review these different strategies in more detail.

3.2.1. Hard secondary templates

Hard templates has proven to be one of the most effective methods to tailor the morphology, porosity, and composition of mesoporous zeolites. The method revolves around the use of an sacrificial inert matrix. This matrix can consist of different materials such as metal oxide nanoparticles ($CaCO_3$), plant materials, resin beads, or aerogels, but carbon compounds have been studied most frequently. Here carbon as a hard template will be reviewed in detail, as this is the most studied one. Other hard templates will be mentioned briefly.

For the preparation of synthesis gel with a hard template, the incipient-wetness impregnation method is most commonly used. The inert matrix is impregnated with an organic structure directing agent, silicon, and aluminum sources in ethanol. The procedure is done in two steps, with each step filling the total pore volume of the inert matrix. Another preparation method with hard templates, is to transfer zeolite precursors that

are in the nanometer scale and colloidally stable, inside the pores of the inert matrix.[41] This method results in the formation of zeolite nanocrystals.

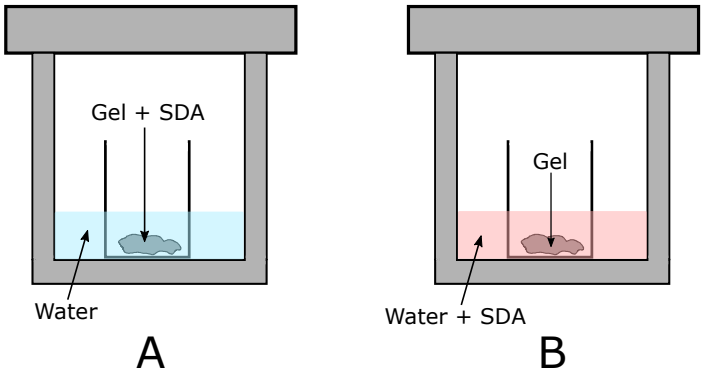

Figure 3.5.: *Schematic of the synthesis of zeolites using the (A) steam assisted crystallization and (B) vapor phase transport methods.*

In order to control the zeolite synthesis in a hard template/confined space, steam assisted crystallization (SAC) or vapor phase transport (VPT) methods are often applied. These methods are based on separation between the zeolite synthesis gel, and the liquid phase in the bottom of an autoclave. This limits the migration of the synthesis gel from the confined space and onto the external surface of the template. For volatile SDAs, such as EDA, the liquid phase is a mixture of water and SDA, the VPT method. The SDA is vaporized and transported to the synhtesis gel for zeolite crystallization. The SAC method is used when utilizing nonvolatile SDAs, such as TPAOH. The SDA must be mixed with the synthesis components within the confined space, and the water only supplies saturated steam for the zeolite crystallization. The two methods are illustrated in Figure 3.5, where the difference between the SAC and VPT methods are illustrated. It is important to note, that in both cases the gel and water do not touch, but is separated by e.g. a teflon cup. These methods have been successfully applied to synthesize several zeolite types, including ZSM-5, MOR, FER, BEA, EMT, FAU.[42–44]

Commercial carbon blacks, nanotubes, and nanofibers

Researchers at Haldor Topsøe reported the first zeolites synthesized with the aid of commercial carbon as a hard secondary template, carbon Black Pearls® (BP2000 and BP700). Carbon Black Pearls® is composed of carbon nanoparticles with a size range of 10 to 50 nm, and mesopores generated by the agglomoration of carbon nanoparticles. As explained above, the carbon template was impregnated with the zeolite synthesis gel.

First with a solution of the structure directing agent, sodium hydroxide, ethanol, water, and aluminum isopropoxide. After the ethanol had evaporated overnight, the template was impregnated with ethanol and silica source (TEOS). After hydrothermal synthesis of the zeolite within the pores of the carbon matrix, the sample was calcinated. This was done in order to decompose the SDA, as well as the carbon template. The resulting product was found to be zeolite nanocrystals, with a size around 20 nm.[45] This method is often referred to as confined space synthesis, and was proven successful for synthesizing zeolite nanocrystals of ZSM-5, silicalite-1, zeolite A, zeolite Y, and zeolite beta.[46]

By using an excess of the zeolite synthesis gel in the impregnating of the carbon matrix, single crystalline mesoporous zeolites can be synthesized instead of nanocrystals. The crystallization of a large single crystal encapsulates the carbon matrix, which then leaves a negative imprint of intracrystalline mesopores after calcination.[47] The formation of either zeolite nanocrystals or mesoporous zeolite single crystals, is speculated to be determined by the nucleation rates in relation to the crystal growth rate. High nucleation rates favour formation of nanosized zeolites whereas low nucleation rates favour formation of mesoporous zeolites.[48] The relationship between the nucleation rate and the growth rate can be affected by numerous factors such as the synthesis gel composition, crystallization temperature, zeolite structure, and carbon template as well. This makes it possible to control the morphology of the final zeolite.[49] Other commercial carbon types, such as carbon nanotubes, nanofibers, carbon black powders (Mogul® L and Monarch® 1300) have been applied to this synthesis pathway.[50,51] The mesoporous zeolites produced with an excess of synthesis gel, exhibited intracrystalline mesopores in the broad size range of 5 to 50 nm.

This approach of using commercial carbon have been demonstrated for the synthesis of MFI-type zeolites, including ZSM-5, the pure siliceous form silicalite-1, the titanium form TS-1, as well as a MEL type zeolite, ZSM-11.[47,52,53] Other mesoporous zeolite types and aluminophosphates, such as beta (BEA type), $AlPO_4$-5 (AFI), and $AlPO_4$-34 (CHA) were prepared by the hydrothermal flouride route.[54] Here, the hydroxide ion used in the common alkaline synthesis route, is substituted by a fluoride ion. This allows for the crystallization to take place at pH around 5, which favors a slow groth and the formation of single crystals.

Mesoporous ordered carbon/composites

Instead of using a synthesis gel, it is possible to prepare a composite material consisting of silica and a hard template in one step. For example, mesoporous silica materials as hard templates have been used to prepare mesoporous carbon and polymer materials. These hard templates are typically prepared in a multistep process where a carbon resin is cast and carbonized over a silica template. The silica template can be directly used as the growth source for the formation of hierarchical zeolites.[55,56] The use of silica/carbon composites as starting materials not only offers an opportunity to introduce a synthesis gel in the confined space but also can simplify the synthesis procedure.

Non carbon hard templates

Alternatively, the silica source can be applied as a sacrificial hard template, which leads to their consumption during zeolite crystallisation.[57] Recently, Machoke et al. prepared macroporous zeolites, through impregnation of mesoporous silica particles with TPAOH and subsequent steam assisted crystallization.[58]

3.2.2. Nanosized zeolites without templates

In order to synthesise nanosized zeolites, the reaction conditions has to be controlled in great detail. In particular, the homogeneity of the starting system and the simultaneity of event to form the precursor gel are very important. The synthesis is therefore often performed in highly diluted systems with large quantities of tetraalkylammonium hydroxide, which induces a fast nucleation and the formation of smaller crystals with a narrow particle distribution [169]. Furthermore, the synthesis is often carried out under mild condition, typically at temperatures $<$120 ℃. Although nanosized zeolites have many interesting advantages, such as the controllable size, well-defined crystal morphology and a high colloidal stability, there are also some important drawbacks, including the difficult scale up, the low crystalline yield (typically $<$10%) and the difficult separation.[59]

3.2.3. Demetalation of zeolites

Generating mesoporosity in a zeolite, can also be done post synthesis through demetallation. This strategy is essential the extraction of framework atoms. As zeolites are predominantly aluminosilicates, the most studied methods are dealumination and desilication. It is a destructive process, creating mesopores at the expense of bulk zeolite, and

can be done through acid, steam, and base treatment. The use of demetallation to overcome the diffusion limitations in place in zeolites, have become an attractive method. Advantages count low cost, and no major health/safety/environment, HSE, issues.[60] The mesoporosity generated in the zeolite are rather different depending on whether aluminium or silicon is extracted. Both dealumination and desilication are therefore discussed below.

Dealumination

Dealumination is the most used demetalation process in industry.[60] It can be performed in numerous ways by hydrolysis of the Al-O-Si bonds of the zeolite framework through e.g. calcination, steaming, and acid leaching.[61–63] Dealumination with steaming and acid leaching are commonly used to obtain FAU type zeolites with high Si/Al ratio, which are not feasible by direct synthesis.[64,65] These materials are more stable and possess stronger acidity than compared with the untreated materials. During these treatments, mesopores are also formed.[66] The generated mesopores are not connected to the outer surface of the zeolite, but are present as isolated cavities.[51] This do not significantly affect the intracrystalline diffusion.[67] Dealumination have been performed on other zeolite types

Desilication

The introduction of mesopores by the alkaline leaching of framework Si has become a very attractive method due to the combination of both experimental simplicity and efficiency of the hierarchical zeolites obtained.[33] The mesopores induced by alkaline treatment are interconnected and accessible from the external surface of the zeolite crystal, representing a clear advantage for access limited and diffusion constrained reactions.[68,69] The advantages of desillication is that the method is relatively cheap, applicable to several zeolite types, and the porosity can be tuned by simply changing the base, pH, temperature or reaction time.[65] In addition, the first step to scaling up of the desilication treatment has been reported.[70]

Groen et al. identified that the presence of Al gradients in the zeolite crystals and, specifically, the concentration of the framework Al species played key roles in the mechanism of mesopore formation in ZSM-5 type zeolites in alkaline medium. A Si/Al ratio of 25-50 was discovered for being optimal for obtaining significant intracrystalline mesoporosity while preserving Al centers. A lower ratio, Si/Al$<$20, prevented the extraction of Si, limiting the generation of mesopores. Zeolites with a high degree of silicon, Si/Al$>$50,

showed significant Si extraction creating relatively large pores, resulting in a great loss of microporosity.[71] By using organic bases, such as TPAOH or TBAOH (tetrabutylammonium hydroxide) instead of NaOH, or use of tetraalkylammonium salts together with NaOH helped to better preserve microporosity.[72]

A significant drawback of desillication, is that it is very dependent on the Si/Al ratio and may result in relatively low yields of recovered zeolite. Often the yield is only 40-90% of the parent zeolite, which may significantly increase the final cost of the overall process.[60] A method for creating mesopore zeolite crystals by avoiding the loss of material and by simultaneously preserving the zeolite structure in its integrity has been reported and are detailed further below.

3.2.4. Surfactant-templated mesostructuring of zeolites after dissolution

Recently, a top down method has been reported for creating mesopores in zeolite crystals that avoids the loss of material, and simultaneously preserves the zeolite structure.[39,73] The approach is to use a single-step process that combines surfactant templating with base treatment to produce single-phase mesostructured zeolites with intracrystalline mesoporosity. The conditions are significantly milder (e.g., dilute NH_4OH solution) than those for desilication. Surfactants such as cetyltrimethyl ammonium bromide or chloride (CTAB or CTAC) have been used to introduce well-controlled mesoporosity into various zeolites types.[73] The pore size distribution of the mesopores created in this way is very narrow and centered at 4 nm. This is very similar to that of the ordered mesoporous material, MCM-41, obtained using this surfactant. There is no evidence of a separate mesoporous phase being formed with this method.

3.2.5. Evaluating porosity strategies

When evaluating strategies for increasing diffusion in zeolites, there are more factors to take into account than just an increase in the total pore volume. The main goals of these strategies, is to improve the accessibility to the active sites, without it outweighing the possible changes to the active sites. Examples of negative impact are irreversible change to the active site species, or a decrease in acid sites due to loss of microporosity or composition change.

For instance, we previously examined this precise issue. Multiple mesoporous TS-1 catalysts were prepared, for the oxidation of pyridine to pyridine N-oxide. The synthesis of the mesoporous TS-1 samples were done using carbon templating (cTS-1), desilication

(dTS-1), and a combination of both (cdTS-1).[74] Figure 3.6 shows the reflectance UV-Vis spectra, with which it is possible to analyze the titanium species in the zeolite. The UV-vis spectrum of conventional and carbon templated TS-1 showed maximum at 210 nm which is attributed to the tetrahedrally coordinated $Ti(OSi)_4$. The desilicated samples showed a small shift in maximum intensity towards 220 nm. This was identified as tetrahedral tripodal $Ti(OSi)_3OH$ and tetrapodal $Ti(OSi)_4$ species. This might be a consequence of an increased surface density of Ti^{4+} due to the desilication process.

The catalytic results showed that cTS-1 was the most active catalyst. It was concluded, that the carbon templating was the most favorable technique of increased access to the active sites, as it preserved the majority of the active sites. Desilication of the TS-1 was however not favorable, as it showed a lower conversion, even though it contained the largest total pore volume, i.e. accessibility to the active sites. The lower conversion of the dTS-1 and cdTS-1, was proposed to be caused by the drastical change in the nature of the titanium species changed to drastically with the desilication.

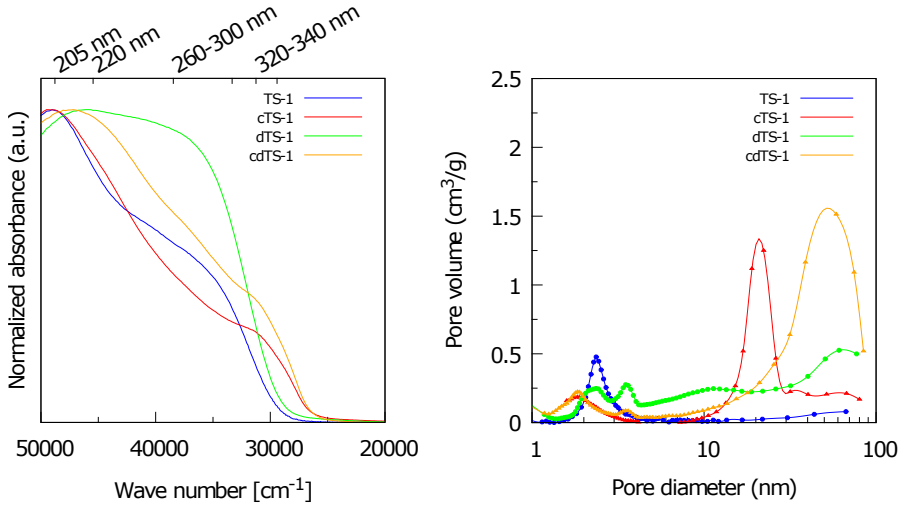

Figure 3.6.: *Reflectance UV-vis spectra nad Barret-Joyner-Halenda derived pore size distribution from 5-100 nm of the prepared TS-1 catalysts. Reprinted with permission from*[74]

In the templating approaches, mesopores can be generated without affecting the framework composition, in contrast to the post synthesis methods, such as desilication. As a consequence, the textural properties (volume and shape of the mesopores) can be tuned by selecting the suitable templates, thus more controllable as compared with the top down methods. The formation of mesopores improves the accessibility of molecules, to and from the acid sites, but also affects the acidity of mesoporous zeolites. In general, mesoporous zeolites have less and weaker Brønsted acid sites in comparison with conven-

tional zeolites.[75] Only the recrystallization with CTAB in a very weak alkaline solution[39] and carbon templating[76] did not cause a decrease in acidity. Despite the loss of a portion of acid sites, the mesoporous zeolites obtained by other templating methods or demetallation showed a distinct improvement in the catalytic activity in numerous reactions. This indicate that the accessibility of acid sites, and not their acid strength, plays a crucial role in the catalytic performance of zeolites.

3.3. Summary

To sum up, zeolites are a group of crystalline materials, exhibit thermal and hydrothermal stability, and have a large surface area, due to their microporosity. These micropores allows for molecular sieving through different types of selectivity. In addition, their flexible chemical composition allows for many different types of framework, as well as capabilities to act as solid acids, or in redox reactions. It is these physical characteristics that make zeolites an favorable catalyst in many large scale applications. The micropores impose however diffusion limitations which significantly reduces the transport of molecules to and from the active sites. The delayed transport of reactants may lead to unwanted side products, catalyst deactivation, and poor utilization of the zeolite.

By generating a second pore system, often mesopores, in the zeolite, the diffusion limitations can be alleviated. This can be done by employing a hard secondary template during zeolite synthesis such as carbon, or extracting framework atoms through acid or base treatment. The different strategies might affect the chemical composition of the zeolite, and as a result, the catalytic active sites. Generally it has been proven that it is the accessibility of the active sites, and not the composition, that has the largest impact on the catalytic performance of zeolites.

Chapter 4.

Synthesis of mesoporous zeolites through in situ carbon templating

---

This chapter reports an effective method to introduce mesoporosity in zeolites, through the in situ formation of a carbon matrix over metal nanoparticles. The mesoporous catalyst was tested in a model reaction of the conversion of n-octane, and outperforms the conventional zeolite significantly. Lastly, this section explores factors that allow for change in porosity, zeolite structures and metal nanoparticles used.

Zeolites inherent ordered micropore structure and tunable acid properties are the reason the materials are highly utilized as a solid catalysts in petrochemical processes. The micropores can however impose limitations on the catalytic performance. The small pores with diameters of molecular dimensions, restrict the accessibility of reactants to the active sites in the interior of the zeolite. This inhibits full utilization of the catalyst. Several groups have explored a multitude of strategies to overcome the diffusion limitations imposed by the micropores of the zeolite. One possible route is to generate intracrystalline mesopores. There are several strategies to achieve this, detailed further in 3.2. For the generation of mesopores in zeolites, carbon applied as a hard secondary template have been proven to fulfill several criteria. It has been showed as a versatile method in the sense, that several different mesoporous zeolite types have been successfully synthesized with this template. Commonly, no change in composition, microporosity, and acidity compared to the conventional counterpart is observed. The active sites in the interior of the zeolite should therefore be equal, and the only difference is increased accessibility. It is not a destructive technique, as compared to . In addition, by choosing the right carbon template, it is possible to obtain the desired mesopore volume and connectivity of the

mesopore network in the zeolite. While a lot can be stated about the benefits of carbon templates, they are not industrally viable at this stage. One of the reasons why, is the sizeable price of the carbon templates, which can be in the price range of several thousand euros ,€. In addition, large amount of carbon template are usually required, as well as the limitation of not being able to recycle the template. All in all, these restrictions make current carbon templates unactractive for generation of mesopores in zeolites.[60]

Here, a novel method of producing mesoporous zeolites is presented. This is done with carbon nanofibers as a hard secondary template. The overall synthesis process is displayed in Figure 4.1. The carbon fibers are synthesized through chemical vapor deposition by passing methane gas over nickel nanoparticles. The composite is then impregnated with a alkaline solution containing the zeolite gel. After hydrothermal synthesis, the zeolite is calcined to remove the structure directing agent and carbon matrix. The use of ready available amorphous silica and the in situ generated carbon template, should greatly reduces the cost compared to using TEOS as a silica source and previously explored commercial carbon templates.

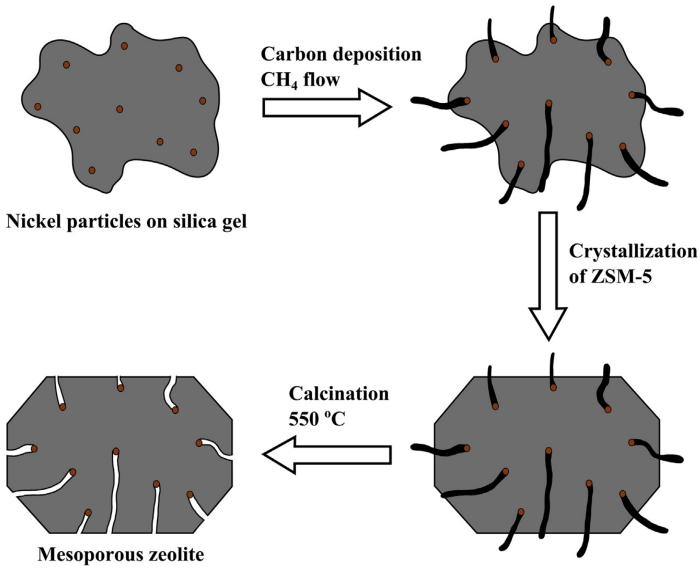

Figure 4.1.: *Overview of the synthesis process: by passing methane over nickel nanoparticles (orange), supported on silica (grey), a carbon matrix is generated in situ as the methane decomposes to coke (black). The obtained carbon/silica composite is then transformed into zeolite during crystallization, incorporating the nickel nanoparticles and carbon. Combustion of the carbon template results in a mesoporous zeolite containing nickel nanoparticles.*

4.1. Carbon nanotubes formation on metal nanoparticles

Carbon formation on metal nanoparticles have been studied dilligently. From the planned production of e.g. carbon nanotubes to the deactivating whisker byproduct in the steam reforming. Typically, carbon nanotubes are prepared by electric arc discharge,[77] laser ablation,[78] and chemical vapor deposition (CVD) of hydrocarbon gases over a catalytic material.[79] The CVD method has been reported to be the most selective in carbon nanotube formation.[80] A metal's activity for hydrocarbon decomposition is not an indication of its ability of CNF formation.[80,81] In some cases, the hydrocarbons will decompose without forming CNFs.[82] Iron, nickel, cobalt, or an alloy of these, have been recognized as highly active catalysts for the growth of CNF.[83–86] For these experiments, nickel was chosen as the catalyst for the formation of the carbon matrix.

4.2. Catalytic cracking with zeolites

In order to determine whether the prepared mesoporous zeolite showed any advantages over conventional zeolite, the hydrocracking of n-octane was chosen as a model reaction. It has been reported that this type of reaction is suitable for evaluating the improved accessibility to the active sites in mesoporous zeolites, compared to its conventional counterpart.[31,87]

4.3. Experimental section

4.3.1. Materials

All reagents were of reagent grade and used without further purifications: Tetrapropylammonium hydroxide (TPAOH, 1 M aqueous solution, Sigma-Aldrich), silica gel (SiO_2, Davisil Grade 62, pore size 150 Å, 60-200 mesh, Sigma-Aldrich), sodium aluminate ($NaAlO_2$, 54 wt% Al_2O_3 and 41 wt% Na_2O, Riedel-de Haen), ammonium nitrate (NH_4NO_3, 98 wt%, Aldrich), Nickel nitrate hexahydrate ($Ni(NO_3)_2 \cdot 6\,H_2O$, Sigma-Aldrich), n-octane (C_8H_{18}, 98%, Sigma-Aldrich), methane gas (CH_4, AGA), forming gas (10% H_2/N_2, AGA), tetrabutylammonium hydroxide (TBAOH, 40 wt%, Sigma-Aldrich), tetraethylammonium hydroxide (TEAOH, 35 wt%, Sigma-Aldrich), sodium hydroxide (NaOH, 97%, VWR), aluminum nitrate ($Al(NO_3)_{3.9}H_2O$, Riedel-de Haen), and distilled water.

4.3.2. Preparation of Ni-containing silica-carbon composite materials

The silica-carbon composite was prepared by the following procedure. 0.15 g of $Ni(NO_3)_2 \cdot 6\,H_2O$ was dissolved in 1.73 g of water. 1.50 g of SiO_2 was impregnated with this solution to incipient wetness (corresponding to 2 wt% Ni loading). The resulting material was dried overnight at room temperature and then calcined in a flow of 10% H_2/N_2 (with a ramp of 20 °C/min) at 600 °C, followed by calcination in a flow of Ar until temperature was fallen to 550 °C. Then flow was changed to a flow of CH_4 and the obtained materials were subjected to it at 550 °Cfor eight hours. A schematic of the CVD setup is presented in Figure 4.2.

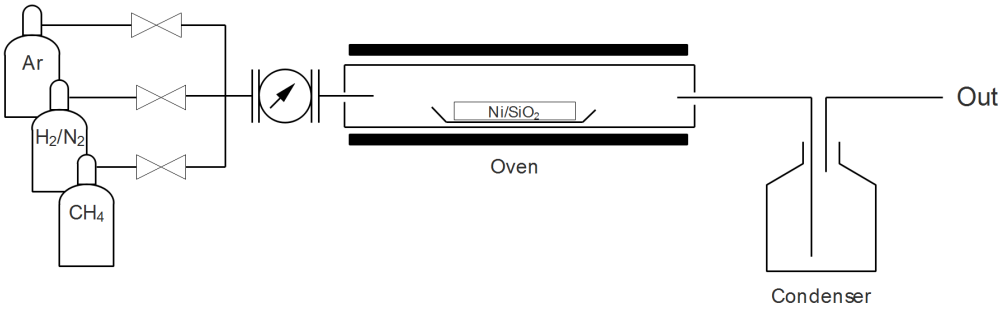

Figure 4.2.: *Schematic of the CVD setup used. The outlet gas is led through an condenser surrounded by dry ice, in order to freeze any volatile organic compounds.*

4.3.3. Synthesis of Ni-zeolite

Synthesis of Meso-Ni-ZSM-5

The mesoporous Ni-containing Na-ZSM-5 material was prepared according to the following procedure. In a 100 ml flask, 8.73 g of TPAOH, 0.60 g of H_2O, and 0.06 g of $NaAlO_2$ was added with stirring until a clear solution was obtained. After that, the Ni containing silica-carbon composite obtained above, Section 4.3.2, was mixed with this solution. After one hour, the final composite material was placed in a teflon beaker inside a stainless steel autoclave, containing 15 ml of water to produce saturated steam, heated to 180 °C and kept there for 72 h. Then, the autoclave was cooled to room temperature, the product was washed with deionized water (1 l) and filtered by suction. Finally, the product was dried at 90 °C for 10 h, and the organic template and the carbon was removed by controlled combustion in air in a muffle furnace at 550 °C for 24 h. Finally, the product was calcined in a flow of 10% $H_2/\ N_2$ (with a ramp of 20 °C/min) at 600 °C

for 4 h.

Alongside Meso-NiHZSM-5, three samples were synthesized with the following change in synthesis parameters: After the Ni-containing silica-carbon composite material was impregnated with the solution of TPAOH, $NaAlO_2$, and H_2O, Meso-NiHZSM-5 [20h] was allowed to stand at room temperature with stirring for 20 hours. Sample Meso-NiHZSM-5 [$\div H_2$] was not reduced in 10% $H_2/_2$ before being exposed to the methane gas at 550 ℃. Meso-Ni-HZSM-5 [8h H_2] was reduced in 10% $H_2/_2$ for eight hours.

The conventional Ni-containing Na-ZSM-5 material was prepared as the mesoporous sample, with the exception that the nickel silica material had not been subjected to methane.

Synthesis of Meso Ni-ZSM-11

The mesoporous Ni-containing Na-ZSM-11 material was prepared according to the following procedure. In a 100 ml flask, 3.16 g of H_2O, 0.14 g of NaOH and 0.21 g of $Al(NO_3)_3 \cdot 9\,H_2O$ were added with stirring and mixed with the Ni-containing silica–carbon composite obtained from Section 4.3.2. Then, 3.18 g of TBAOH was added to this mixture. The final composite material was placed in a Teflon beaker inside a stainless steel autoclave, containing 15 g of water to produce saturated steam, heated to 175 ℃ and kept there for 24 h. Then, the autoclave was cooled to room temperature, the product was washed with deionized water (1 l) and filtered by suction. Finally, the product was dried at 90 ℃ for 10 h, and the organic template and the carbon were removed by controlled combustion in air in a muffle furnace at 550 ℃ for 24 h. For the synthesis of the conventional sample, the Ni-silica composite was not exposed to any methane.

Synthesis of Meso Ni-BEA

The mesoporous Ni-containing Na-Beta material was prepared according to the following procedure. In a 100 ml flask, 0.08 g of NaOH, 1.74 g of H_2O, 0.17 g of $NaAlO_2$ and 4.25 g of TEAOH were added with stirring until a clear solution was obtained. After that, the Ni-containing silica–carbon composite obtained from Section 4.3.2 was impregnated with this mixture. The final composite material was introduced into a stainless steel autoclave, containing 15 g of water to produce saturated steam, heated to 140 ℃ and kept there for 144 h. Then, the autoclave was cooled to room temperature, the product was washed with deionized water (1 l) and filtered by suction. The zeolite was dried at 90 ℃ for 10 h, and the organic template and the carbon were removed by controlled combustion in

air in a muffle furnace at 550 ℃for 24 h. For the synthesis of the conventional sample, the Ni-silica composite was not exposed to any methane.

Synthesis of Meso Ni-Zeolite Y

The synthesis of mesoporous FAU-type crystals was based on the recipe from the patent by Christensen et al.[88] In a typical synthesis procedure, the freshly prepared chemicals were used: sodium silicate (200 g l^{-1} SiO_2), sodium aluminate solution (240 g l^{-1} Al_2O_3), sodium hydroxide solution (400 g Na_2O l^{-1}). The mesoporous NaY material was prepared using seed gel according to the following procedure. Seed gel was made by the following recipe: in 100 ml flask 9.3 ml of sodiumaluminate solution (240 g L^{-1} Al_2O_3), 19.97 mL of sodium hydroxide solution (400 g l^{-1} Na_2O) and 50 ml of sodium silicate (200 g l^{-1} SiO_2) were added slowly with stirring. After that the mixture was left for 4 hours. Synthesis gel was prepared by the following procedure: in 100 ml flask 4.4 ml of sodium aluminate solution (240 g l^{-1} Al_2O_3), 2.35 ml of sodium hydroxide solution (400 g l^{-1} Na_2O) and 5.46 mL of sodium silicate (200 g l^{-1} SiO_2) were added slowly with stirring. After that, the Ni-containing silica–carbon composite obtained as described in Section 4.3.2 and 0.48 ml of seed gel was added slowly. The mixture was left for 1 hour with stirring. Then the gel was introduced into a stainless steel autoclave, containing 15 g of water to produce saturated steam, heated to 100 ℃ and kept there for 18 h. Then, the autoclave was cooled to room temperature, the product was washed with deionized water (1 L) and filtered by suction. The zeolite was dried at 90 ℃ for 10 h, and the carbon template was removed by controlled combustion in air in a muffle furnace at 550 ℃ for 24 h. For the synthesis of the conventional sample, the Ni-silica composite was not exposed to any methane.

Catalysts preparation

All acidic zeolite samples (Ni-HZSM-5) were prepared by the following ion-exchange procedure. The H-form of each zeolite was prepared by three consecutive ion-exchanges, starting with the corresponding Na-form (1 g of sample) and 1 M aqueous NH_4NO_3 solution (80 ml) at 80 ℃. The filtered NH_4-form of zeolite was washed with deionized water (1 l) after each exchange and allowed to dry in air. Finally, the ion-exchanged product was heated in air at 550 ℃ for 5 h to produce the desired H-form of the zeolite.

4.3.4. Characterization

X-ray powder diffraction

X-ray powder diffraction patterns were recorded in transmission mode using Cu-Kα radiation from a focusing quartz monochromator and a Huber G760 Guinier camera in the 2θ interval 5-80°. All xrpd measurements were performed by Lise Lotte Berring.

Nitrogen physisorption

All nitrogen physisorption analysis were performed at liquid N_2 temperature on a Micromeritics ASAP 2020. The samples were outgassed in vacuum at 200 ℃during 18 h prior to measurement. The (apparent) total surface area was calculated by the BET method. Micropore volumes, V_{micro}, were determined using the t-plot method. The total sorbed volume, V_{total}, including adsorption in the micropores and mesopores and on the external surface, were calculated from the amount of nitrogen adsorbed at relative pressure $p/p_0 = 0.95$. Pore size distributions were derived from the BJH method using the desorption branch.

Electron microscopy

Scanning electron microscopy (SEM) was performed on Quanta 200 ESEM FEG operated at 10 kV, and spot size of 2.0. The calcined zeolite samples were placed on a carbon film and Au was evaporated onto the samples for 5 seconds. This was done in order to achieve sufficient conductivity and avoid charging. Transmission electron microscopy (TEM) of the majority of the samples, was performed on a FEI Tecnai microscope operated at 200 kV. The samples were dispersed directly on holey carbon grids. TEM images were all taken by Jerrik Mielby.

Temperature programmed desorption

Temperature programmed desorption of ammonia (NH3-TPD) was performed on a Micromeritics Autochem 2920. Prior to the adsorption of ammonia, the sample was heated to 600 ℃in helium. Desorption of ammonia was performed in a flow of helium using a heating ramp of 15 ℃/min.

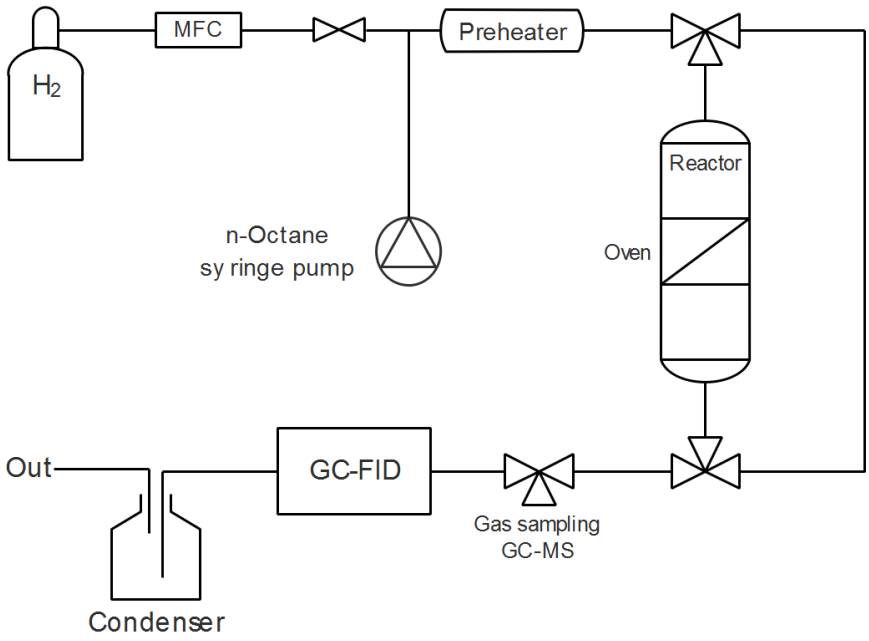

Figure 4.3.: *Schematic illustration of the experimental flow-setup.*

4.3.5. Catalytic experiments: cracking and isomerization of n-octane

In the n-octane conversion experiments, 100 mg of fractionated catalyst (180-355 μm)was placed into a 3 mm stainless steel fixed bed reactor. Afterwards, n-octane was pumped into an evaporator at 180 ℃ together with H_2 (50 ml/min) and the preheated gas was then passed through the reactor. All activity measurements were performed under the same reaction conditions using a preprogrammed temperature profile from 300 to 500 ℃ increasing with 1 ℃/min. The product gas was periodically analysed every 20 min by an online GC-FID equipped with a standard nonpolar column. All major products were identified from gas samples by GC-MS and by the retention time of authentic samples on the online GC-FID. Each catalyst was tested three times in order to obtain a fair picture of the activity. A schematic of the flow setup is presented in Figure 4.3.

4.4. Results and Discussion

4.4.1. X-ray powder diffraction

Figure Figure 4.4 shows the diffraction data for the two prepared samples, after the zeolite crystallization and subsequent calcination. Both samples show sharp and intense

diffraction peaks at 8°and 9°, combined with the other well defined peaks, it is evident that the samples exhibit the characteristic diffraction pattern of a ZSM-5 structured zeolite. None of the samples display peaks from metallic nickel, which are marked by vertical lines at 2θ values of 44.5°, 51.94°, and 76.42° (JCPDS, Card No. 04-850). The reason for this could be the possible small size of the nanoparticles, or that the signal from the zeolites overlaps.

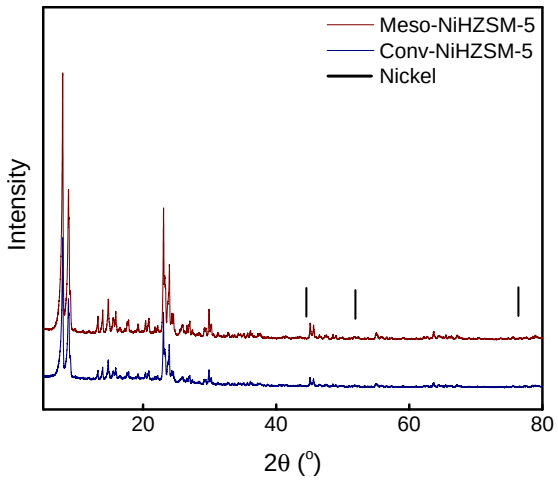

Figure 4.4.: *XRPD diffragtograms of the mesoporous and conventional zeolite, containing nickel. The vertical black lines are for possible identification of nickel particles.*

4.4.2. Nitrogen physisorption

The nitrogen physisorption isotherms are displayed in Figure Figure 4.5A. Meso-NiHZSM-5 exhibit a type IV(a) isotherm, with hysteresis loop at relative pressure higher than p/p_0=0.4. This indicates the presence of mesopores, with a width over 4 nm, within the sample.[7] The hysteresis loop is a type H4 which is common for some mesoporous zeolites.[7] This type of loop is associated with cylindrial pores, as well as limited pore blocking in inkbottle mesopores.[51] The high uptake of nitrogen at very low relative pressure (p/p_0<0.05) in both samples, is associated with filling of micropores. The additional porosity in the mesoporous zeolite, is broad and centered around 17 nm, as seen from Figure 4.5B. This is very common for carbon templated zeolites.[40] The pore size distributions are cut off to exclude a peak near 2 nm. This is regarded as an artifact of the BJH method due to the closing of the two hysteresis loop. While the isotherm for Conv-NiHZSM-5 shows some type H4 hysteresis, it shows no other pore system than the inherent micropores in Figure 4.5B.

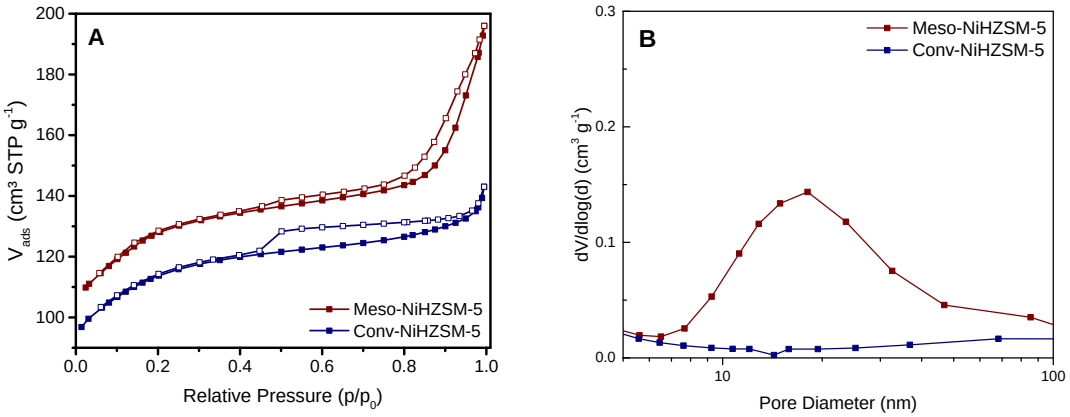

Figure 4.5.: *(A) N_2 physisorption isotherms of the prepared materials. The isotherm for Meso-NiHZSM-5 is offset by 10 for illustrative purposes. (B) Barret-Joyner-Halenda derived pore size distribution from 5-100 nm.*

Table 4.1 displays the data gained from the nitrogen physisorption, as well as elemental data determined by ICP. The (apparent) total surface area was calculated by the BET method, the micropore volume was calculated by the *t*-plot method and the total pore volume was determined from the isotherm adsorption branch by a single point close to p/p_0. The data showed an increase in the . Previously, it has been reported that mesoporous zeolites synthesized with carbon nanofibers exhibited a lower microporous volume. The calcination temperature of the carbon nanofibers and zeolite might have been too low to remove all the carbon. Remaining carbon could decrease the micropore volume per gram.[51] Concerning the Meso-NiHZSM-5, there was no change in the micropore volume compared to the conventional counterpart. This could be an advantage as it is an evidence of the mesopores are not created on the expense of the micropores. It is possible that the nickel blocks some of the pores.

Table 4.1.: *Nitrogen physisorption and elemental data.*

Sample	Si/Al[a] ratio	V_{micro}[b] (cm^3g^{-1})	V_{total}[c] (cm^3g^{-1})	S_{BET}[d] (m^2g^{-1})	Ni content[a] (wt%)
Meso-NiHZSM-5	39	0.17	0.28	429	1.9
Conv-NiHZSM-5	42	0.17	0.20	388	1.7

[a] Determined by ICP. [b] Calculated by the *t*-plot method. [c] Determined from the isotherm adsorption branch at around P/P_0=0.95. [d] Calculated by the BET method.

The aluminium content in zeolites is an important parameter, as it affects the number and strength of the Brønsted acid sites, as well as ion exchange capability. Through ICP

analysis, it was confirmed that the Si/Al ratio in Meso-NiHZSM-5 is comparable to that of the conventional zeolite. This does not equal, that the two samples have the same acidity. To determine that, NH_3-TPD was performed and is reported on later.

4.4.3. Electron microscopy

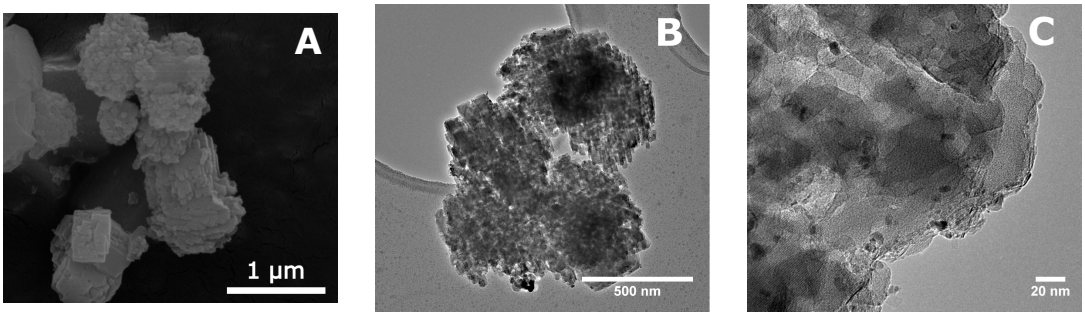

Figure 4.6.: *Electron microscopy images of the Meso-NiHZSM-5 sample. (A) SEM of a representative part of the sample. Overview of the zeolite particles in TEM (B), and a closeup of the mesopores and nickel nanoparticles (C).*

Figure 4.6 shows the scanning- and transmission electron microscopy images obtained of the Meso-NiHZSM-5 sample. From the SEM it is possible to discern that the zeolite crystals are very uniform, and around 1 μm in size. The crystal size of 1 μm is in good agreement with what have been previously reported, for mesoporous ZSM-5 synthesized with carbon as a hard secondary template.[40] Other groups have reported crystal sizes in the area of 15 μm, when using amorphous silica instead of TEOS for zeolite synthesis.[51] A large crystal size increases the risk of encapsulating the carbon nanofibers in the zeolite, causing the mesopores to have no connection to the external surface. In addition, no unconverted amorphous silica was observed.

The mesopores are clearly visible in Figure 4.6C, and are determined to be around 15 nm in diameter. This is very well in agreement with the N_2 physisorption data obtained in Section 4.4.2. The mean nickel nanoparticles diameter is 6 nm, determined by measuring ~100 particles. Unstructured material outside the zeolite crystals were detected. One possibility is the formation of nickel phyllosilicate during the hydrothermal zeolite synthesis. Generally, these are prepared through precipitation of nickel onto a silica surface by under hydrothermal conditions.[89] However, the characteristic peaks were not observed in XRPD. This might not be a definitive answer to whether the nickel phyllosilicate is present, as the strong peaks from the zeolite can overlap. Another possibility is that the material is the remains of the carbon matrix. A solution to both

situations would be to increase the calcination temperature.[90]

The electron microscopy images of the conventional zeolite are presented in Figure 4.7. The particles are around 1 μm, and very uniform in both size and shape. From Figure 4.7B, it is evident that the zeolite is solid, and not containing any other porosity than the inherent microporosity. The nickel nanoparticles are situated on the outer surface of the zeolite, Figure 4.7C, and are determined to be around 6 nm, by measuring ~100 particles.

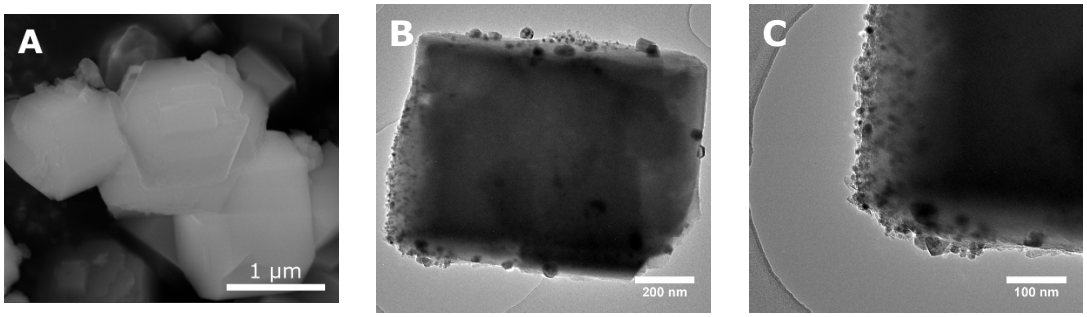

Figure 4.7.: *Electron microscopy images of the Conv-NiHZSM-5 sample. (A) SEM. TEM images of a zeolite crystal (B) as well as nickel nanoparticles (C).*

As it is possible for nickel to be active in reactions with hydrocarbons, as demonstrated above, removal of nickel before catalytic application might be an advantage. It is possible to remove nickel through several methods. The extraction of nickel with ethylenediaminetetraacetic acid, EDTA, is one of such possibilities. It is possible to recycle the EDTA, making it a feasible method.[91] Exposing a zeolite to EDTA is however a proven demetallation route to generate mesopores.[92] Using this method is therefore not possible when analyzing the results of this in situ carbon templating method. The structure and composition of the zeolite will change after being treated with EDTA, as is common in demetallation methods. Another possibility, is to from the volatile nickel tetracarbonyl compound. $Ni(CO)_4$ is formed easily by the direct reaction of carbon monoxide and finely dispersed nickel, at relative low temperatures.[93] The reverse reaction is the basis of the Mond process, used for the purification of nickel. The health concerns for $Ni(CO)_4$ and CO, must however not be ignored, as both molecules are toxic. This may prevent this route from being applied in larger scales.

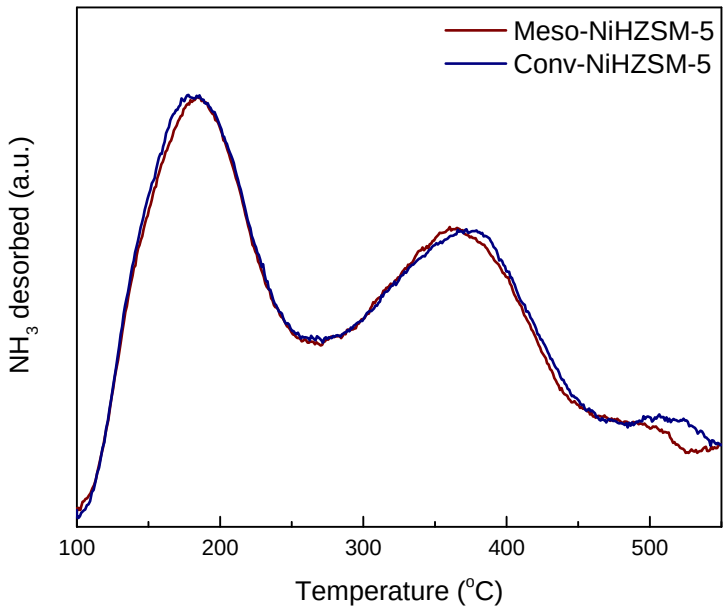

Figure 4.8.: *TPD of meso and conv zeolite*

4.4.4. Temperature programmed desorption

A common quality of using a carbon template, is the preservation of the Si/Al ratio and the microporous system in the produced mesoporous zeolites. As a result, the acidity of a mesoporous zeolite should be equal to that of its conventional counterpart. Previous characterization have showed that the microporosity and Si/Al ratio of Meso-NiHZSM-5 and Conv-NiHZSM-5 are equal. This is however not evidence enough, as the calcination of the carbon template could lead to partial amorphization mesoporous zeolite, which in turn leads to a lower acidity.[94]

Temperature programmed desorption of ammonia, was chosen as a method to relatively determine the acidity of the zeolite samples. The basis of the analysis is based on the strong acid-base adsorption between ammonia and the zeolite's acid sites. After saturation with ammonia, the sample is heated and ammonia will desorb at a temperature given by the strength of the acid site. The amount of desorbed ammonia is then determined with a thermal conductivity detector.

As can be seen from Figure 4.8 the acidity of the two samples are identical. This was to be expected, as studies have reported that carbon templated zeolites exhibit the same amount of acidity as their conventional counterparts.[76,95] The difference in activity must therefore be a consequence of an improved mass transfer to, and from, the active sites.

4.4.5. Catalytic activity

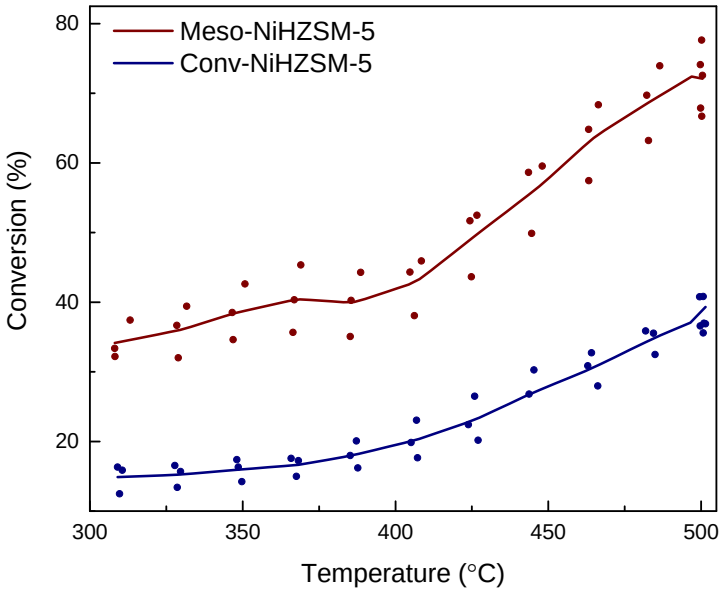

Figure 4.9.: *Conversion of n-octane over mesoporous and conventional zeolites.*

Increased total pore volume is not a guarantee that a certain mesoporous zeolite is, in the end, better than its conventional counterpoint. As explained in refsubsec:evaluating, .

many of the mesopore zeolite materials obtained through carbon templating, show a noticeable reduction in the micropore volume as compared with the conventional ones. This implies partial amorphization of the samples during calcination.[94] In addition the simple presence of mesopores inside the crystals does not necessarily translate itself into an automatic benefit for the diffusion of ingoing molecules, if access to them is provided through the zeolite micropores, that is, if there is no actual connectivity among the mesopores.

In order to determine whether or not the mesoporosity of Meso-NiHZSM-5 have any positive effect, it was tested in the model reaction of cracking and isomerization of the long chain alkane n-octane. This was done alongside Conv-NiHZSM-5 for comparison. Figure Figure 4.9 shows the catalyst performance in terms of conversion of n-octane. Clearly, there is a pronounced effect of the presence of mesopores in the catalysts, which can be attributed to the enhanced diffusion properties of the mesoporous zeolite compared to the conventional zeolite catalyst.

Screening zeolite catalysts at the laboratory scale

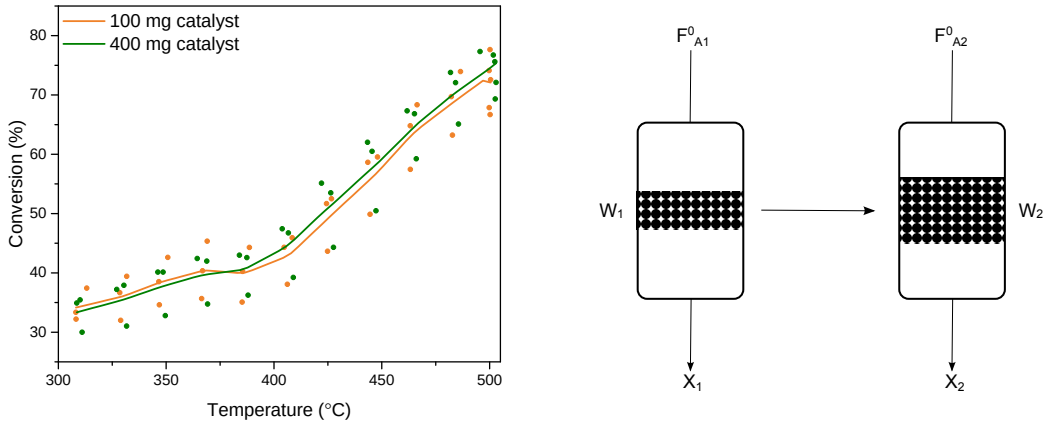

Figure 4.10.: *Test for external mass transfer limitations.*

In order to ascertain the distinctive activities of heterogeneous catalysts, it is crucial to choose the correct reaction conditions. The chemical reaction occurring can generate gradients of heat and concentration around and within the catalyst particles. Correct reaction conditions take these matters into account, and aim to minimize any effect on the catalytic activity. A series of experimental test were performed to ensure that no limitations, mass or heat, were placed upon the intrinsic activities of the catalysts. All tests were done using the conversion of n-octane with the Meso-NiHZSM-5 catalyst.

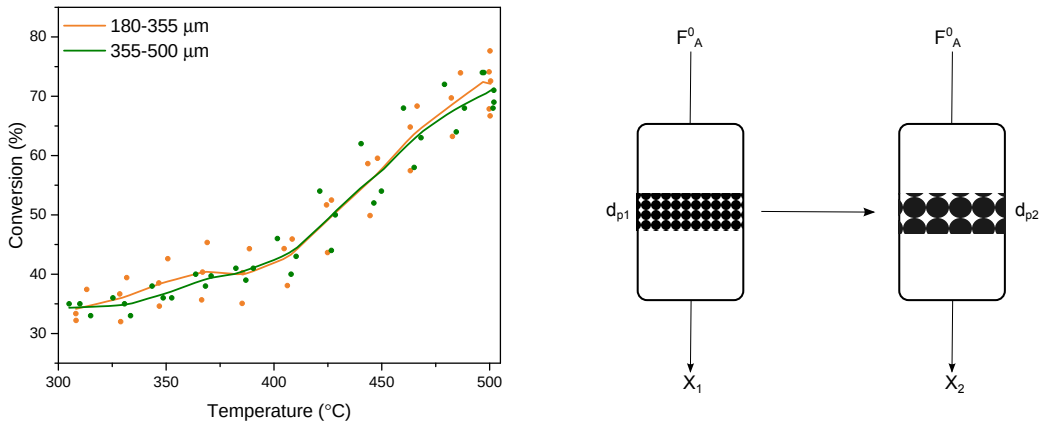

Figure 4.11.: *Test for internal mass transfer.*

Mass transfer limitations occur due to hampered diffusion of reactants and products. External mass transfer limitations are imposed by poor diffusion between catalyst particles. A control experiment for this can easily be done by increasing the catalyst weight,

while keeping the space time, W_i/F^0_{Ai}, constant. If no external mass transfer limitations are present, the conversion for the two experiments will be the same.

Figure 4.10 shows the results of the test for external mass transfer limitations. It is clear that there are no serious change in the catalytic conversion, with increased flow of reactants. The reaction is therefore not inhibited by external mass transfer limitations at these reaction conditions.

While external mass transfer is between the catalyst particles, internal mass transfer is the diffusion of molecules inside the catalyst particle. Here, an experiment was done to exclude any limitation based on the particle size of the catalyst. Two particle size fractions, 180-355 μm and 355-500 μm, were tested and compared. If any internal mass transfer is present, the conversion is dependent on the particle size. As Figure 4.11 shows no significant difference in the conversion, it is safe to assume that there are no internal mass transfer limitations, under these reactions conditions. Total exclusion of the limitations presented by the intra-zeolitic pore diffusion, is however a greater challenge as explained in Section 3.[66]

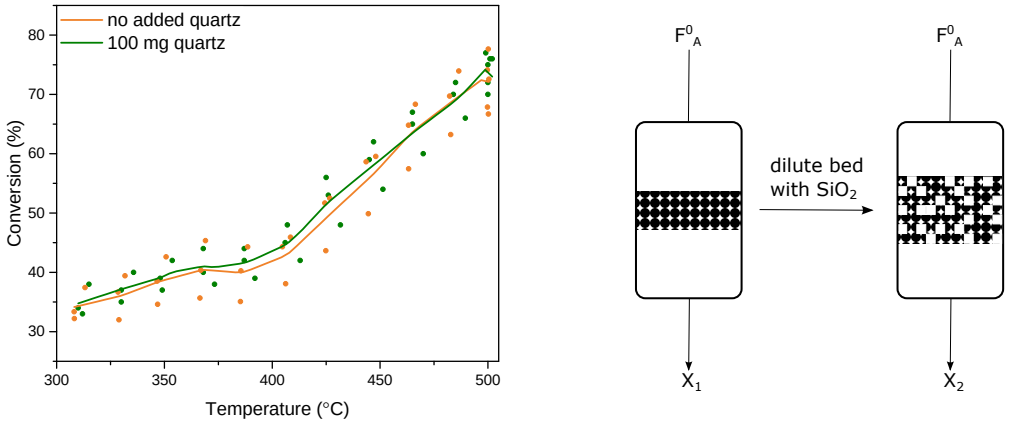

Figure 4.12.: *Test for heat gradients in the catalytic bed.*

By diluting the catalyst bed with an inert material, it is possible to test for any temperature gradient. If any is present, lower conversion will observed for exothermic reactions and a higher conversion for endothermic reactions. Figure 4.12 shows the results of these tests. The catalyst bed was diluted with 100 mg SiO_2. As can be seen, the conversion did not change with the dilution of the catalytic bed. There is therefor no temperature gradient under the chosen reaction conditions.

4.4.6. Varying the porosity

As a results of the initial proof of concept, it was examined whether the porosity of the mesoporous zeolites could be affected by varying the process parameters. Three samples were prepared according to Section 4.3.3, but to summarize: Meso-NiHZSM-5 [20h] was left for 20 hours under stirring instead of one hour after the impregnation of SDA, water, and alumina source. This was done in an effort to mix the carbon template and the synthesis gel, in order to better confine the crystallization. Meso-NiHZSM-5 [÷H_2] were not treated with hydrogen before being exposed to CH_4. Meso-NiHZSM-5 [8h H_2] were treated with hydrogen for 8 hours before the flow was changed to CH_4.

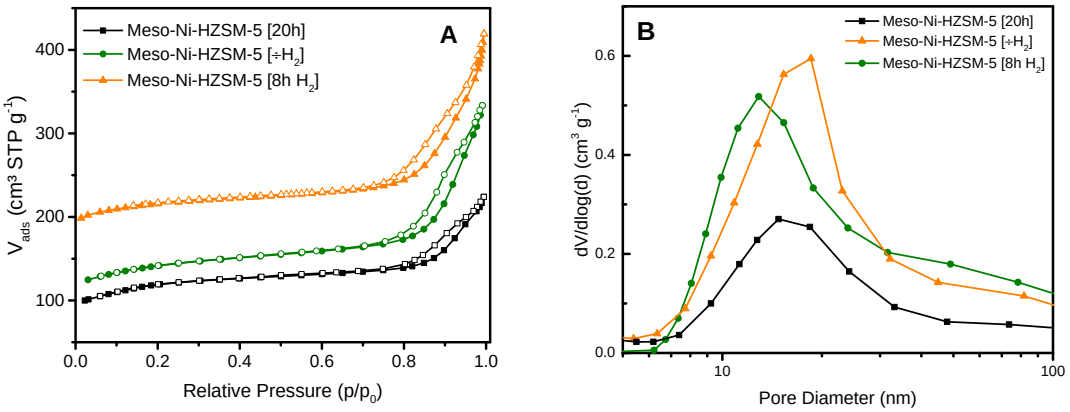

Figure 4.13.: *(A) N_2 physisorption isotherms of the prepared catalysts. The isotherms for Meso-Ni-HZSM-5 [20h] and Meso-Ni-HZSM-5 [8h H_2] have been offset by 20 and 100, respectively, for illustrative purposes. (B) Barret-Joyner-Halenda derived pore size distribution from 5-100 nm.*

Table 4.2.: *Nitrogen physisorption data.*

Sample	V_{micro} [a] (cm^3g^{-1})	V_{total} [b] (cm^3g^{-1})	S_{BET} [c] (m^2g^{-1})
Meso-Ni-HZSM-5 [20h]	0.11	0.40	443
Meso-Ni-HZSM-5 [÷H_2]	0.12	0.46	432
Meso-Ni-HZSM-5 [8h H_2]	0.13	0.48	448

[a] Calculated by the *t*-plot method. [b] Determined from the isotherm adsorption branch at around P/P_0=0.95. [c] Calculated by the BET method.

The nitrogen physisorption isotherms and BJH derived pore size distributions of the three samples are presented in Figure 4.13. The isotherms are very similar to the one reported in Figure 4.5. They are all type IV(a) isotherm, with hysteresis loop at relative

pressure higher than p/p_0=0.4. The H4 hysteresis loop is associated with cylindrial pores, as well as limited pore blocking in inkbottle mesopores. The steep uptake of nitrogen at very low relative pressure (p/p_0<0.05) can be contributed to the filling of micropores. The pore size distribution is centered around 12-20 nm for the three samples. Mixing the synthesis gel and the carbon template for a longer time, Meso-NiHZSM-5 [20h], results in a higher pore volume. The reason for this, could be due to an improved confinement of the synthesis gel in the carbon template. The fact that Meso-NiHZSM-5 [÷H_2] displays mesoporosity, suggests that the reduction step with hydrogen is uneccesary. The conditions during the CVD are suitable for the nickel nanoparticles to form. Meso-NiHZSM-5 [8h H_2] showed a much higher total pore volume than the sample reduced for only 4 hours. The increased reduction time, might have resulted in a higher dispersion of the nickel nanoparticles, leading to higher carbon formation.

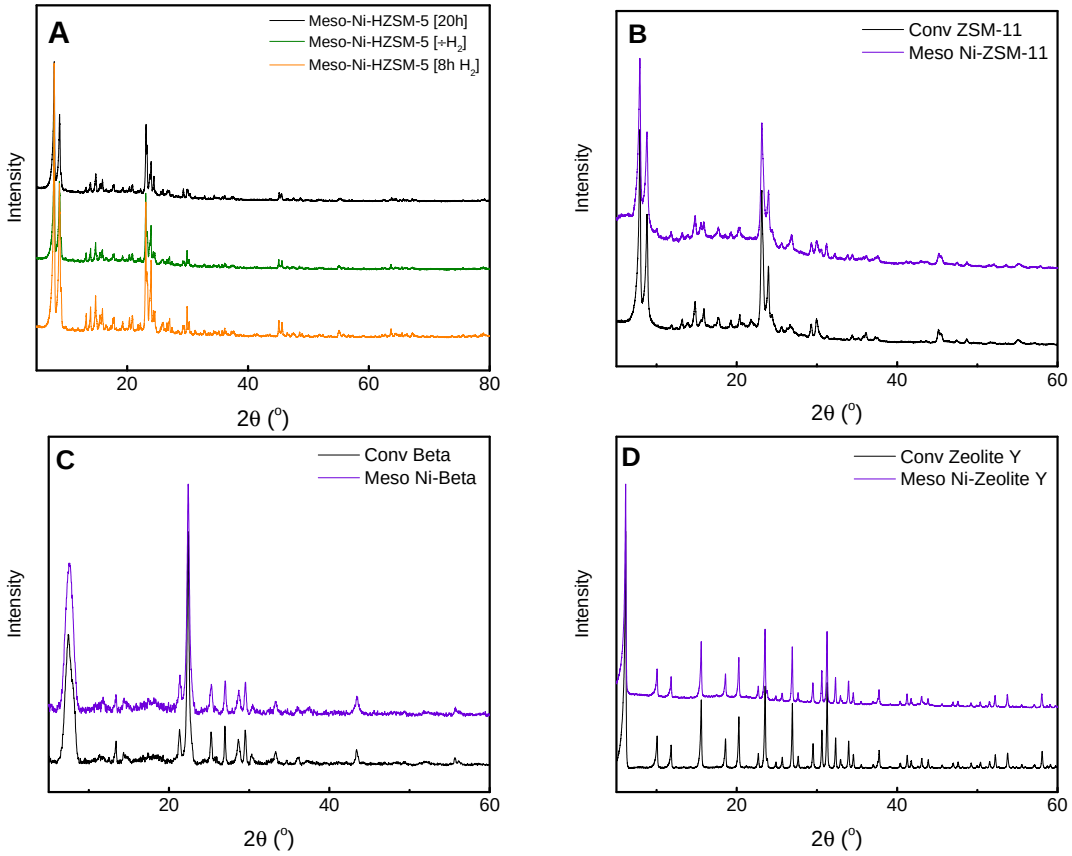

Figure 4.14.: *XRPD diffractograms of the synthesized zeolite samples.*

The data obtained from the nitrogen physisorption is given in Table 4.2. All samples contained a larger total pore volume than the sample presented in 4.4.2. This is a clear

indication that the process can be optimized further.

Figure 4.14A displays the X-ray diffractograms of the synthesized samples. Varying the synthesis method, did not result in any observable change of the crystal structure. All three samples exhibit clear and well defined peaks characteristic of the ZSM-5 type zeolite.

Future experiments might involve a series of samples with different CVD durations, where the sample is being exposed to CH_4. The determination of an optimal CVD duration could reduce the overall synthesis time, as well as minimizing use of reagents.

4.4.7. Expanding on zeolite types

Up until now, the presented method of synthesizing mesoporous zeolites, have only been described ZSM-5 structured zeolites. Here, mesoporous ZSM-11, Beta, and Zeolite Y, are synthesized using the in-situ carbon templating. The samples are characterized thoroughly in order to verify whether or not this synthesis strategy is general.

Figure 4.14 displays all obtained XRPD patterns of the synthesized ZSM-11, Beta, and Zeolite Y zeolites. It should be evident that the mesoporous samples matches their conventional counterpart in both crystallinity and structure. All XRPD patterns were obtained after the combustion of the organic template and carbon material, where applicable.

Nitrogen physisorption isotherms and pore size distribution for the prepared conventional and mesoporous ZSM-11, Beta, and Zeolite Y samples are all presented in Figure 4.15. All prepared mesoporous zeolites have a Type IV isotherm, with a type H4 hysteresis loop, starting at p/p_0=0.4. In addition, the isotherms all have an upward curvature at relative pressures above 0.8. These characteristics are the same observed for the Meso-NiHZSM-5, and are also common for other carbon templated zeolites. The (apparent) BET surface area and pore volumes obtained, are presented in Table 4.3 alongside elemental analysis data.

It is apparent that the total pore volume of mesoporous NiZSM-11 and NiBeta, have increased by a large amount through this method of using an in situ generated carbon template. NiZeolite Y only shows a slightly more pronounced hysteresis than the conventional Zeolite Y. In addition the BJH derive pore size distribution shows only a modest increase in porosity. Neither of these results are however affecting the total pore volume, where there are no difference between the conventional and the (attempted) mesoporous zeolite sample. A reasonable explanation for this could be the different procedure for the

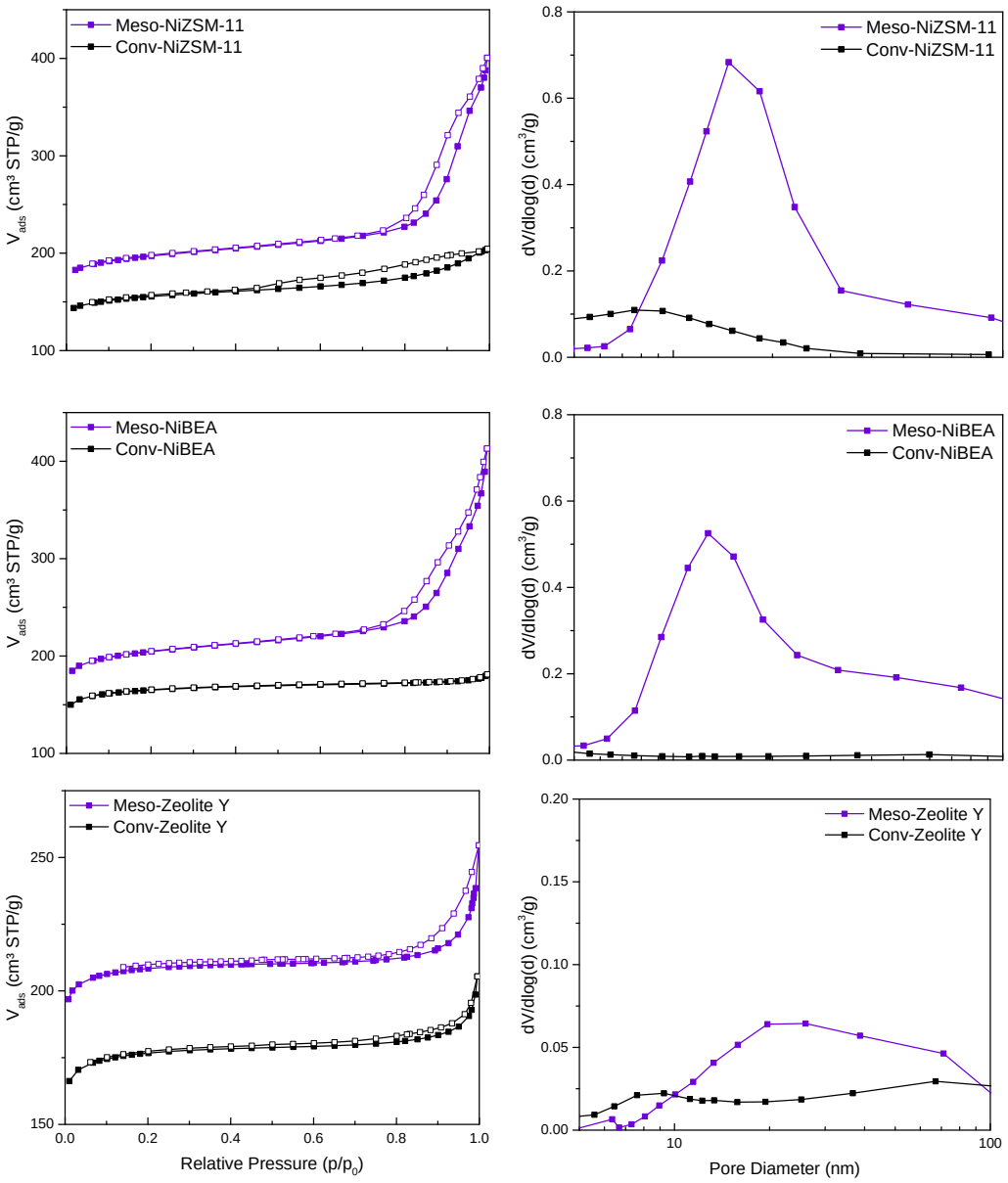

Figure 4.15.: *N_2 physisorption isotherms of the prepared catalysts. Barret-Joyner-Halenda derived pore size distribution from 5-100 nm.*

Table 4.3.: *Nitrogen physisorption and elemental data.*

Sample	Si/Al[a] ratio	V_{micro}[b] (cm^3g^{-1})	V_{total}[c] (cm^3g^{-1})	S_{BET}[d] (m^2g^{-1})
Meso NiZSM-11	88	0.13	0.41	397
Conv ZSM-11	88	0.14	0.22	409
Meso NiBeta	24	0.18	0.44	522
Conv Beta	22	0.22	0.27	553
Meso NiZeolite Y	4.4	0.32	0.34	853
Conv Zeolite Y	4.6	0.33	0.35	886

[a] Determined by ICP. [b] Calculated by the *t*-plot method. [c] Determined from the isotherm adsorption branch at around P/P_0=0.95. [d] Calculated by the BET method.

synthesis gel compared to the other samples. As explained in Section 3.2.1 to hinder the synthesis gel from migrating away from the confined space, a separation of the synthesis gel and the liquid phase is required. As the preparation for the Zeolite Y does require large amount of water in the synthesis gel, it is quite possible that the synthesis gel is not confined in the carbon template. One possible solution to this is to use different experimental parameters for the CVD process. It is possible to vary the carbon template, and as a result the final porosity of the sample, as showed in Section 4.4.6. The Si/Al ratio are not noticeable different between the mesoporous and conventional samples, this is the same result observed with the Meso-NiHZSM-5, and expected as explained in Section 3.2.5.

The samples were analyzed by electron microscopy as a way to gain supplemental knowledge about structure, morphology, and porosity. Electron microscopy images of the conventional and mesoporous ZSM-11 are presented in Figure 4.16. The average crystal size of Meso NiZSM-11 was determined to be around 3 μm from SEM images. The mesopores in Meso NiZSM-11 are clearly visible as lighter areas in the crystals in Figure 4.16C. In order to gain useful information from TEM, the imaging was done on much smaller crystals so that the electron beam was able to travel through the sample. The Beta zeolite crystals, presented in Figure 4.17A+B, are very uniform with an average size of 1 μm for both the conventional and mesoporous sample. The TEM image in Figure 4.17 shows the presence of intracrystalline mesopores. Figure 4.18 displays the two Zeolite Y samples. As expected from the N_2 physisorption, there are not any noticeable differences between the two samples. This strengthens the argument that the synthesis was not successful for the generation of mesoporous zeolites.

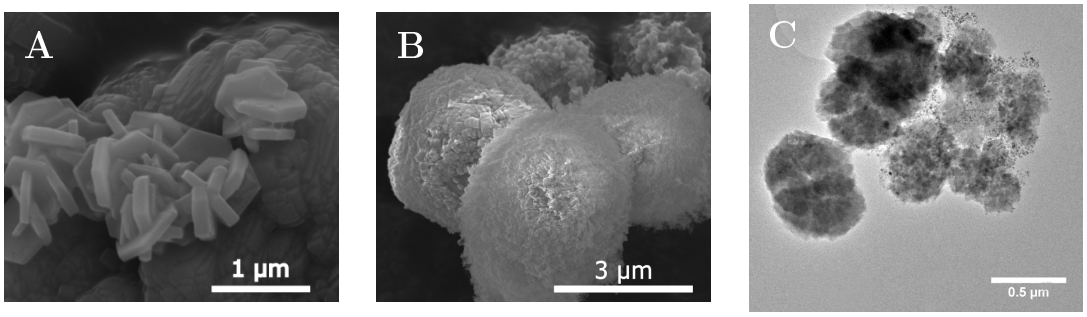

Figure 4.16.: *Electron microscopy images of the ZSM-11 samples. (A and B) SEM of a representative part of the conventional and mesoporous sample respectively. (C) TEM overview of Meso NiZSM-11.*

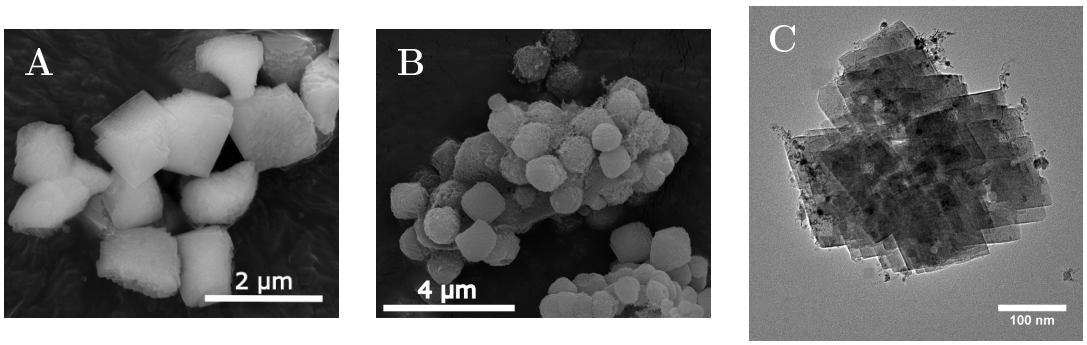

Figure 4.17.: *SEM image of Conv Beta (A) and Meso NiBeta(B). TEM of a Meso NiBeta (C) with visible mesopores and nickel nanoparticles.*

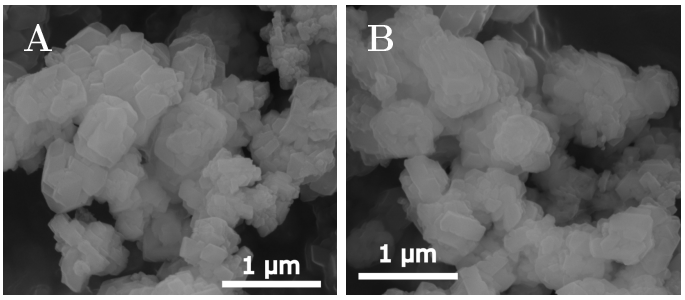

Figure 4.18.: *SEM images of (A) Conv Zeolite Y and (B) Meso NiZeolite Y.*

4.5. Summary

In this chapter, the synthesis of mesoporous zeolites with a carbon secondary hard template is reported. The preparation was based on the decomposition of methane over nickel nanoparticles supported on silica. This lead to the in situ formation of carbon, which was used as a hard secondary template for the preparation of mesoporous zeolites. Mesoporous HZSM-5 was produced and matched the conventional counterpart in terms of crystallinity and acidity, while exhibiting a larger total pore volume. The method was shown to create varying porosity with changes in the experimental parameters. Lastly, the method was successfully applied to ZSM-11 and Beta type zeolites.

Chapter 5.

Fundamentals of polymer electrolyte membrane fuel cells

This chapter describes the fundamentals of a polymer electrolyte membrane fuel cell (PEMFC). Common degradation mechanisms such as particle dissolution, Ostwald ripening, agglomeration, particle detachment, and carbon corrosion will be discussed. Through modification of the catalyst support, it is possible to lessen the degradation. Examples of these strategies are also taken up in the chapter.

Electrochemical processes are expected to play a key role in the implementation of sustainable energy technologies in our future energy systems.[96] Fuel cells hold great promise for the chemical energy conversion of small molecules. These energy carriers include hydrogen, methanol, and ethanol. During the last decades, fuel cell technology have experienced a significant progress, bringing it closer to large scale applications.[97–99] In the present chapter, some of the fundamentals of fuel cells will be explained. This include subjects such as working principle, types of fuel, common degradation mechanisms, and design of a nanostructured Pt/C catalyst for fuel cell application.

Fuel cells are categorizes in two groups based on the operation temperature: high temperature fuel cells, with an operating temperature in the range of 100 - 1000 ℃, and low temperature fuel cells that operate below 100 ℃. While this is effective from an application point of view, a more precise classification can be done according to the electrolyte used. The five most common technologies are: polymer electrolyte membrane fuel cells (PEMFCs), alkaline fuel cells (AFCs), phosphoric acid fuel cells (PAFCs), molten carbonate fuel cells (MCFCs), and solid oxide fuel cells (SOFCs). The PEMFC will be the only type discussed further, as Section 6 deals with designing a novel catalyst

for this type of fuel cell.

5.1. Working principle of PEMFC

The process of chemical energy conversion into electricity in PEMFCs occurs through direct electrochemical reactions. The component responsible for the chemical energy conversion, is the membrane electrode assembly (MEA), which consists of three main parts: cathode, membrane and anode. PEMFCs use a polymeric electrolyte with side chains containing acidic functional groups that allow the transport of protons between the electrodes. The membrane is sandwiched between the two electrodes, where the electrochemical fuel oxidation (anode) and oxidant reduction (cathode) reactions take place. The functions of the membrane are to conduct protons and to avoid gas permeation to the other side of the cell. The fuel and oxidant are provided to the device from external sources.[100]

In hydrogen fuelled PEMFCs, hydrogen is decomposed at the anode into positively charged protons and negatively charged electrons. The protons diffuse through the polymer electrolyte membrane (PEM) to the cathode, whereas the electrons are conducted via an external circuit to the cathode, generating an electric current. At the cathode, the electrons, protons, and oxygen react in the oxygen reduction reaction (ORR) producing water as the only reaction product, which flows out of the cell. A schematic of the above mentioned process is given in Figure 5.1.

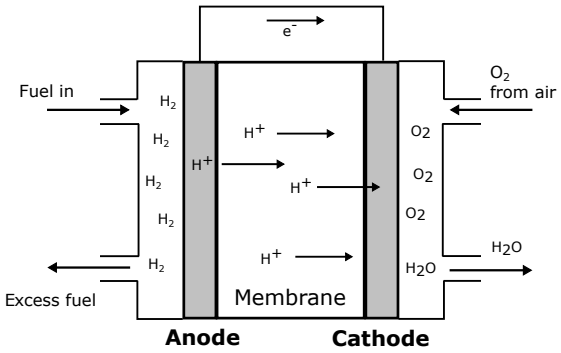

Figure 5.1.: *Schematic of a membrane electrode assembly for PEMFC.*

The anode and cathode catalyst typically consist of platinum or platinum alloy nanoparticles supported on high surface area carbon supports. At the anode side, in H_2-PEMFCs the splitting of the hydrogen molecule is relatively easy using platinum based catalyst.[100] However, the splitting of the oxygen molecule is less favorable, causing significant acti-

vation losses. Nevertheless, platinum based catalysts are still the best option for the oxygen reduction reaction (ORR).[100,101]

As mentioned, Pt/C is the default catalyst for operating with pure hydrogen streams. The majority of H_2 produced is through the reforming of hydrocarbons, which can contain small amounts of CO, which deactivates the catalyst. For operation with with CO-contaminated H_2, PtRu/C catalysts offer superior performance.[100]

5.2. Small organic molecules as electrooxidative fuel

For some applications, e.g. mobile and portable, hydrogen based fuel cells have raised some concerns. This is mainly the high cost of miniaturized hydrogen containers, potential dangers in the transport and use of hydrogen, and the low gas-phase energy density.[102] One way to bypass these barriers, is to develop materials for hydrogen storing where the hydrogen can easily be handled. A numerous amount of potential carriers have been identified, sch as ammonia or liquid organic hydrogen carriers.[103,104] Another possible way, is to use small organic molecules, e.g. methanol, ethanol, and formic acid, as fuel.

Direct Methanol Fuel Cells (DMFCs) uses methanol used directly as fuel. Methanol is liquid at ambient conditions, has low production costs, and is in principle renewable when produced from biomass. The power densities of DMFCs are generally 5–10 times lower compared to PEMFCs. DMFCs are therefore mostly used in low power applications such as cell phone chargers and laptop power supplies.[100] A lot o research have gone into the design of DMFCs, but the technology is not without some complications. First of all, the low electrocatalytic oxidation rates of the anode results in lower electrical efficiencies. Secondly, methanol permeation through the membrane from the anode to the cathode side simultaneously reduces fuel utilization, poisons the cathode catalyst, and decreases cell performance.[100,102,105] In addition, the inherent toxicity of methanol, is an issue for the commercialization of DMFCs.[102]

The high volumetric and gravimetric power density of liquid ethanol are significant advantages of Direct Ethanol Fuel Cells (DEFCs). However DEFCs are currently less effective than DMFCs due to sluggish alcohol oxidation kinetics.[99,100]

Direct Formic Acid Fuel Cells (DFAFCs), use formic acid as fuel, and have received an increasing interest in the recent years. As with the two above mentioned techniques, the fuel is liquid at ambient conditions. Formic acid suffers however from its low volumetric

power density of only 2.1 kWh l^{-1}, compared to that of methanol which is 4.7 kWh l^{-1}. In the litterature, there are discussions whether or not this disqualifies DFAFCs for low power mobile applications.[100,102,106]

5.3. Degradation of PEMFC electrocatalysts on the nanoscale

For practical performance of a fuel cell, high activity is not the only criteria. High stability against the aggressive conditions that occur in the fuel cell under operation, is also a requirement.[107] An efficient fuel cell catalyst needs to preserve its activity over an extended lifetime and to avoid degradation under operation. A value often linked to the degradation, is the loss the electrochemically active surface area (ECSA). A gradual loss of ECSA will inevitably lead to efficiency losses, and can eventually reach unacceptable levels. For standard Pt/C catalysts, indications for a variety of different degradation mechanisms are reported and summarized in the literature.[107–110] Figure 5.2 provides an overview of the catalyst degradation mechanisms that have been suggested to occur in hydrogen fuel cells. The improvement of the catalyst durability is considered as equally important as the activity improvement.[111,112]

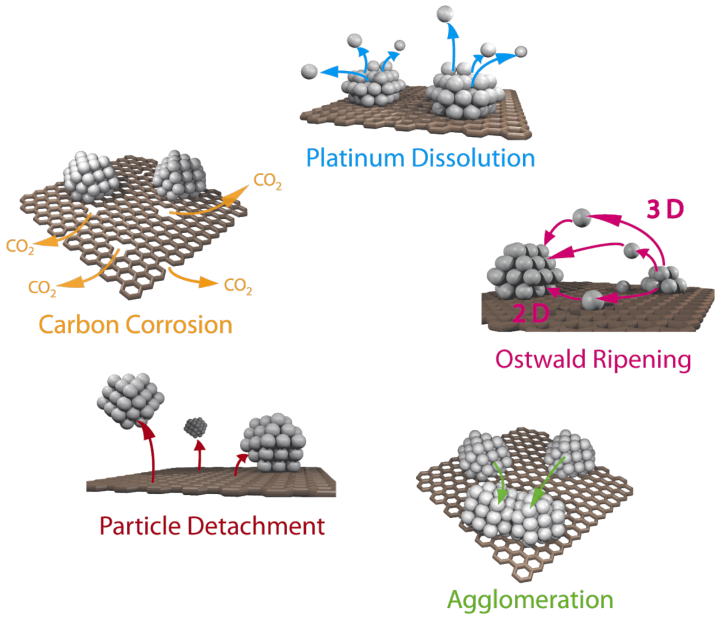

Figure 5.2.: *Simplified representation of suggested degradation mechanisms for platinum particles on a carbon support in fuel cells. Adapted from Meier et al.*[113]

5.3.1. Platinum dissolution

One type of degradation is the dissolution of platinum. This occurs during operation, and have been proven in a variety of studies. Platinum have been detected in the water stream that exits the fuel cell, or to have been redeposited in the membrane.[114–116] Platinum dissolution is expected to be especially severe for smaller platinum particles, which have a higher surface energy and are thus considered to dissolve already at lower potentials than bulk platinum.[117,118] If the dissolved platinum is redeposited on larger platinum particles, significant particle growth can occur and the according degradation mechanism is called Ostwald ripening.

5.3.2. Sintering - Particle migration, agglomeration, and Ostwald Ripening

Particle growth is one of the most common mechanisms for loss of catalytic activity in heterogeneous catalysis. The growth of supported metal nanoparticles is referred to as sintering and it results in loss of active surface area. In fuel cell catalysts, particle growth is the result of Ostwald ripening and particle migration with further agglomeration.[115] Ostwald ripening occurs as a two step process. Small nanoparticles are dissolved into solution, and the dissolved species are redeposited onto larger particles. This mechanism leads to an overall increase of particle size, and therefore a reduction in catalytic activity. The driving force behind this process is the reduction of surface energy of the particles.

It has been reported that there are two mechanisms in fuel cells for particle growth due to agglomeration: agglomeration as a result of carbon corrosion and agglomeration caused by particle migration. In the first case, the carbon support is oxidized and as a consequence platinum particles adjacent to each other come into contact, and finally agglomerate when the support corrodes.[119] Agglomerations and subsequent coalescence of Pt nanoparticles supported on highly graphitic supports was shown by Schlögl et al. to be the main degradation mechanism.[120] The reason for the employment of the highly graphitic carbon supports, is that they exhibit superior stability against carbon corrosion. So the majority of the degradation would come from other sources than the shrinking of the support.

A recent review on the mechanisms of sintering by Hansen et al.,[121] found that the degradation occurs differently. Through in situ TEM and Monte Carlo simulations, they suggested that Ostwald ripening was responsible for initial sintering, which causes a rapid decrease in catalytic activity. After the disappearance majority of the small

nanoparticles, the sintering was a turned to a combination of Ostwald ripening and particle migration. This disagreement on the sintering mechanism, might be caused by the experiments performed. Hansen et al. reviewed and performed experiments on metal nanoparticles with metal oxide supports, e.g. Pd/SiO_2, at temperatures of up to 900 ℃in air. At these conditions the sintering mechanism of metal nanoparticles might be different from the mechanism observed in fuel cells.

5.3.3. Particle detachment

Several investigations have suggested detachement of Pt nanoparticles from the carbon support during degradation tests. The size distribution of the platinum particles did not change significantly, but a decrease in particle population was observed.[122,123] Particle detachment have also been observed to simultaneously occur with agglomeration.[119,120,124] These pathways are both ascribed to a weakened particle-support interactions. This is believed to be the cause of carbon corrosion, which platinum can catalyse.[125]

5.3.4. Carbon corrosion

Carbon corrosion is oxidation of framework carbon to CO and CO_2. This type of degradation can lead to loss of structure, resulting in collapse and a considerable shrinking of the catalyst layer.[126,127] Particle agglomeration and detachment have been proven to be direct consequences of this.[119] Besides triggering the above mentioned degradation pathways, the loss of structure and porosity can also result in mass transport limitations for the reactants.[128] Carbon corrosion have been suggested to occur faster on the internal part of carbon particles, as these often consist of low-ordered carbon phases. Well-ordered graphene-like shells have proven to be more resistant towards carbon corrosion.[129] These suggestions were successfully proven by IL-TEM (Identical Location TEM) by Schlögl et al.[119] Figure 5.3 show IL-TEM images of a Pt/C sample before and after degradation treatment. The resulting materials showed signs of lower carbon density, Figure 5.3 B, and carbon shrinkage, Figure 5.3 D.

5.4. Designing a successful carbon support

To produce cost competitive materials, the literature has paid particular attention to the improvement of electrocatalyst activity. This has resulted in nanostructured platinum or platinum alloy catalysts with impressive activities.[130,131] However, the stability of

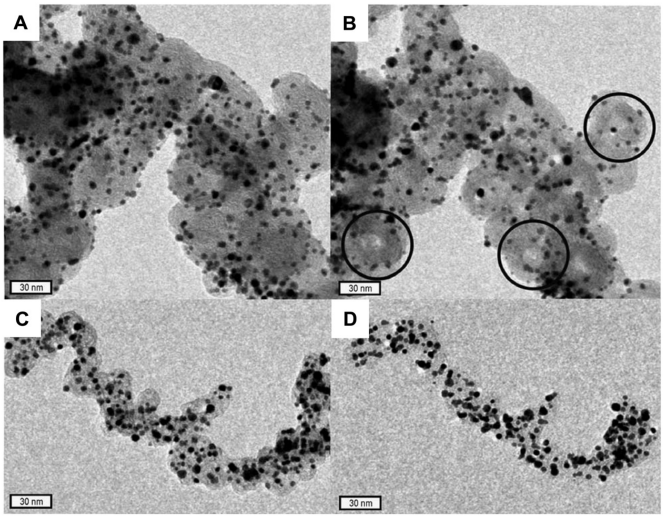

Figure 5.3.: *Example of carbon corrosion for a Pt/C catalyst. Before (A and C) and after (B and D) 16 hours potential hold at 1.3 V_{RHE} at 75 ℃. (B) shows indications of corroded hollow-like structures. (D) shows a catalyst location with shrinkage of the carbon support. Adapted from Schlögl et al.*[119]

such materials under operation conditions of fuel cells still remains a challenge. Thus, improvement of electrocatalyst durability currently is one of the most important issues.[132] To address this instability issue, several approaches have been proposed at the material level. One possible strategy is to use other supports than carbon. A wide variety of materials such as metal oxides, -carbides, and -nitrides have reported promising corrosion resistances under fuel cell conditions. However, most of these non-carbon materials suffer from low conductivities and/or poor platinum dispersion, thus limiting the efficiency of the fuel cell.[108]

Below, three methods of increasing the effectiveness of carbon supported Pt catalysts, are presented. First, encapsulation of the platinum nanoparticles will be described. This strategy have been shown to greatly increase the resistance towards sintering. Secondly is the introduction of heteroatom, e.g. nitrogen, doping of the carbon support. This procedure generates materials that have been shown to increase both electrochemical activity and stability. thirdly, the graphitization of carbon support will be discussed. Carbon support containing graphitic domains exhibit a higher resistance towards carbon corrosion.

5.4.1. Encapsulation of nanoparticles

Encapsulating nanoparticles is an interesting concept, and has been covered in several reviews.[133,134] By using this technique for fuel cell catalysts, is has been proven possible to prevent or slow down some of the common degradation mechanism such as particle detachment and agglomeration.[135] One of such examples are presented in Figure 5.4. Here, individual gold nanoparticles are encapsulated in hollow carbon spheres. These type of hollow shells containing nanoparticles, are often referred to as a yolk-shell particles.

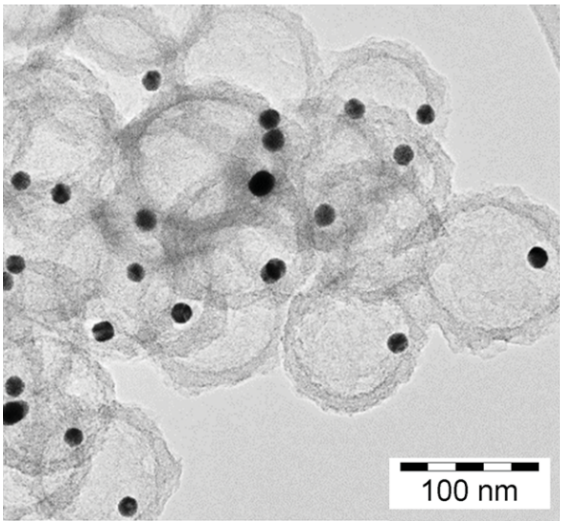

Figure 5.4.: *Gold nanoparticles encapsulated in carbon shells. An example of a yolk-shell particle. Adapted from Galeano et al.*[135]

In yolk-shell particles agglomeration of particles located in different spheres and detachment of particles is completely suppressed.[135] In addition, since the nanoparticles are relatively monodispersed the driving force for Ostwald-ripening is very low. For yolk-shell systems to be suitable for electrocatalysis applications, there are some criteria to follow. The carbon shell should possess adequate conductivity for fuel cell applications. It also requires sufficient porosity, in order to allow the transport of electrolyte and gaseous reactants to the encapsulated metal nanoparticle. In addition, the metal loading has to be as high as possible to achieve significant reaction rates

5.4.2. Nitrogen doping

In order to improve nanoporous carbon supports with novel physical and electrochemical properties, heteroatoms such as boron, nitrogen, sulfur, fluorine, and phosphorous have

been doped into carbon frameworks. Nitrogen doped carbons have been investigated as metal-free catalysts, and as catalyst support for electrochemical energy conversion systems.[136–138] N-doped carbons have been proposed to generate favorable metal-support interactions, which significantly enhance catalyst activity and stability.[139,140]

Preparation of N-doped carbon materials can be divided into two main groups: In situ doping and postsynthesis doping methods. The first strategy involves the carbonization of nitrogen containing precursors, either through pyrolysis or chemical vapor deposition. This can be done with or without a hard template. An example of the former is the carbonization of furfuryl alcohol in a nitrogen rich porous organic framework.[141] These type of processes often results in carbon materials with disordered nanopores.[142] In situ doping can also be nanocasted in the aid of a hard template, such as mesoporous silica and aluminosilicate.[143] This method ensures the uniform distribution of nitrogen species, and allows for predetermined ordered porous carbon materials. The second strategy for doping with nitrogen, is to treat carbon materials in a nitrogen containing atmosphere, e.g. NH_3 at high temperatures.[144] This method has been widely used for nitrogen functionalization of carbon materials and usually requires the preoxidation of the carbon surface or the aid of transition metals for the incorporation of the nitrogen species into the carbon network.

Studies indicate that introducing nitrogen into carbon supports, influence three parameters:[139]

- Different nucleation and growth kinetics during catalyst nanoparticle formation, which results in higher particle dispersion and smaller particle size.
- Increased catalyst-support interaction, which might result in enhanced durability.
- Modification of catalyst nanoparticle electronic structure, which might enhance intrinsic catalytic activity.

X-ray photoelectron spectroscopy (XPS) is a technique often employed, in order to determine the structural, chemical, and physical nature of N-doped support materials. Groups have reported the presence of multiple nitrogen species, including pyridinic, pyrrolic, quaternary/graphitic, and oxide forms.[145–148] Figure 5.5 provides an overview of the various nitrogen species observed in the N-doped carbon supports. Because of the complex nature of these materials, and the overlap in binding energy in XPS, it is difficult to identify and correlate specific nitrogen species with improved performance.[139,149] So

while N-doping is known to enhance activity and stability of fuel cell catalysts, the nature of the introduced nitrogen and their effects on the resulting electrocatalytic properties, are still not fully understood.[139,150]

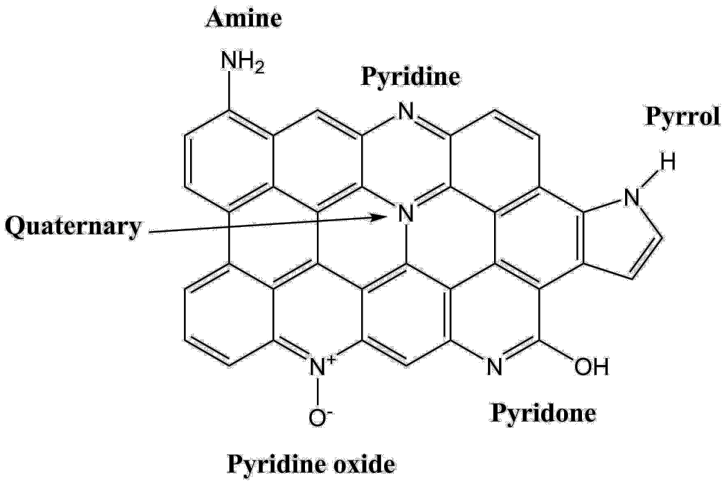

Figure 5.5.: *Structures of the various nitrogen species commonly observed in the N-doped carbon materials.*

5.4.3. Graphitization

Carbon corrosion is regarded as a primary degradation process, and can be the cause for secondary processes such as platinum particle detachment or agglomeration.[113] It is therefore imperative to enhance the stability of the support towards this type of degradation, if durable catalysts are to be realized. One way of accomplishing this, is the graphitization of the carbon support. Through high temperature treatment, either with or without a catalysts, e.g. Ni or Fe, the graphitization process can occur.[151] Graphitic support have been reported in litterature to increase resistance against carbon corrosion.[113,152,153] Although graphitization has shown to increase durability by kinetically delaying the carbon oxidation, the reduction of the surface area upon graphitization leads to a decrease in catalyst dispersion and thus also in mass activity.[113]

5.5. Example of a possible successful carbon support

Novel supports for PEMFC are being pursued in order to improve both activity and durability. As explained above, several design criteria have been identified for a successful support. These include small well dispersed Pt nanoparticles, and resistance towards

carbon corrosion. The polymer described in 1.2, exhibit several properties, that might make it ideal for PEMFC. Firstly, the large surface area of > 1000 m^2 g^{-1}, as well as the narrow pore system, make it possible to obtain well dispersed and possibly confined Pt nanoparticles. Secondly, as every carbon is sp^2 hybridized, the support should possess sufficient conductivity for fuel cell applications. In addition, several nanoporous polymers have been synthesized from nitrogen containing substrates.[4,141] It is not unthinkable, that the PPhen also could be synthesized to contain nitrogen species, i.e. in situ doping of nitrogen.

A 25 wt% Pt/PPhen were prepared from the pure PPhen, described in Section 1.3. A TEM image of the resulting material can be seen in Figure 5.6A. The platinum nanoparticles are well dispersed throughout the support, with a average size of 1.7 nm. After heat treatment, Pt/PPhen-before, no significant change of the support was visible in TEM, displayed in Figure 5.6B. However, due to the high temperature, the Pt nanoparticles agglomerated into larger particles. In another experiment, the polymer was impregnated with the platinum precursor after the heat treatment, Pt/PPhen-after. This was done in order to spare the particles for the severe treatment. From Figure 5.6C, it can be seen that the resulting Pt showed a much smaller size compared to the Pt nanoparticles that had been subjected to the heat treatment. Figure 5.6D shows the Pt nanoparticle size distribution of the different materials. As expected, the sample that were not heat treated, shows the narrowest size distribution, with an average size of 1.7 nm. The Pt particles of Pt/PPhen-before had an average size of 4.3 nm, but exhibited a wide size distribution. By heat treating the PPhen before impregnation with Pt precursor, it was possible to obtain Pt nanoparticles with an average size of 2.5 nm. The size distribution is wider than the Pt/PPhen, and narrower than the sample where the Pt where subjugated to the heat treatment as well. The increase in nanoparticle size, compared to the non heat treated Pt/PPhen, might stem from decreased surface area, or a weakened metal-support interaction. The size of the Pt nanoparticles in Pt/PPhen-after are however still suitable PEMFCs.

To fully evaluate the final material as a fuel cell catalyst, further analysis of the support should be performed. These include pore volume, surface area, and the chemical nature of carbon. As mentioned above, graphitization, is a trade-off between increased durability and a decreased in Pt dispersion. Whether or not this preparation method is favorable concerning both parameters is yet to be determined. Other methods of graphitization, as explained in 5.4.2, might be considered. Further analysis and testing is not part of

the thesis, but in the hands of Max-Planck-Institut für Kohlenforschung.

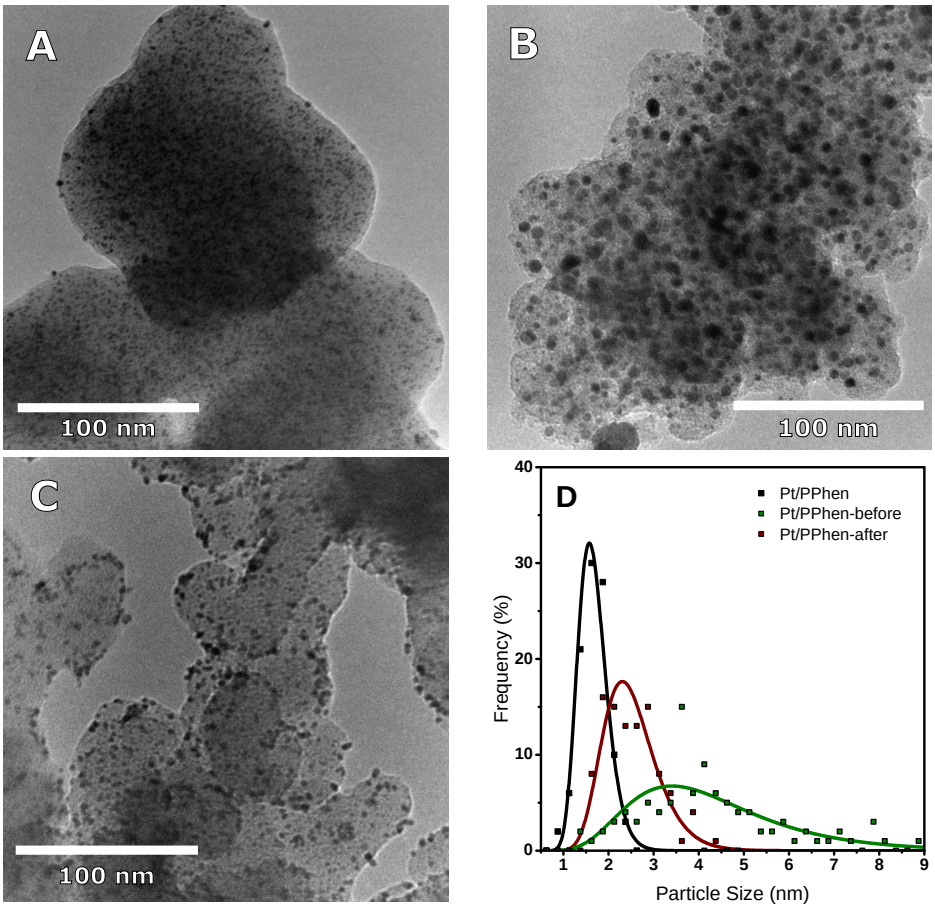

Figure 5.6.: *Representative TEM of (A) Pt/PPhen, (B) Pt/PPhen-before, and (C) Pt/PPhen-after. (D) Lognormal size distributions of the Pt nanoparticles, based on measurements of approximately 100 nanoparticles. Pt/PPhen-before and -after denotes whether the sample is impregnated with platinum precursor before or after heat treatment.*

5.6. Experimental section

5.6.1. Synthesis of Pt/PPhen

Pt/PPhen was produced by impregnating a platinum precursor unto the pure PPhen, followed by reduction. The synthesis of the pure PPhen is decribed in 1.3. $Pt(acac)_2$ (0.403 gram) was dissolved in 0.5 ml of ethanol. The liquid was applied to PPhen and mixed thoroughly. After drying at 60 ℃ for four hours, the solid was put in a tube oven, subjected to an argon atmosphere, heated to 400 ℃ with a ramp of 3 ℃ min^{-1}, and held

there for four hours. After the oven had cooled down, a flow of 2% O_2/N_2 was led over the sample in order to pacify it. The heat treatment of the Pt/PPhen was done at 600 ℃ in Ar, with a ramp of 5 ℃ min^{-1}. This sample is denoted Pt/PPhen-before. A sample was prepared where the PPhen was impregnated with platinum precursor after the heat treatment. This sample is denoted Pt/PPhen-after.

5.6.2. Characterization

TEM of every polyphenylene (PPhen) based material were performed at Max-Planck-Institut für Kohlenforschung. The instrument used was a Hitachi HF-2000 operated at 200 kV. Samples were dispersed in ethanol, and a droplet was placed upon a holey carbon grid. This was allowed to fully dry at room temperature before analysis.

5.7. Summary

Fuel cells are expected to play a key role in the implementation of sustainable technologies in our future energy systems. To bring the technology closer to large scale applications fuel cells should possess a high catalytic activity, as well as high stability over time. Major degradation mechanisms include platinum dissolution and carbon corrosion. There are several techniques on how to alleviate the impact of the degradation on fuel cell catalysts. One method is the encapsulation of the active Pt in carbon yolk-shell particles. This is especially true against degradation mechanisms such as particle detachment and agglomeration, and Ostwald ripening, due to the monodispersed nature of the material. Doping the carbon support with nitrogen improves both the stability and activity of the catalyst. This is done through an strengthened catalyst-support interaction and modification of catalyst nanoparticle electronic structure. The nature of the introduced nitrogen active species and their effects on the resulting electrocatalytic properties are however still not fully understood. Lastly, graphitic carbon supports have a high resistance against carbon corrosion, which is the primary degradation mechanism for agglomeration and detachment. With all the degradation mechanisms identified, and possible method of resisting them, it is possible to produce a fuel cell catalyst that is highly active and durable.

Chapter 6.

Pt encapsulated in hollow nitrogen doped carbon spheres

This chapter reports a novel method of encapsulating small Pt nanoparticles in hollow nitrogen doped carbon spheres. In order to enhance diffusion through the carbon shell, activation with potassium hydroxide were successfully performed. These materials were characterized in order to understand the platinum, the carbon support, and the interaction between them. Electrochemical properties of the catalyst were examined by cyclic voltammetry, as well as electrooxidative catalysis.

Proton exchange membrane fuel cell (PEMFC) is a promising technology for energy conversion, both for local or mobile applications.[154] One of the technical challenges of the PEM fuel cell, is the usage of the expensive element platinum. While ultra-small Pt nanoparticles is by far the most active catalyst for the reaction, Pt is quite expensive, and not an abundant and readily available resource.[155,156] It is therefore crucial to make sure, that the fuel cells operates with a high efficiency as possible. To decrease the amount of Pt in fuel cells in order to reduce the cost, considerable improvements in activity have been achieved over recent years by alloying Pt with transition metals as well as by exploring nonprecious metal catalyst concepts.[130,131] However, the poor long-term stability electrocatalysts under the operating conditions remains a major obstacle.[107] Thus, if electrochemical energy conversion catalysts shall be introduced on a large scale, the state of the art electrocatalysts will require significant improvements in stability.[98,99]

In 5.4 several techniques were discussed on how to design an active and durable catalyst for PEMFC. Building upon these methods a synthesis pathway for the preparation of a novel, platinum based, catalyst is presented. It is based upon nanostructured hollow

nitrogen doped carbon spheres, containing nanosized platinum particles and graphitic domains. The material is also activated by KOH in order to obtain a more porous shell. The resulting materials are characterized regarding both carbon support and platinum nanoparticles. The electrochemical properties of the catalyst were examined by cyclic voltammetry, as well as electrooxidative oxidation of formic acid, methanol, and ethanol.

6.1. General synthesis strategy

The following experiments aim at synthesizing small hollow nitrogen doped carbon spheres, containing nanosized platinum particles, and some degree of graphitic carbon. By producing relative small spheres, it is possible to encapsulate a greater amount of platinum nanoparticles, compared to other reported yolk-shell catalysts.[135] The relative small spheres will also allow for a smaller catalyst layer in the membrane electrode assembly, enhancing the diffusion of reactants. The encapsulation of the Pt nanoparticles should improve the stability of the fuel cell catalyst. This is done by slowing down, or even preventing, coalescence and detachment of metal nanoparticles from the support, platinum dissolution, and Ostwald ripening. As detailed above, the nitrogen doped carbon should result in an increased catalyst support enhance the catalytic activity, improve nanoparticle dispersion as well as stability. Graphitization of the carbon support is done in order to alleviate corrosion of the support and thus further improving the durability. Activation of the samples with KOH were done in order to improve the porosity of the samples. The whole synthesis process is very complex, as every step is prepared in batch. Recently, continuous synthesis of nanostructured silica based materials have been reported.[157] The materials prepared included core-shell particles containing Au nanoparticles. With modifications, this could be applied to the preparation of the first material here, Pt/SiO_2. This would allow for a more practical production of useful electrocatalysts.

KOH activated carbon

The silica spheres used as a template, possesses a limited pore volume, with pore sizes in the microporous region.[158] The carbon sphere produced by nanocasting using these SiO_2 spheres might therefore also exhibit low pore volumes. As detailed above, the carbon shell should posses sufficient porosity, in order to allow the transport of electrolyte and gaseous reactants to the encapsulated metal nanoparticle. Chemical activation using alkali hydroxide is a well established method to generate highly microporous structures

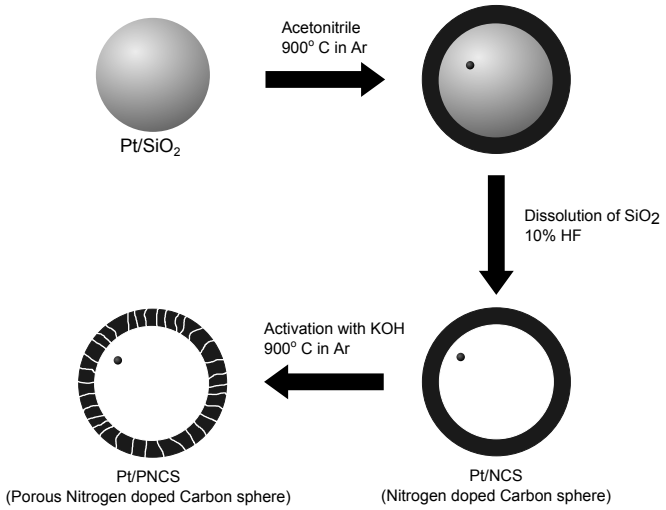

Figure 6.1.: *Scheme for the synthesis pathways of the Pt/NCs and Pt/PNCs.*

for various carbon materials.[159,160] The most common used are NaOH and KOH, where the latter has proven to be most successful when activating ordered carbon structures.[161] At a high temperature, the alkali species is reduced to metal by the carbon species, and the carbon framework is etched to create a large number of micropores due to the oxidation of carbon into carbonate ion. The subsequent removal of the alkali metal species by washing with acid solution may generate additional micropores. With an activation temperature of 900 ℃, significantly higher than the melting point of KOH ($\sim$ 400 ℃), KOH would be present as a liquid and can diffuse into the carbon framework.

6.2. Experimental

6.2.1. Materials

All reagents were of reagent grade and used without further purifications: (3-aminopropyl)-trimethoxysilane (APTMS, 97 %, Sigma-Aldrich), Acetonitrile (CH_3CN, $\geq$ 99.5 %, Sigma-Aldrich), Ammonia (NH_3, 25 % w/w, Sigma-Aldrich), Argon (Ar, 99.99 %, AGA), chloroplatinic acid hexahydrate ($H_2PtCl_{6.6}H_2O$, $\geq$ 37.5 % Pt basis, Sigma-Aldrich), cyclohexane (C_6H_{12}, $\geq$ 99.7 %, Sigma-Aldrich), ethanol (CH_3OH, $\geq$ 99 %, Sigma-Aldrich), formic acid (HCOOH, 98 %, Sigma-Aldrich), hydrochloric acid (HCl, 37 %, Sigma-Aldrich), hydrofluoric acid (HF, 40%, Sigma-Aldrich), methanol (CH_3OH, $\geq$ 99.9 %, Sigma-Aldrich), nitric acid (HNO_3, $\geq$ 99 %, Sigma-Aldrich), polyethylene glycol hexadecyl ether (Brij® C10, Sigma-Aldrich), potassium hydroxide (KOH, $\geq$ 85.5 %, Struers),

sulfuric acid (H_2SO_4, $\geq$ 95 %, TraceSELECT®, Fluka), tetraethyl orthosilicate (TEOS, $\geq$ 99.7 %, Sigma-Aldrich), and distilled water.

6.2.2. Synthesis of Pt/NCS Hollow Nitrogen Doped Carbon Spheres

Pt@SiO_2 Core/Shell nanospheres

For the samples containing 4 wt% platinum, the procedure was as following: 4.25 g of Brij® C10 was mixed with 7.5 ml cyclohexane and 0.5 ml of a 0.0625 M $H_2PtCl_6x_6H_2O$. The mixture was heated to 50 °C under stirring. When the solution became transparent, 0.8 ml 25% NH_3, 150 µl APTMS and 2 ml TEOS was added at two minutes intervals. The solution was then allowed to stir for two hours. Afterwards, the solid was dispersed in ethanol four times, each time collected by centrifugation (five minutes, 3500 rpm). Last, the solid was dried overnight at 80 °C.

Pt/NCS-SiO_2

The silica spheres were placed in a quartz boat, which was subsequently placed in a large tube oven. Argon gas (45 ml min^{-1}) was passed through a Drechsel bottle containing acetonitrile before reaching the tube oven. The sample was heated at 900 °C for three hours, with a ramp of 20 °C min^{-1}. Argon was allowed to bubble through the acetonitrile, and over the sample, for both the heating and the cooling of the sample.

Pt/NCS

The silica spheres with a nitrogen doped carbon shell was put in 10% HF solution. This was allowed to stand under rotation for four hours. The solid was afterwards washed with water and collected by centrifugation, until the pH of the wash water was neutral, and dried at 80 °C for 12 hours.

Pt/PCNS

Activated carbon spheres were prepared through the following method. Pt/NCS were physically mixed with KOH, the weight ratio being 4:1, KOH relative to carbon. This was put in a porcelain boat, and placed in a tube oven. The sample was then heated to 850 °C in argon flow, with a step increase of 5 °C min^{-1}, and held for 1.5 hours. Afterwards the solid were treated with 0.1 M HCl, and washed with water until neutral pH. Lastly the sample was dried at 80 °C for 12 hours.

6.2.3. Characterization

X-ray powder diffraction

X-ray powder diffraction patterns were recorded in transmission mode using Cu-Kα radiation from a focusing quartz monochromator and a Huber G760 Guinier camera in the 2θ interval 5-80°. All xrpd measurements were performed by Lise Lotte Berring.

Thermogravimetric analysis

All TGA were performed on a Mettler Toledo TGA/DSC 1 with an aluminium sample holder. The temperature range was 25-600 ℃, with a ramp of 10 ℃minute^{-1}. TGA measurements were performed Bodil Fliis Holten.

Electron microscopy

Transmission electron microscopy (TEM) of the majority of the samples, was performed on a FEI Tecnai microscope operated at 200 kV. The samples were dispersed directly on holey carbon grids. TEM images were all taken by Jerrik Mielby. The high-angle annular dark-field scanning transmission electron microscopy (HAADF-STEM) imaging was carried out on an FEI Titan 80-300ST field emission gun (FEG) TEM operated at 300 kV. HAADF STEM images were all taken by Dr. Takeshi Kasama from DTU CEN.

X-ray photon spectroscopy

XPS measurements were performed with a Kratos HSi spectrometer with a hemispherical analyzer. The monochromatized Al Kα X-ray source (E=1486.6 eV) was operated at 15 kV and 15 mA. For the narrow scans, an analyzer pass energy of 40 eV was applied. The hybrid mode was used as lens mode. The base pressure during the experiment in the analysis chamber was $4 * 10^{-7}$ Pa. All the carbon samples measured were highly conductive. All XPS binding energies were referenced to the graphitic C 1s signal of the carbon support at 284.5 (± 0.1) eV. The background was corrected with a Shirley-type background. The peaks were fitted with an asymmetric Gauss-Lorentzian peak shape (30% Gauß- and 70% Lorentzian contribution). XPS measurements were performed at Max-Planck-Institut für Kohlenforschung by Dr. Claudia Weidenthaler.

Nitrogen physisorption

All nitrogen physisorption analysis were performed at liquid N_2 temperature on a Micromeritics ASAP 2020. The samples were outgassed in vacuum at 200 °Cduring 18 h prior to measurement. The (apparent) total surface area was calculated by the BET method. Micropore volumes, V_{micro}, were determined using the t-plot method. The total sorbed volume, V_{total}, including adsorption in the micropores and mesopores and on the external surface, were calculated from the amount of nitrogen adsorbed at relative pressure $p/p_0 = 0.99$. Pore size distributions were derived from the BJH method using the desorption branch.

X-ray fluorescence

XRF measurements were conducted on a εpsilon 3-XL from PANalytical with high resolution silicon drift detector (SDD) and X-ray tube excitation (Rh, Ag, and Mo anode materials, 20 kV, 100 μA). Each analysis was repeated ten times.

6.2.4. Electrochemical procedures

Working electrode (WE) used in the experiments was glassy carbon electrode (GCE, ϕ = 4 mm) that was polished with sand paper (# 4000) followed by alumina slurry polishing on 1 μm, 0.3 μm and 0.05 μm. GCE was sonicated in the solution of ethanol (approx. 10 vol. %) in Milli-Q water for 10 min. followed by sonication in Milli-Q water for 2 times 10 min. GCE was then dried in an oven at 60 °C. Glassware was cleaned in boiling 15 % HNO_3 acid. Electrolyte was freshly made, ultra-pure 0.1 M H_2SO_4. Three-electrode electrochemical cell with sample material on GCE as WE, reversible hydrogen electrode (RHE) as reference electrode (RE) and Pt wire as counter electrode (CE) was used. The setup was degassed with Ar flow for 20 min. Electrochemical oxidation was tested in freshly prepared 0.1 M H_2SO_4 + 0.1 M formic acid/methanol/ethanol. Potentials are reported vs. saturated calomel electrode (SCE). All preparation, testing, and analysis of the data where done by Nedjeljko Seselj at DTU Chemistry.

Sample preparation

Pt/NCS was dispersed in 1.0 mL (250 µL of ethanol + 50 µL of 5 % Nafion® in ethanol + 700 µL of Milli-Q water) and sonicated for 15 min. 20 µL of the prepared solutions were drop-casted on GCEs and dried in the oven at 60 °C for 30 min.

6.3. Results and discussion

6.3.1. X-ray powder diffraction

Figure 6.2A shows the xrd pattern of the platinum containing hollow N-doped carbon spheres. The diffraction peaks at 2θ values of about 39.8°, 46.3°, 67.6°, and 81.5° are ascribed to the facets (111), (200), (220), and (311), characteristic of face-centered cubic (fcc) crystalline Pt (JCPDS, Card No. 04-0802). This indicates that the Pt was reduced to the metallic state during the CVD process. In addition, graphitized carbon is present, which is evident from the peak at 2θ = 26.5°, which is attributed to the hexagonal graphite structure.

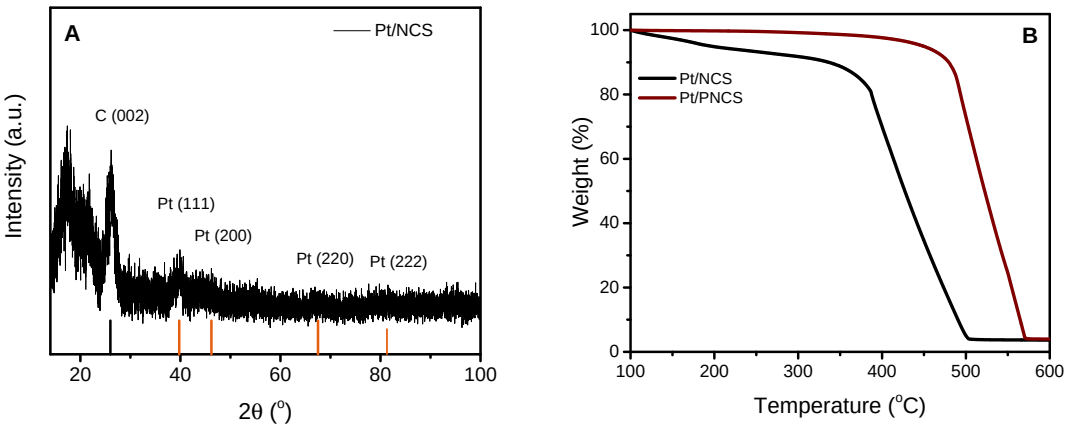

Figure 6.2.: *(A) XRD pattern of Pt/NCS. The black tick represents graphitized carbon, while the orange ones are characteristic peaks for crystalline Pt. (B) TGA curves of Pt/NCS and Pt/PNCS performed in air.*

6.3.2. Thermogravimetric analysis

The Pt content in Pt/NCS was determined by thermogravimetric analysis (TGA). The Pt/NCS and Pt/PNCS were heated to 600 °C in air in order to completely burn the carbon. Any remaining mass corresponded to Pt and non-dissolved silica. The TGA curves are presented in Figure 6.2. The Pt/NCS sample starts to lose mass at relatively low temperatures, which might be attributed to the loss of nitrogen- and oxygen-containing functional groups, and showed that the main weight loss occurs between 400-500 °C. The leftover inorganic mass was determined to be 3.01 weight percent. The main weight loss of the Pt/PNCS sample occured between 500-570 °C, significantly higher than the Pt/NCS sample. One explanation for this, is that the activiation with KOH decreases the

nitrogen content.[162] This has been noted before, to increase the thermal decomposition temperature.[163] The final weight of of Pt/PNCS were determined to be 3.98 % of the initial weight. The small difference in residual mass between the two samples, shows that the activation with KOH does not . This is in good agreement with previously reported carbon materials prepared with KOH activation.[164] In order to determine whether or not, the residual mass is only Pt, subsequent analysis are reported below.

6.3.3. Transmission electron microscopy

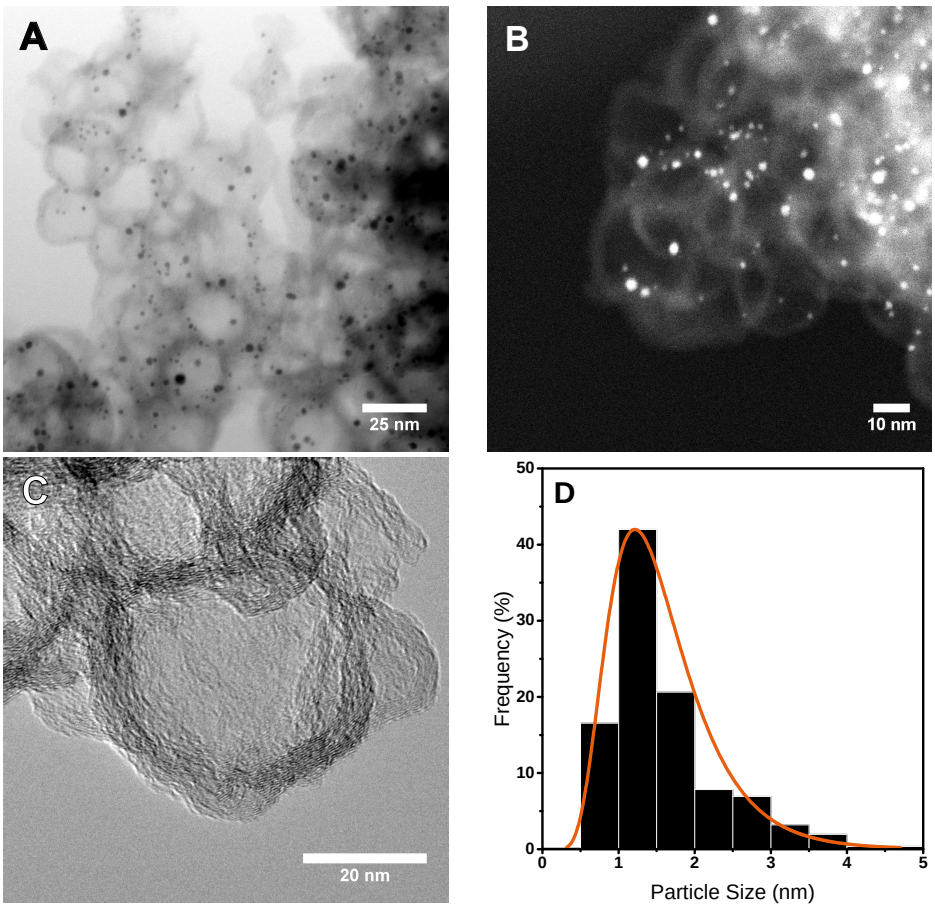

Figure 6.3.: *Representative STEM (A), HAADF-STEM (B), and TEM (C) images of Pt/NCS. (D) Size distribution based on measurements of approximately 550 nanoparticles by STEM.*

Pt/NCS was examined with STEM, HAADF-STEM, and TEM. This was done in order to gain a clearer understanding of the nanostructure of the support, as well as the platinum particles. From Figure 6.3A it is clear, that the synthesis of the NCS

was successful. The N-doped carbon spheres are well defined, and no residual SiO_2 was observed. The hollow NCS inner diameter was determined to be close to 20 nm, which is in good agreement with the mesopore size determined by N_2 physisorption analysis. The N-doped carbon shell was determined to be 3 nm thick on average. Through the condition of the CVD procedure, the Pt species were reduced to fine Pt nanoparticles. The average size was determined to be 1.5 nm, based upon the measurements of over 550 nanoparticles. Based on the Figure 6.3B it seems as if multiple Pt nanoparticles are present in some of the NCS. There is a possibility that this is due to the effect of the transmission mode of imaging. However, if this is not the case, there is an increased risk of particle agglomeration during operation, as each nanoparticle is not completely isolated.

The sample activated by KOH maintained its spherical structure, as can be seen in Figure 6.3C, albeit slightly deformed. It is suspected that the generated micropores fully penetrates the 3 nm thin shell, and is connected to the outer surface. The Pt nanoparticles are quite difficult to observe with conventional TEM. Small particles are present in the same space as the carbon shell, but any adequate determination is not possible. HAADF-STEM tomography could be a suitable characterization technique for determining the size and placement of the platinum nanoparticles in the sample. No evidence of particle agglomeration during the KOH activation was observed, as no large particles were present throughout the sample.

6.3.4. X-ray photoelectron spectroscopy

The Pt and N surface chemical species was investigated by X-ray photoelectron spectroscopy (XPS). When analysing XPS spectra, it is important to keep in mind that it is a surface-sensitive technique.[165] As the shell of the support is only 3 nm thick, it should not be an issue to obtain a representative overview of the chemical species of the catalyst.

Figure 6.4A shows the survey spectra of the Pt/NCS sample. The presence of C, N, O, and Pt are clearly visible. Figure 6.4B displays the N 1s spectra, which contains multiple nitrogen species identified as: pyrdinic (N-1), amine(N-2), pyrrolic/pyridone (N-3), graphitic/quarternary (N-4), and pyridine-N-oxide (N-5). The N-3 nitrogen species is the predominant species in the sample. The peak position for the nitrogen types can differ compared to litterature. This is due to the different environments of the nitrogen.[137] Using the integrated peak area ratio of the individual N 1s and C 1s peaks, corrected by the atomic sensitivity factors, the surface N/C ratio is determined to be ca.

10 at %.

Figure 6.4C displays the Pt 4f spectra, which can be deconvoluted into two pairs of doublets labeled with I, II. The most intense doublet with BE of 71.2 eV (Pt $4f_{7/2}$) and 74.5 eV (Pt $4f_{5/2}$) was attributed to metallic Pt. The peaks at around 72.2 and 75.5 eV could be assigned to Pt^{2+} species such as PtO or $Pt(OH)_2$.[166] This could indicate that the conditions during the CVD process is not enough to fully reduce the platinum. The integration of peak areas indicates that the majority of Pt species exist as metallic Pt.

6.3.5. Nitrogen physisorption

Table 6.1.: *Nitrogen physisorption of the prepared materials. NCS is the N-doped carbon spheres, and PNCS is porous N-doped carbon spheres.*

Sample	V_{micro}[a] (cm^3g^{-1})	V_{total}[b] (cm^3g^{-1})	S_{BET}[c] (m^2g^{-1})
Pt/NCS	$1.75 \cdot 10^{-2}$	0.760	282
Pt/PNCS	0.119	1.37	630

[a] Calculated by the *t*-plot method. [b] Determined from the isotherm adsorption branch at around P/P_0=0.99. [c] Calculated by the BET method.

The physisorption isotherm for Pt/NCS is displayed in Figure 6.5A. The isotherm shows very little uptake in the lower range of $p/p_0<0.05$. This indicates, that very little microporosity exist in the NCS sample. Hysteresis is clearly visible from $p/p_0<0.50$,which indicates the presence of mesopores in the sample. The type of hysteresis, type H2(b), is associated with pore blocking as the nitrogen adsorbed in the inner void of the particles, have access to the external surface only through narrow necks in the shell.[7] Pt/PNCS is the sample after being activated with KOH, after the removal of SiO_2. The nitrogen uptake of the materials in the microporous region, $p/p_0<0.05$, is greatly increased compared to the regular NCS material.

The BJH pore size distributions of the Pt/NCS and PNCS materials determined from the adsorption and desorption branches are displayed in Figure 6.5B. The pore size distribution determined from the adsorption branch is centered around 20 nm. In contrast, the pore size distribution from the desorption branch shows a narrow pore size distribution predominantly centered at 4.2 nm. In the same pore size distribution, it is possible to identify a second maximum centered at 3.5 nm.

From the isotherm and BJH pore size distribution, it can be concluded that the Pt/NCS

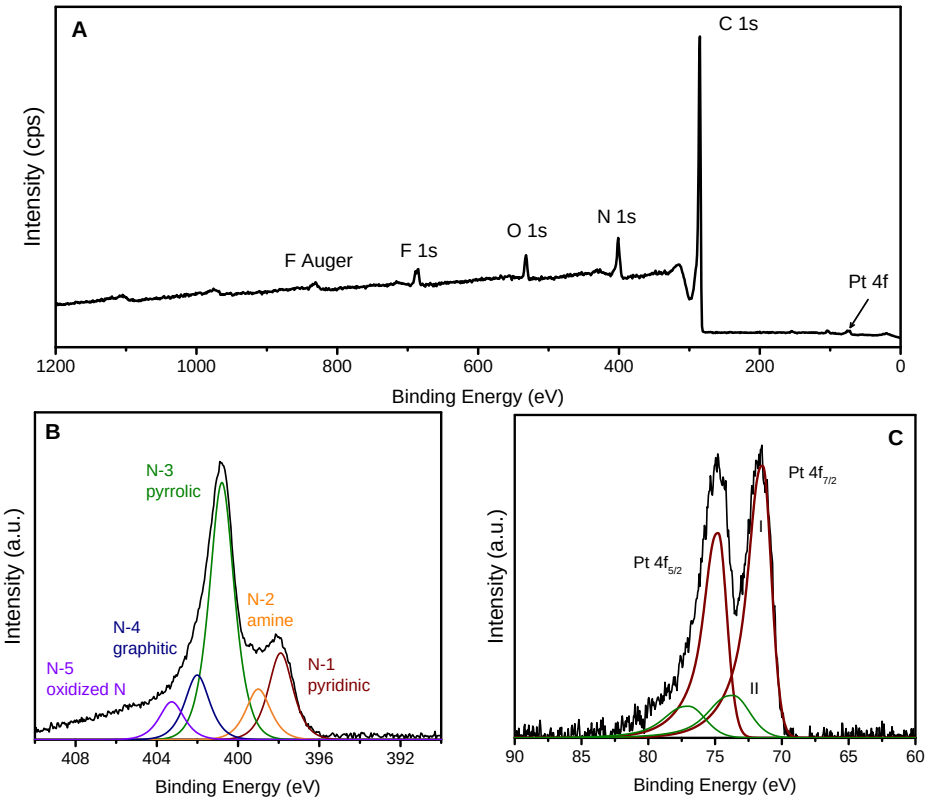

Figure 6.4.: *XPS survey (A), N 1s (B), and Pt 4f (C) spectra of the Pt/NCS material. The black lines correspond to the raw data obtained. The colored curves correspond to the deconvolutions of the fitted species. The deconvolutions are intended as a guide and do not represent any absolute assignment of the species.*

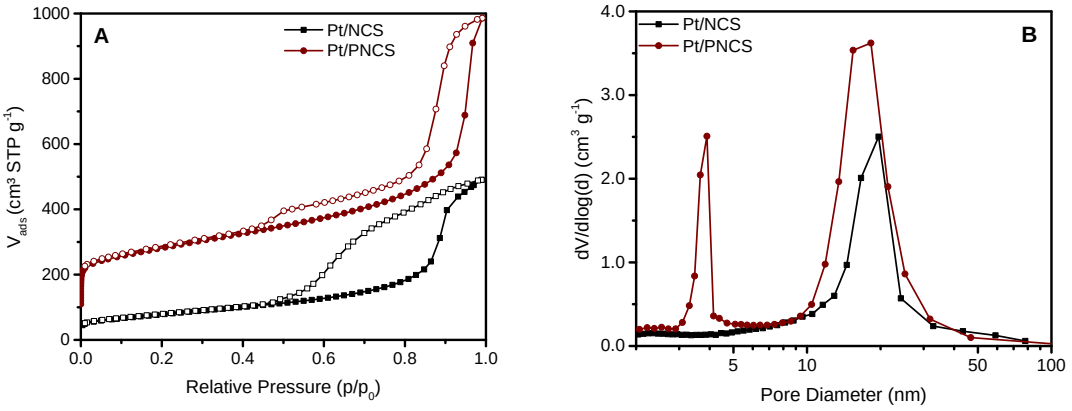

Figure 6.5.: *(A) N_2 physisorption isotherms of the prepared materials. The isotherm for Pt/PNCS is offset by 100 for illustrative purposes. (B) Barret-Joyner-Halenda derived pore size distribution from 2-100 nm.*

exhibit a low degree of porosity, besides the inner void of the spheres. The solid shell might therefore inhibit the catalytic reaction, due to diffusion limitations of reactants and products.

The data obtained from the nitrogen physisoprtion of the prepared materials are presented in Table 6.1. By activating the NCS with KOH, producing PCNS, the micro- and mesoporous volume is greatly increased. KOH activation of the sample was also attempted before removal of the silica spheres. The ambition was to remove the silica and generate pores in the shell simultaneously. If successful, this would allow one to skip the silica dissolution step with the hazardous HF. XRF results after the activation showed however residual Si present, and subsequent HF treatment was necessary.

6.3.6. Electrochemical results

Pt/NCS was tested in the catalysis toward electrochemical oxidation of MeOH, EtOH, and FA. The cyclic voltammograms are given in Figure 6.6. For the reaction with MeOH a slight peak current increase is present at 0.24 V and 0.56 V. With EtOH as a fuel, one current peak at 0.26 V and two anodic peaks at 0.60 and 1.04 V present the oxidation of EtOH and its side products. Since these two experiments did not give any strong catalytic currents, they are not analyzed further.

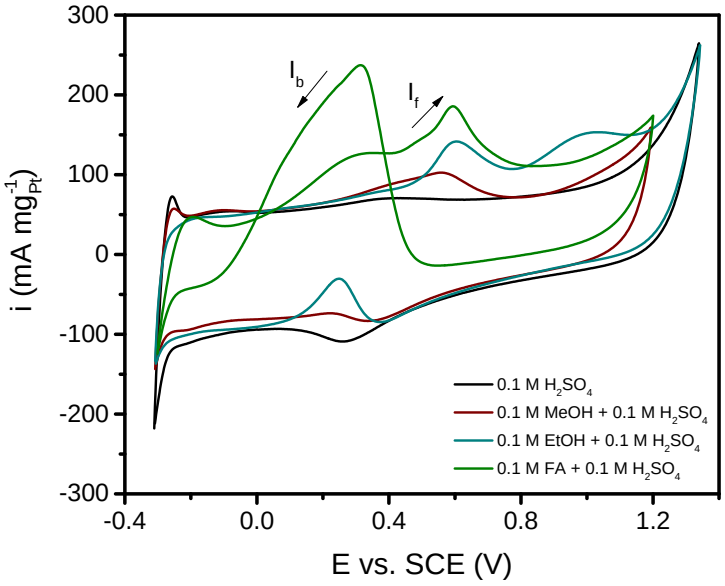

Figure 6.6.: *A) Cyclic voltammogram of Pt/NCS at 20 mV/s in 0.1 M MeOH, 0.1 M EtOH, 0.1 M FA (+ 0.1 H_2SO_4), and in pure 0.1 M H_2SO_4.*

The Pt/NCS exhibited much better activities for FA than for MeOH and EtOH. Besides the direct decomposition of FA to CO_2, oxidation can occur through dehydrogenation and adsorption of formate, or dehydration and subsequent oxidation of strongly adsorbed CO.[167] Cyclic voltammogram of electrochemical oxidation of FA display two anodic peaks at 0.30 and 0.59 V vs. SCE. These two peaks correspond to oxidation of FA through the intermediate pathways of adsorbed formate and CO respectively.

In Figure 6.7 the Pt/NCS is compared to a commercial catalyst consisting of platinum nanoparticles deposited on carbon black, Pt/C. The selectivity of the catalyst towards the direct oxidation through non-poisoning dehydrogenation of FA can be obtained through the pathway factor. This is determined by the peak ratio of the forward scan current maximum, i_f, over the backward scan current maximum, i_b. Pt/NCS pathway factor is 1.29, which is significantly lower than for the commercial Pt/C at 2.33. It is believed that this is due to the local environment near the Pt is saturated with intermediate products that only slowly diffuses out of the carbon shell. This is what inhibits the pathway factor in comparison to Pt/C. Here, Pt nanoparticles are much more accessible from the solution, making the diffusion more effective. A local saturation of side products is observed from the peak at 0.59 V. The Pt/NCS exhibit 25% higher catalytic current than the Pt/C. This originates from the increased concentration of non-diffused intermediate products being oxidized on Pt nanoparticle surface. The mass activities from the peak currents at 0.30 V were determined 237.9 mA $mgPt^{-1}$ for Pt/NCS and 352.2 mA $mgPt^{-1}$ for Pt/C. Even with the encapsulated structure of Pt nanoparticles, Pt/NCS shows only 32% lower catalytic currents than Pt/C for FA oxidation at 0.30 V peak position. So while the activity results currently are not very uplifting, the material shows promise if further optimization is possible.

The reason in much higher catalytic currents for FA than for MeOH and EtOH on Pt/NCS resides in the mechanism of the reaction, where FA is more facile to be oxidized to CO_2 and has less intermediate products than both of the alcohols. Side product diffusion plays a significant role in electrooxidation on Pt/NCS, therefore the highest activity is for FA.

The results of the fuel cell measurements performed here, is influenced by the mass transport of the reactants and products. If an in depth examination of the catalyst stability is wanted, rotating disk electrode experiments are more suitable.[113] This could give a more detailed picture of the positive effects of e.g. the N-doping and graphitization.

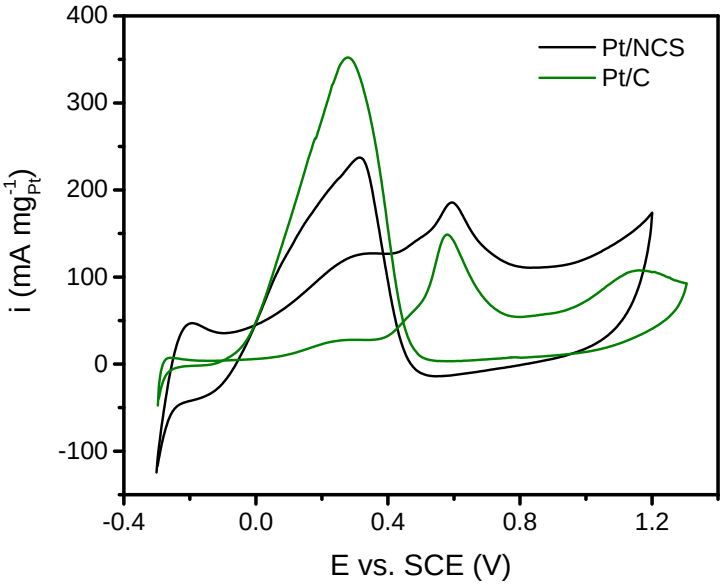

Figure 6.7.: *Electrochemical oxidation of 0.1 M formic acid at Pt/NCS and C-Pt20%, both performed at 20 mV/s on GCE in 0.1 M H_2SO_4.*

6.4. Summary

Platinum nanoparticles were successfully encapsulated in hollow nitrogen doped carbon spheres, which contained some graphitic elements. All these modifications have been reported to either increase the catalytic activity, or to improve the stability of the catalyst. The samples were characterized with respect to both the Pt nanoparticles and the nitrogen doped carbon shell. The characterization showed the successful preparation of graphitic elements through XRPD, the incorporation of nitrogen species in the carbon by XPS, and TEM and physisorption proved the hollow nature of the carbon particles. Electrochemical results show that Pt/NCS is greatly hindered by the low porosity of the shell, in the electrooxidation of formic acid. This causes a build up of intermediates in the environment surrounding the Pt nanoparticles, and reduces the activity. As a response to this, the sample was activated with KOH. This creates additionally micropores in the carbon shell, which will increase the diffusion of reactants and intermediates. If the material is to be a successful fuel cell catalyst, further improvements must be made, as well as characterization regarding the stability of the catalyst.

Chapter 7.

Conclusion

The synthesis of nanostructured solid materials holds great potential in the development of novel catalytic applications and improving existing catalytic processes. This thesis has focused on the improvement of materials for solid acid catalysts and catalysts for fuel cells.

Chapter 3 describes the material class of zeolites. An introduction is given to their structure, chemical composition, and the properties that arise from this. As the micropores in the zeolite have diameters in the size range of small molecules, they exhibit molecular size selective properties. This characteristic is one of the reason for the applications of zeolites in catalytic reactions. The micropores are however also a major drawback, as they impose mass transfer limitations that reduced the lifetime of the catalyst, among other disadvantages. The rest of the chapter is dedicated to methods on how to overcome these limitations, mainly by different synthesis procedures of mesoporous zeolites.

Chapter 4 describes a novel method of how to prepare mesoporous zeolites with a carbon secondary hard template is reported. The preparation was based on the decomposition of methane over nickel nanoparticles supported on silica. This lead to the in situ formation of carbon, which was used as a hard secondary template for the preparation of mesoporous zeolites. Compared to excisting carbon templates, made from complex methods or expensive starting materials, this in situ produced carbon template was significantly more feasible. Mesoporous HZSM-5 was succesfully prepared and matched the conventional counterpart in terms of crystallinity and acidity, while exhibiting a larger total pore volume. This resulted in an increased conversion in a model reaction, which was attributed to the improved accessibility to and from the acid sites. The method was able to create varying porosity with changes in the experimental parameters. Lastly, the method was successfully applied to ZSM-11 and Beta type zeolites.

Chapter 5 is an introduction to the proton exchange membrane fuel cell (PEMFC). The working principle of PEMFC is described, as well as possible fuels, such as hydrogen and methanol. For PEMFC to be brought closer to large scale applications, the catalyst should posses a high activity and stability. Tremendous amount of research have gone into increasing the activity by producing Pt nanoparticles or alloys. However, these modifications do not improve the resistance towards degradation of the catalyst. Common degradation mechanism are given in this chapter, as well as how to produce a carbon support that alleviate these types of degradation.

Chapter 6 reports the preparation of a fuel cell catalyst for potential sustainable electricity production. Platinum nanoparticles were successfully encapsulated in hollow nitrogen doped carbon spheres. The synthesis strategy was build upon the methods described in the previous chapter, known to withstand common degradation mechanisms. The samples were characterized with respect to both the Pt nanoparticles and the nitrogen doped carbon shell. Electrochemical results showed that the activity of the material was greatly hindered by the low porosity of the shell. Steps was taken to generate micropores in the thin carbon shell to allow for better diffusion. While initial catalytic testing showed some drawbacks, the sample displayed great promise and further optimization could be interesting.

Appendix A.

Publications

Project related publications, enclosed in this thesis:

1 J. O. Abildstrø, M. Kegnæs, G. Hytoft, J. J. Mielby, S. Kegnæs, "Synthesis of mesoporous zeolite catalysts by in situ formation of carbon template over nickel nanoparticles", *Micropor. Mesopor. Mat.*, **2016**, *225*, 232-237.

2 J. O. Abildstrøm, Z. N. Ali, U. V. Mentzel, J. J. Mielby, S. Kegnæs, M. Kegnæs, "Mesoporous MEL, BEA, and FAU zeolite crystals obtained by *in situ* formation of carbon template over metal nanoparticles", *New J. Chem.*, **2016**, *40*, 4223-4227.

Other publications

4 J. Mielby, J. O. Abildstrøm, F. Wang, T. Kasama, C. Weidenthaler and S. Kegnæs, "Oxidation of Bioethanol using zeolite encapsulated gold nanoparticles", *Angew. Chem. Int. Edit.*, **2014**, *53*, 12513-12516.

5 J. Mielby, J. O. Abildstrøm, S. Pérez-Ferreras, S. B. Rasmussen, S. Kegnæs, "Formation of pyridine *N*-oxides using mesoporous titanium silicalite-1", *J. Porous Mater*, **2014**, *21*, 531-537.

Patents

6 S. Kegnæs, J. O. Abildstrøm, J. J. Mielby, A. Gallas-Hulin, "Method of producing zeolite encapsulated nanoparticles", **2015**, Patent No.: WO2015001122.

7 S. Kegnæs, J. O. Abildstrøm, J. J. Mielby, "Method for producing zeolites and zeotypes", **2015**, Patent No.: WO2015001123.

8 S. Kegnæs, J. J. Mielby, J. O. Abildstrøm, "A general method to incorporate metal nanoparticles in zeolites and zeotypes", **2015**, Patent No.: WO2015155216.

Synthesis of mesoporous zeolite catalysts by in situ formation of carbon template over nickel nanoparticles

Synthesis of mesoporous zeolite catalysts by in situ formation of carbon template over nickel nanoparticles

J. O. Abildstrø, M. Kegnæs, G. Hytoft, J. J. Mielby, S. Kegnæs *Micropor. Mesopor. Mat.*, **2016**, *225*, 232-237.

Microporous and Mesoporous Materials 225 (2016) 232–237

Contents lists available at ScienceDirect

Microporous and Mesoporous Materials

journal homepage: www.elsevier.com/locate/micromeso

Synthesis of mesoporous zeolite catalysts by *in situ* formation of carbon template over nickel nanoparticles

Jacob Oskar Abildstrøm [a], Marina Kegnæs [b], Glen Hytoft [b], Jerrik Mielby [a], Søren Kegnæs [a, *]

[a] Department of Chemistry, Technical University of Denmark, DK-2800 Kgs. Lyngby, Denmark
[b] Haldor Topsøe A/S, Haldor Topsøes Allé 1, DK-2800 Kgs. Lyngby, Denmark

ARTICLE INFO

Article history:
Received 9 July 2015
Received in revised form
29 November 2015
Accepted 3 December 2015
Available online 17 December 2015

Keywords:
Hierarchical zeolites
Carbon templating
Metal nanoparticles
Cracking
Isomerization

ABSTRACT

A novel synthesis procedure for the preparation of the hierarchical zeolite materials with MFI structure based on the carbon templating method with *in situ* generated carbon template is presented in this study. Through chemical vapour deposition of coke on nickel nanoparticles supported on silica oxide, a carbon-silica composite is obtained and exploited as a combined carbon template/silica source for zeolite synthesis. This approach has several advantages in comparison with conventional carbon templating methods, where relatively complicated preparative strategies involving multistep impregnation procedures and rather expensive chemicals are used. Removal of the carbon template by combustion results in zeolite single crystals with intracrystalline pore volumes between 0.28 and 0.48 cm^3/g. The prepared zeolites are characterized by XRD, SEM, TEM and physisorption analysis. The isomerization and cracking of *n*-octane is chosen as a model test reaction and the mesoporous zeolite catalyst is found to exhibit higher activity than the conventional catalyst.

1. Introduction

Zeolites represent the most important group of industrial catalysts offering a wide range of applications from oil refining, petrochemistry and the synthesis of fine chemicals to environmental catalysis [1–4]. Zeolites are crystalline microporous materials that possess a well-defined structure with pore sizes in the range of molecular dimensions as well as strong acid sites. This makes zeolites unique catalysts that can provide excellent size– and shape-selectivity. Moreover, their tuneable chemical composition, high surface area and large pore volume along with high thermal, hydrothermal and mechanical stability make zeolites very attractive heterogeneous catalysts [5,6] and support materials that can incorporate metal nanoparticles or nanoclusters inside the micropore cavities [7–9]. Furthermore, zeolites modified with metal nanoparticles may combine the attractive properties of zeolites with the special catalytic properties of metal nanoparticles to give novel bifunctional catalytic materials where synergistic effects are exploited [10–12].

Unfortunately, zeolites often suffer from severe diffusion limitations that in some cases may induce a negative impact on the catalytic performance of zeolite catalysts. This is related to the intracrystalline transport of the reactants and products to and from the active sites in the zeolites, especially in the reactions that involve large and bulky compounds. Additionally, in some reactions, coke formation enhances these limitations, as the coke deposits block the zeolite micropores, causing a rapid decrease in the catalytic activity [13,14]. Therefore, large efforts have been made in order to improve the catalyst performance. This has been realized by reduction of the intracrystalline diffusion path length in the following possible approaches: synthesis of zeolites with extra-large pores [15–20], direct synthesis of zeolite nanocrystals [21–27], by exfoliating layered zeolites [28,29], and by introducing mesopores in the microporous materials through templating strategies [14,30,31] or demetallation processes [4,32–36].

Over the last years hard-templating strategies for the preparation of hierarchical zeolites and particularly the carbon templating method for the preparation of mesoporous materials have attracted considerable attention [14,30,37,38]. The creation of mesoporosity is beneficial for catalytic applications as it facilitates efficient mass transport of reactants and products in the mesopores [33]. Additionally, mesoporosity in zeolites leads to a better dispersion of

* Corresponding author.
E-mail address: skk@kemi.dtu.dk (S. Kegnæs).

http://dx.doi.org/10.1016/j.micromeso.2015.12.015
1387-1811/

active metal particles to maximize the catalyst performance [12]. Recently the benefits of introducing mesopores into zeolite crystals by carbon templating have been demonstrated [39–43]. The mesoporous zeolite crystals combine the shape-selectivity, hydrothermal stability and high acidity typical for conventional zeolites with highly efficient transport of reactants and products typical for mesoporous materials. However, in spite of numerous advantages, the carbon templating method has never been implemented industrially, due to several practical challenges including versatility in terms of zeolite structure and compositions, feasibility of tailoring the hierarchical features and ease of being scaled up in a cost-effective way [30].

Here we report the recent progress on synthesis of mesoporous zeolite catalysts modified with nickel nanoparticles using a simple and versatile procedure by *in situ* formation of the carbon template. This novel approach has several advantages in comparison with existing carbon templating methods, where relatively complicated preparative strategies involving multistep impregnation procedures are used. Furthermore, the conventional carbon templating approach often relies on relatively expensive starting materials such as carbon black pearls and tetraethylorthosilicate [14]. In the presented approach a cheap and available silica source – silica gel (SiO_2) is used. Moreover, the carbon template is generated *in situ* by decomposition of methane, which results in the formation of large amounts of coke around the silica supported nickel nanoparticles. The formation of coke over metal nanoparticles is a well-known phenomenon for a range of catalytic reactions that is frequently investigated [44]. In the presented method, the formation of coke is used to serve as carbon template during the subsequent zeolite synthesis. This approach is based on the assumption that the encapsulated carbon is removed by combustion after the zeolite crystallization, thereby creating additional porosity in the zeolite crystals. In Fig. 1 a schematic overview of the presented synthesis approach is given.

By subjecting the metal nanoparticles to a varied amount of methane, the ratio of coke to silica can be tuned. In principal, this may be used to control the porosity in the mesoporous zeolites in a very simple manner. Furthermore, this synthesis method allows adjusting the acidity of the zeolites, i.e. the Si/Al ratio independently of the mesoporosity. Finally, an important advantage of this approach is the relatively versatile synthesis method that in principle allows any desired zeolite with incorporated metal nanoparticles to be prepared in mesoporous form.

In order to compare the conventional and hierarchical zeolite catalysts the cracking and isomerization of the *n*-octane is chosen as a test reaction.

2. Experimental

2.1. X-ray powder diffraction

X-ray powder diffraction patterns were recorded in transmission mode using Cu -Kα radiation from a focussing quartz monochromator and a Huber G760 Guinier camera in the 2θ interval 5–80°.

2.2. Nitrogen physisorption

Nitrogen adsorption and desorption measurements were performed at liquid nitrogen temperature on a Micromeritics ASAP 2020. The samples were outgassed in vacuum at 200 °C during 18 h prior to measurement. Total surface area was calculated according to the BET method. Micropore volumes (V_{micro}) were determined using *t*-plot method. The total sorbed volume (V_{total}), including adsorption in the micropores and mesopores and on the external surface, were calculated from the amount of nitrogen adsorbed at relative pressure $p/p_0 = 0.99$, before the onset of interparticle

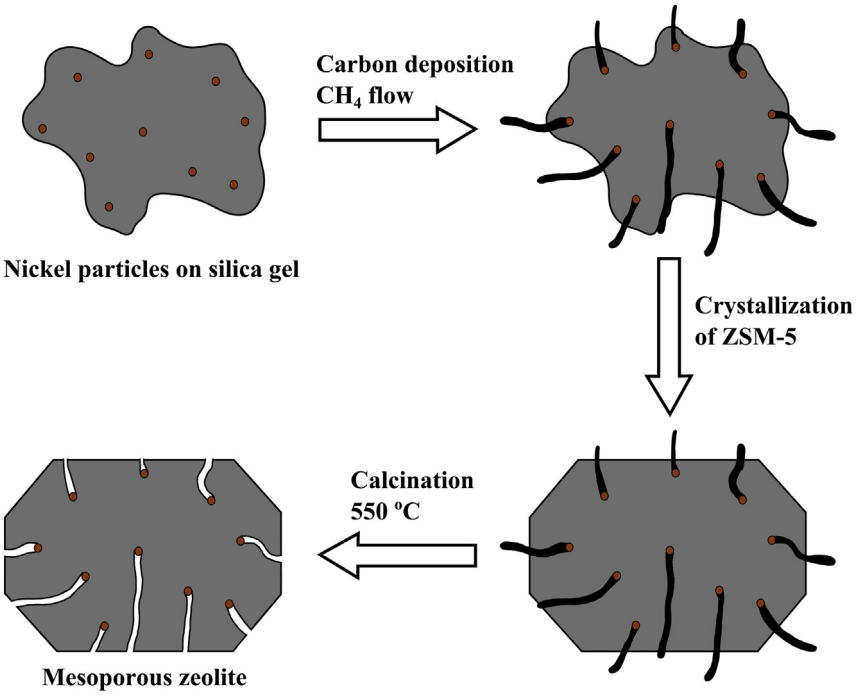

Fig. 1. Overview of the synthesis process: by passing methane over nickel nanoparticles (orange), supported on silica (grey), a carbon template is generated *in situ* as the methane decomposes to coke (black). The obtained carbon-silica composite is then transformed into zeolite during crystallization, incorporating the nickel nanoparticles and carbon. Combustion of the carbon template results in a mesoporous zeolite containing nickel nanoparticles. (For interpretation of the references to colour in this figure legend, the reader is referred to the web version of this article.)

consideration. Pore size distributions were calculated by the BJH method (desorption).

2.3. Inductively coupled plasma

Elemental analysis was performed by ion coupled plasma optical emission spectroscopy (ICP-EOS) on a Agilent 720 ES ICP-OES instrument. Before analysis the solid samples were dissolved in a solution of H_3PO_4, HCl, and HF.

2.4. Scanning electron microscopy

Scanning electron microscopy (SEM) was performed on Quanta 200 ESEM FEG operated at 10 kV, with the calcined zeolite samples placed on a carbon film and Au was evaporated onto the samples for 5 s to achieve the sufficient conductivity.

2.5. Transmission electron microscopy

Transmission electron microscopy (TEM) was performed on a FEI Tecnai microscope operated at 200 kV with the samples dispersed directly on holey carbon grids.

2.6. Materials

All reagents were of reagent grade and used without further purifications: tetrapropylammonium hydroxide (TPAOH, 1 M aqueous solution, Sigma-Aldrich), silica gel (SiO_2, Davisil Grade 62, pore size 150 Å, 60–200 mesh, Sigma-Aldrich), sodium aluminate ($NaAlO_2$, 54 wt% Al_2O_3 and 41 wt% Na_2O, Riedel-de Haen), ammonium nitrate (NH_4NO_3, 98 wt%, Aldrich), Nickel nitrate hexahydrate ($Ni(NO_3)_2 \cdot 6H_2O$, Sigma-Aldrich), *n*-octane (C_8H_{18}, 98%, Sigma-Aldrich), methane gas (CH_4, AGA), forming gas (10% H_2/N_2, AGA), and distilled water.

2.6.1. Preparation of Ni-containing silica-carbon composite materials

The silica-carbon composite was prepared by the following procedure. 0.15 g of $Ni(NO_3)_2 \cdot 6H_2O$ was dissolved in 1.73 g of water. 1.50 g of SiO_2 was impregnated with this solution to incipient wetness. The resulting material was dried overnight at room temperature and then calcined in a flow of 10% H_2/N_2 (with a ramp of 20 °C/min) at 600 °C for 4 h (Sample 1) and for 8 h (Sample 5), followed by calcination in a flow of Ar until temperature was fallen to 550 °C. One of the samples (Sample 4) was not reduced in the flow of 10% H_2/N_2. Then flow was changed to a flow of CH_4 and the obtained materials were subjected to it at 550 °C for 8 h.

2.6.2. Synthesis of Ni-containing mesoporous ZSM-5-type zeolite

The mesoporous Ni-containing Na-ZSM-5 material was prepared according to the following procedure. In a 100 ml flask, 8.73 g of TPAOH, 0.60 g of H_2O, and 0.06 g of $NaAlO_2$ was added with stirring until a clear solution was obtained. After that, the Ni-containing silica-carbon composite obtained above (2.6.1) was mixed with this solution. The composition of the resulting synthesis gel was 1 Al_2O_3: 78 SiO_2: 13TPA_2O: 1.4 Na_2O: 1313H_2O. After 1 h in case of Sample 1 and after 20 h in case of Sample 3, the final composite material was placed in a teflon beaker inside a stainless steel autoclave, containing 15 ml of water to produce saturated steam, heated to 180 °C and kept there for 72 h. Then, the autoclave was cooled to room temperature, the product was washed with deionized water (1 l) and filtered by suction. Finally, the product was dried at 90 °C for 10 h, and the organic template and the carbon was removed by controlled combustion in air in a muffle furnace at 550 °C for 24 h. Finally, the product was calcined in a flow of 10% H_2/N_2 (with a ramp of 20°/min) at 600 °C for 4 h.

2.6.3. Synthesis of Ni-containing conventional ZSM-5-type zeolite

The conventional Ni-containing Na-ZSM-5 material (Sample 2) was prepared according to the following procedure. 0.15 g of $Ni(NO_3)_2 \cdot 6H_2O$ was dissolved in 1.73 g of water. 1.50 g of SiO_2 was impregnated with this solution to incipient wetness. The resulting material was dried overnight at room temperature. In a 100 ml flask, 8.73 g of TPAOH, 0.60 g of H_2O, and 0.06 g of $NaAlO_2$ was added with stirring until a clear solution was obtained. After that, the Ni-containing silica oxide was mixed with this solution. The composition of the resulting synthesis gel was 1 Al_2O_3: 78 SiO_2: 13TPA_2O: 1.4 Na_2O: 1313H_2O. After 1 h, the final composite material was placed in a teflon beaker inside a stainless steel autoclave, containing 15 ml of water to produce saturated steam, heated to 180 °C and kept there for 72 h. Then, the autoclave was cooled to room temperature, the product was washed with deionized water (1 l) and filtered by suction. The zeolite was dried at 90 °C for 10 h, and the organic template and the carbon was removed by controlled combustion in air in a muffle furnace at 550 °C for 24 h. Finally, the product was calcined in a flow of 10% H_2/N_2 (with a ramp of 20 °C/min) at 600 °C for 4 h.

2.7. Catalysts preparation

2.7.1. Ion exchange

All acidic zeolite samples (Ni-H-ZSM-5) were prepared by the following ion-exchange procedure. The H-form of each zeolite was prepared by three consecutive ion-exchanges, starting with the corresponding Na-form (1 g of sample) and 1 M aqueous NH_4NO_3 solution (80 ml) at 80 °C. The filtered NH_4-form of zeolite was washed with deionized water (1 l) after each exchange and allowed to dry in air. Finally, the ion-exchanged product was heated in air at 550 °C for 5 h to produce the desired H-form of the zeolite.

2.8. Catalytic experiments: cracking and isomerization of n-octane

In the *n*-octane conversion experiments, 100 mg of fractionated catalyst (180–355 μm) was placed into a 3 mm stainless steel fixed-bed reactor. Afterwards, *n*-octane was pumped into an evaporator at 180 °C together with H_2 (50 ml/min) and the preheated gas was then passed through the reactor. All activity measurements were performed under the same reaction conditions using a pre-programmed temperature profile from 300 to 500 °C increasing with 1 °C/min.

The product gas was periodically analysed every 20 min by an online GC-FID equipped with a standard nonpolar column. All major products were identified from gas samples by GC-MS and by the retention time of authentic samples on the online GC-FID.

3. Results and discussion

X-ray powder diffraction patterns for all produced MFI-type zeolites after the zeolite synthesis and subsequent combustion of the organic template and the carbon material are shown in Fig. 2. Based on these data, all obtained zeolites are concluded to be completely crystalline and contain exclusively MFI-structured material.

Fig. 3(A) shows the nitrogen adsorption/desorption isotherm of Ni-containing mesoporous zeolite after combustion of the carbon. The isotherm contains a hysteresis loop at relative pressure higher than $p/p_0 = 0.4$, which is indicative for mesoporosity. Moreover, the hysteresis loop has an upward curvature at relative pressure above 0.8. This upward curvature indicates the presence of cylindrical

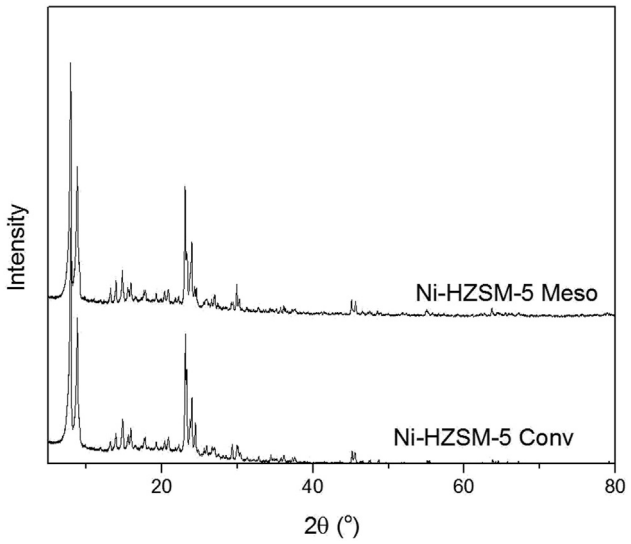

Fig. 2. XPRD patterns of pure and Ni-containing conventional (sample 2) and mesoporous (sample 1) MFI-type materials.

mesopores which are connected to the external surface area [45]. Additionally, as it is seen from Fig. 3(B) mesopores with a diameter of about 17 nm are formed. By varying process parameters as described in 2.6.1 and in 2.6.2, the zeolite samples with different amount of mesoporosity and with pore volumes of up to 0.48 cm^3/g can be formed, as it is seen in Fig. 3(C) and Tables 1 and 2. Nitrogen physisorption isotherms for these materials as well as XRPD patterns are presented in Supplementary materials.

It is apparent from Fig. 3(B) and Table 1 that mesoporous Ni-containing zeolite sample obtained by novel method using *in situ* generated carbon template has standard pores volumes and is characterized by large surface area [46]. Moreover, it is seen from Table 1 that by using the presented synthesis method it is possible easily to obtain mesoporous zeolite crystals with desirable acidity (matching the acidity of conventional materials), which is challenging in the case of conventional carbon templating method [46]. Temperature programmed desorption of ammonia (NH_3-TPD) for two samples presented in Table 1 showed very similar results, see Fig. S5 in Supplementary materials.

Fig. 4 shows representative SEM images of the conventional and mesoporous Ni-ZSM-5 zeolites after combustion of the carbon template. The SEM images indicate that both samples are highly crystalline and that crystals of uniform size are obtained. The average crystal size of both conventional and mesoporous zeolites determined from SEM images in Fig. 4 and from TEM image in Fig. 5

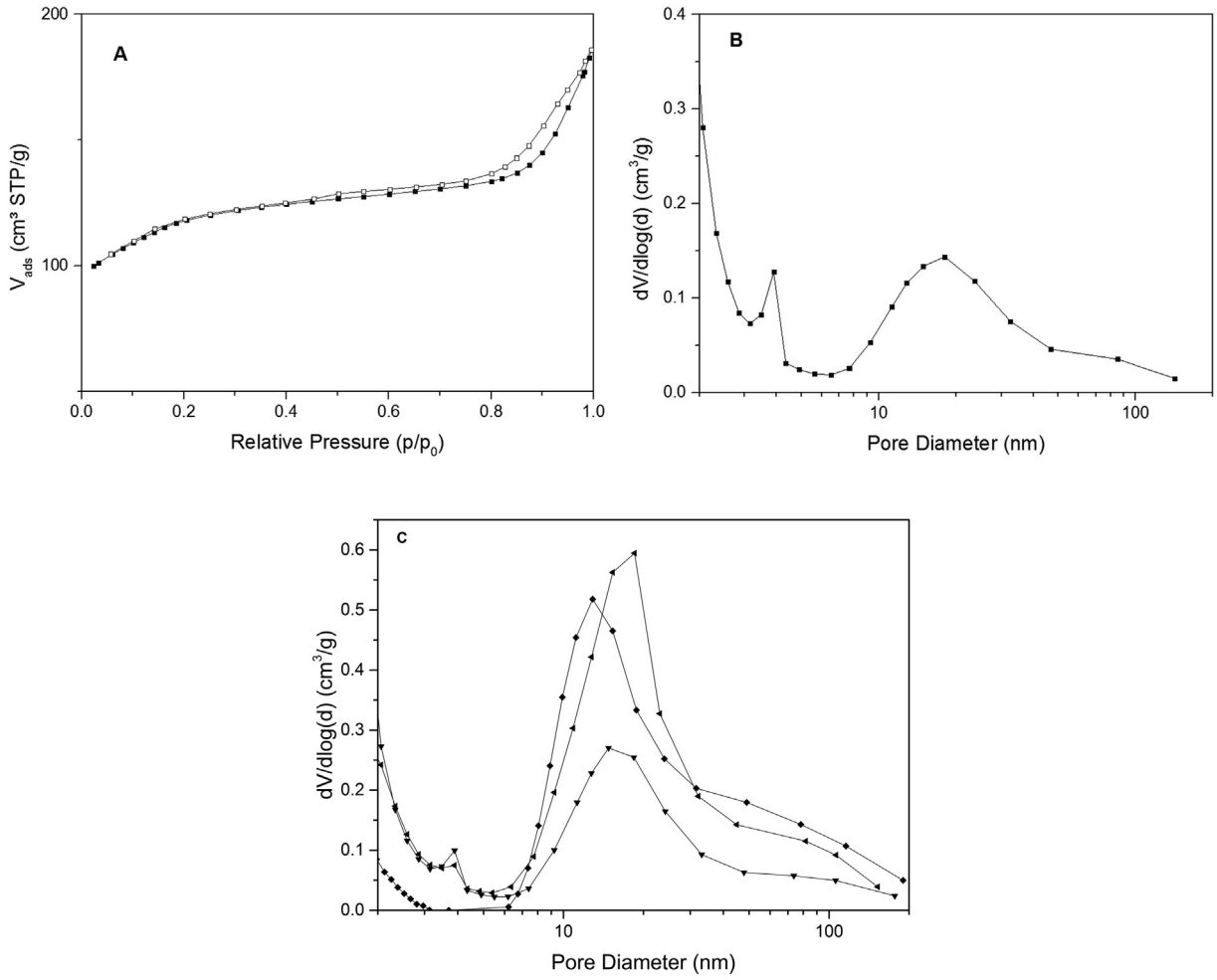

Fig. 3. (A) N_2 adsorption/desorption isotherm of the mesoporous Ni-containing HZSM-5-type material and (B) BJH-derived pore-size distribution of sample 1. (C) BJH-derived pore-size distribution of sample 3 (▼), sample 4 (◄) and sample 5 (◆).

Table 1
Nitrogen physisorption and elemental analysis data.

Sample name	Zeolite	Conv/Meso	Si/Al ratio[a]	V_{micro} (cm^3/g)[b]	V_{total} (cm^3/g)	Surface area (m^2/g)[c]	Ni content (wt%)[a]
Sample 1	Ni-HZSM-5	meso	39	0.09	0.28	429	1.9
Sample 2	Ni-HZSM-5	conv	42	0.10	0.20	388	1.7

[a] Determined by ICP.
[b] Calculated by *t*-plot method.
[c] Calculated by BET method.

Table 2
Nitrogen physisorption data for samples presented in Fig. 3(C).

Sample name	Zeolite	Conv/Meso	V_{micro} (cm^3/g)[a]	V_{total} (cm^3/g)	Surface area (m^2/g)[b]
Sample 3	Ni-HZSM-5	meso	0.12	0.46	432
Sample 4	Ni-HZSM-5	meso	0.11	0.48	448
Sample 5	Ni-HZSM-5	meso	0.13	0.40	433

[a] Calculated by *t*-plot method.
[b] Calculated by BET method.

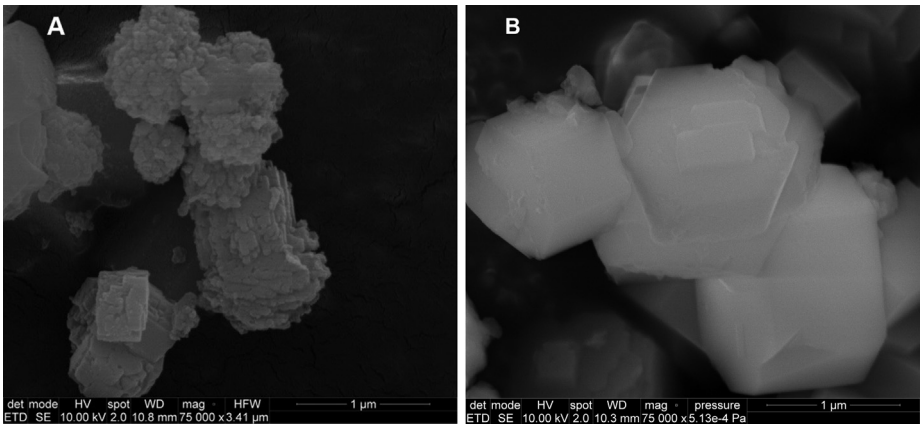

Fig. 4. SEM images of (A) mesoporous Ni-containing HZSM-5 (sample 1) and (B) microporous Ni-containing HZSM-5-type materials (sample 2).

and is about 1 µm and the typical shape of MFI-type crystals is observed.

From TEM image in Fig. 5(A), it is possible to see the individual mesopores, which are in good agreement with the pore size distribution determined by physisorption analysis. The incorporated nickel particles have an average particle size of around 6 nm as determined by TEM (Fig. 5(B)).

The TEM images of conventional ZSM-5 material are available in Supplementary materials.

As a test reaction for conventional and mesoporous Ni-HZSM-5 the cracking and isomerization of the long chain alkane *n*-octane is chosen. Fig. 6 shows the catalyst performance in terms of conversion of *n*-octane. Clearly, there is a pronounced effect of the presence of mesopores in the catalyst, which can be attributed to the

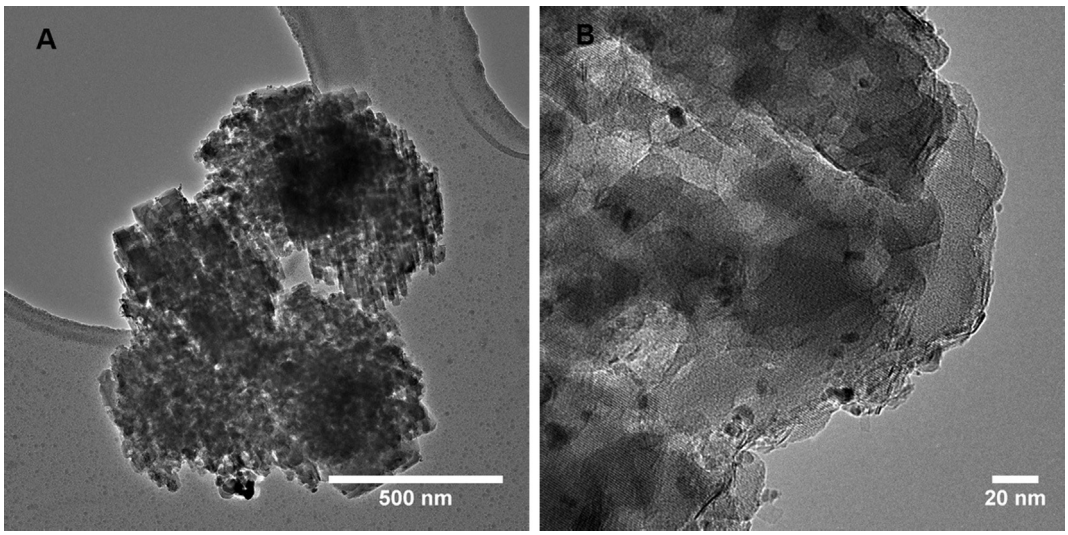

Fig. 5. TEM images of mesoporous Ni-containing HZSM-5-type material (sample 1).

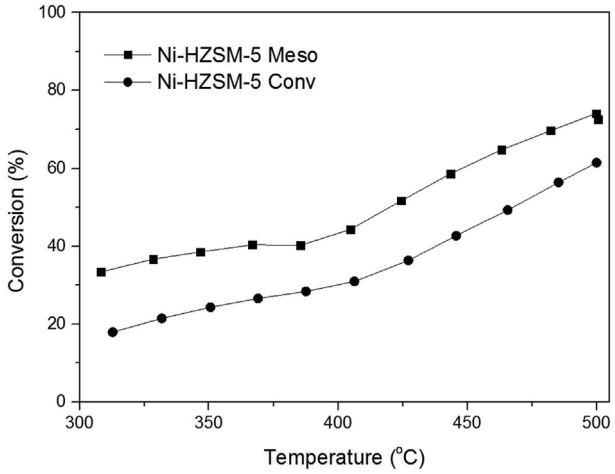

Fig. 6. Conversion of n-octane over mesoporous Ni-containing HZSM-5 (sample 1) and conventional Ni-containing HZSM-5-type materials (sample 2).

enhanced diffusion properties of the zeolite crystal compared to the conventional zeolite catalysts. This is particularly important for reactions that involve reactants more bulky than *n*-octane. The product distributions at 450 °C for the conventional and mesoporous Ni-HZSM-5 catalysts are given in Supplementary materials, Figs. S6 and S7. It is seen that the product distributions for two catalysts are similar. The mesoporous zeolite catalyst gave smaller fraction of C2 and a slightly larger faction of C5 and C6 in the product mixture in comparison with the conventional zeolite catalyst. Improved catalytic selectivity for mesoporous zeolite catalysts has also been observed previously [40].

4. Conclusions

In conclusion, the preparation of mesoporous ZSM-5-type zeolite single crystals modified with Ni-nanoparticles based on the carbon templating method with *in situ* generated carbon template is reported for the first time. The obtained zeolite material combines high crystallinity with an intracrystalline mesopore system with pore volume of up to 0.4 cm^3/g. Compared to existing carbon templating procedures, this method does not rely on the availability of special and expensive chemicals, only on the mesoporous silicas that are used widely and can be obtained easily by precipitation. Thus, with this novel and simple preparation method, it will be possible that mesoporous zeolites with incorporated nickel nanoparticles could be so easily and inexpensively available that they will find use in industrial applications.

Acknowledgements

The authors thank Mette Nielsen (Haldor Topsøe A/S) for assistance during catalyst characterization. The authors gratefully acknowledge the support of the Danish Council for Independent Research, Grant No. 2-127580 and the support of the Lundbeck Foundation (Lundbeckfonden), Grant No. R141-2013-13244.

Appendix A. Supplementary material

Supplementary material related to this article can be found at http://dx.doi.org/10.1016/j.micromeso.2015.12.015.

References

[1] W. Vermeiren, J.-P. Gilson, Top. Catal. 52 (2009) 1131–1161.
[2] C. Martínez, A. Corma, Coord. Chem. Rev. 255 (2011) 1558–1580.
[3] J. Cejka, G. Centi, J. Perez-Pariente, W.J. Roth, Catal. Today 179 (2012) 2–15.
[4] V. Valtchev, G. Majano, S. Mintova, J. Pérez-Ramírez, Chem. Soc. Rev. 42 (2013) 263–290.
[5] R. Szostak, Molecular Sieves – Principles of Synthesis and Identification, Van Nostrand Reinhold: New York, 1989, second ed., Blackie, London, 1998, pp. 1–5.
[6] A. Corma, Chem. Rev. 95 (1995) 559–614.
[7] J.C. Fierro-Gonzalez, Y. Hao, B.C. Gates, J. Phys. Chem. C 111 (2007) 6645–6651.
[8] A.B. Laursen, K.T. Højholt, L.F. Lundegaard, S.B. Simonsen, S. Helveg, F. Schüth, M. Paul, J.-D. Grunwaldt, S. Kegnæs, C.H. Christensen, K. Egeblad, Angew. Chem. Int. Ed. 49 (2010) 3504–3507.
[9] K.T. Højholt, A.B. Laursen, S. Kegnæs, C.H. Christensen, Top. Catal. 54 (2011) 1026–1033.
[10] C.H. Christensen, B. Jørgensen, J. Rass-Hansen, K. Egeblad, R. Madsen, S.K. Klitgaard, S.M. Hansen, M.R. Hansen, H.C. Andersen, A. Riisager, Angew. Chem. Int. Ed. 45 (28) (2006) 4648–4651.
[11] P.M. Arnal, M. Comotti, F. Schüth, Angew. Chem. 118 (2006) 8404–8407.
[12] J. Mielby, J.O. Abildstrøm, F. Wang, T. Kasama, C. Weidenthaler, S. Kegnæs, Angew. Chem. Int. Ed. 53 (2014) 12513–12516.
[13] C.H. Christensen, K. Johannsen, E. Törnqvist, I. Schmidt, H. Topsøe, C.H. Christensen, Catal. Today 128 (2007) 117–122.
[14] K. Egeblad, C.H. Christensen, M. Kustova, C.H. Christensen, Chem. Mater 20 (2008) 946–960.
[15] M.E. Davis, C. Saldarriaga, C. Montes, J. Garces, C. Crowder, Nature 331 (1988) 698–699.
[16] C.C. Freyhardt, M. Tsapatsis, R.F. Lobo, K.J. Balkus Jr., M.E. Davis, Nature 381 (1996) 295–298.
[17] A. Corma, M.J. Diaz-Cabanas, J.L. Jorda, C. Martinez, M. Moliner, Nature 443 (2006) 842–845.
[18] J. Sun, C. Bonneau, A. Cantin, A. Corma, M.J. Diaz-Cabanas, M. Moliner, D. Zhang, M. Li, X. Zou, Nature 458 (2009) 1154–1158.
[19] R. Simancas, D. Dari, N. Velamazán, M.T. Navarro, A. Cantín, J.L. Jordá, G. Sastre, A. Corma, F. Rey, Science 26 (2010) 1219–1222.
[20] O.V. Shvets, P. Nachtigall, W.J. Roth, J. Cejka, Microporous Mesoporous Mater. 182 (2013) 229–238.
[21] G. Bellussi, A. Carati, M.G. Clerici, G. Meddinelli, R. Millini, J. Catal. 133 (1992) 220–230.
[22] L. Tosheva, V. Valtchev, Chem. Mater. 17 (2005) 2494–2513.
[23] M. Choi, K. Na, J. Kim, Y. Sakamoto, O. Terasaki, R. Ryoo, Nature 461 (2009) 246–249.
[24] M. Tsapatsis, W. Fan, Chem. Cat. Chem. 2 (2010) 246–248.
[25] X. Zhang, D. Liu, D. Xu, S. Asahina, K.A. Cychosz, K.V. Agrawal, Y.A. Wahedi, A. Bhan, S.A. Hashimi, O. Terasaki, M. Thommes, M. Tsapatsis, Science 336 (2012) 1684–1687.
[26] W. Chaikittisilp, Y. Suzuki, R.R. Mukti, T. Suzuki, K. Sugita, K. Itabashi, A. Shimojima, T. Okubo, Angew. Chem. 125 (2013) 3439–3443.
[27] H. Awala, J.-P. Gilson, R. Retoux, P. Boullay, J.-M. Goupil, V. Valtchev, S. Mintova, Nat. Mater. 14 (2015) 447–451.
[28] A. Corma, V. Fornes, S.B. Pergher, Th.L.M. Maesen, J.G. Buglass, Nature 396 (1998) 353–356.
[29] S. Maheshwari, E. Jordan, S. Kumar, F.S. Bates, R.L. Penn, D.F. Shantz, M. Tsapatsis, J. Am. Chem. Soc. 130 (2008) 1507–1516.
[30] D.P. Serrano, J.M. Escola, P. Pizarro, Chem. Soc. Rev. 42 (2013) 4004–4035.
[31] K. Na, G.A. Somorjai, Catal. Lett. 145 (2015) 193–213.
[32] J. Perez-Ramirez, D. Verboekend, A. Bonilla, S. Abello, Adv. Funct. Mater. 19 (2009) 3972–3979.
[33] R. Chal, C. Gerardin, M. Bulut, S. van Donk, Chem. Cat. Chem. 3 (2011) 67–81.
[34] K. Na, M. Choi, R. Ryoo, Microporous Mesoporous Mater. 166 (2013) 3–19.
[35] M.S. Holm, K. Egeblad, P.N.R. Vennestrøm, C.G. Hartmann, M. Kustova, C.H. Christensen, Eur. J. Inorg. Chem. (2008) 5185–5189.
[36] P.N.R. Vennestrøm, M. Grill, M. Kustova, K. Egeblad, L.F. Lundegaard, F. Joensen, C.H. Christensen, P. Beato, Catal. Today 168 (2011) 71–79.
[37] C.J.H. Jacobsen, C. Madsen, J. Houzvicka, I. Schmidt, A. Carlsson, J. Am. Chem. Soc. 122 (2000) 7116–7117.
[38] M. Kustova, K. Egeblad, K. Zhu, C.H. Christensen, Chem. Mater. 19 (2007) 2915–2917.
[39] M.Yu Kustova, P. Hasselriis, C.H. Christensen, Catal. Lett. 96 (2004) 205–211.
[40] C.H. Christensen, I. Schmidt, C.H. Christensen, Catal. Commun. 5 (2004) 543–546.
[41] M. Yu Kustova, S.B. Rasmussen, A.L. Kustov, C.H. Christensen, Appl. Catal. B 67 (2006) 60–67.
[42] M. Kustova, M.S. Holm, C.H. Christensen, Y.-H. Pan, P. Beato, T.V.W. Janssens, F. Joensen, J. Nerlov, Stud. Surf. Sci. Catal. 174 (2008) 117–122.
[43] M.S. Holm, E. Taarning, K. Egeblad, C.H. Christensen, Catal. Today 168 (2011) 3–16.
[44] A.K. Rovik, S.K. Klitgaard, S. Dahl, C.H. Christensen, I. Chorkendorff, Appl. Catal. A 358 (2009) 269–278.
[45] A.N. Janssen, I. Schmidt, C.J.H. Jacobsen, A.J. Koster, K.P. de Jong, Microporous Mesoporous Mater. 65 (2003) 59–75.
[46] M. Yu Kustova, A.L. Kustov, C.H. Christensen, Stud. Surf. Sci. Catal. 158 (2005) 255–262.

Mesoporous MEL, BEA, and FAU zeolite crystals obtained by *in situ* formation of carbon template over metal nanoparticles

Mesoporous MEL, BEA, and FAU zeolite crystals obtained by *in situ* formation of carbon template over metal nanoparticles

J. O. Abildstrøm, Z. N. Ali, U. V. Mentzel, J. J. Mielby, S. Kegnæs, M. Kegnæs *New J. Chem.*, **2016**, *40*, 4223-4227.

NJC

PAPER

View Article Online
View Journal | View Issue

Cite this: *New J. Chem.*, 2016, **40**, 4223

Mesoporous MEL, BEA, and FAU zeolite crystals obtained by *in situ* formation of carbon template over metal nanoparticles†

Jacob Oskar Abildstrøm,[a] Zahra Nasrudin Ali,[a] Uffe Vie Mentzel,[b] Jerrik Mielby,[a] Søren Kegnæs*[a] and Marina Kegnæs[b]

Received (in Victoria, Australia) 12th October 2015,
Accepted 5th January 2016

DOI: 10.1039/c5nj02809d

www.rsc.org/njc

Here, we report the synthesis and characterization of hierarchical zeolite materials with MEL, BEA and FAU structures. The synthesis is based on the carbon templating method with an *in situ*-generated carbon template. Through the decomposition of methane and deposition of coke over nickel nanoparticles supported on silica, a carbon–silica composite is obtained and exploited as a combined carbon template/silica source for the zeolite synthesis. The mesoporous zeolite materials were all prepared by hydrothermal crystallization in alkaline media followed by removal of the carbon template by combustion, which results in zeolite single crystals with intracrystalline pore volumes of up to 0.44 cm^3 g^{-1}. The prepared zeolite structures are characterized by XRD, SEM, TEM and N_2 physisorption measurements.

1. Introduction

Zeolites are crystalline inorganic materials with an ordered microporous structure and strong acid sites that are extensively used as heterogeneous catalysts in oil refining and chemical synthesis.[1,2] Furthermore, zeolites possess high surface areas and large pore volumes and are therefore used in many modern industrial processes related to catalysis, adsorption, and separation, where they provide excellent size- and shape-selectivity.[3,4] However, the large-scale application of zeolites has still not reached its full potential,[5] because zeolite catalysts often suffer from severe diffusion limitations. Since the reactants and products have to diffuse through the micropores in order to reach and leave the active sites, the diffusion in zeolites is often orders of magnitude slower than both molecular and Knudsen diffusion. These diffusion limitations are enhanced for large and bulky compounds that closely match the pore sizes of the zeolites and will inevitably slow down the reaction rate.

Moreover, in some reactions, coke formation enhances these limitations, as the coke deposits block the zeolite micropores, which results in a rapid decrease in catalytic activity.[6,7]

Therefore, several preparative strategies have been developed in the attempt to improve the performance of zeolites in catalysis: the synthesis of zeolites with extra-large pores,[8–11] direct synthesis of zeolite nanocrystals,[12–17] by exfoliating layered zeolites,[18,19] and by introducing mesopores in the microporous materials through templating strategies[7,20–22] or demetallation processes.[4,7,23–25]

Recently, a novel synthesis procedure for the preparation of mesoporous MFI-type material based on the carbon templating method with an *in situ*-generated carbon template was reported by our group.[26] The mesoporous zeolite crystals combine the shape-selectivity, hydrothermal stability, and high acidity typical for conventional zeolites with highly efficient transport of reactants and products typical for mesoporous materials.[7] The novel synthesis approach has several advantages in comparison with existing carbon templating methods, where relatively complicated preparative strategies involving multistep impregnation procedures are used.[27–30] In the presented approach a cheap and available silica source–silica gel (SiO_2) is used. The carbon template is generated *in situ* by decomposition of methane, which results in the formation of large amounts of coke around the silica supported nickel nanoparticles.[26] The formation of coke over metal nanoparticles is a well-known phenomenon for a range of catalytic reactions that is frequently investigated.[31] For the decomposition of methane, supported nickel nanoparticles are recognized as effective catalysts.[32] In this way, the novel synthesis approach is more cost effective in comparison with the conventional carbon templating approach that relies on relatively expensive starting materials such as carbon black pearls and tetraethyl orthosilicate.[7,27,28,30] The encapsulated carbon is removed by combustion after the zeolite crystallization, which creates mesoporosity in the zeolite crystals. In Fig. 1 a schematic overview of the presented synthesis approach is given.

[a] *Department of Chemistry, Technical University of Denmark, DK-2800 Kgs. Lyngby, Denmark. E-mail: skk@kemi.dtu.dk*
[b] *Haldor Topsøe A/S, Haldor Topsøes Allé 1, DK-2800 Kgs. Lyngby, Denmark*

† Electronic supplementary information (ESI) available: Physisorption analysis – pore size distribution and transmission electron microscopy. See DOI: 10.1039/c5nj02809d

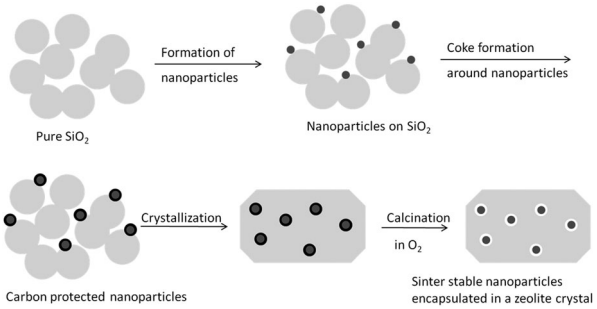

Fig. 1 Synthesis scheme for preparation of mesoporous zeolite single crystals based on the carbon templating method with an *in situ*-generated carbon template.

Furthermore, this novel synthesis method allows preparation of mesoporous zeolites with desirable acidity, which is challenging in the case of the conventional carbon templating method.[33]

Here, we report the recent progress on the synthesis and characterization of mesoporous zeolites with MEL, BEA and FAU structures using an *in situ*-generated carbon template obtained by decomposition of methane over nickel nanoparticles. The results demonstrate that our synthetic strategy is general and opens up for simple and cost-effective synthesis of several important industrial zeolite catalysts in mesoporous form.

2. Experimental

2.1 X-ray powder diffraction

X-ray powder diffraction patterns were recorded in transmission mode using Cu-Kα radiation from a focusing quartz monochromator and a Huber G760 Guinier camera in the 2θ interval 5–60°.

2.2 Nitrogen physisorption

Nitrogen adsorption and desorption measurements were performed at liquid nitrogen temperature on a Micromeritics ASAP 2020. The samples were outgassed in vacuum at 200 °C during 18 h prior to measurement. Total surface area was calculated according to the BET method. Total- and micropore volumes were determined by the BJH method (desorption branch) and *t*-plot method respectively.

2.3 Scanning electron microscopy

Scanning electron microscopy (SEM) was performed on Quanta 200 ESEM FEG operated at 10 kV, with the calcined zeolite samples placed on a carbon film and Au was evaporated onto the samples for 5 seconds to achieve the sufficient conductivity.

2.4 Transmission electron microscopy

Transmission electron microscopy (TEM) was performed on a FEI Tecnai microscope operated at 200 kV with the samples dispersed directly on holey carbon grids.

2.5 Materials

All reagents were of reagent grade and used without further purifications: tetrabutylammonium hydroxide (TBAOH, 40 wt%, Sigma-Aldrich), tetraethylammonium hydroxide (TEAOH, 35 wt%, Sigma-Aldrich), silica gel (SiO_2, Davisil Grade 62, pore size 150 Å, 60–200 mesh, Sigma-Aldrich), sodium hydroxide (NaOH, 97%, VWR), sodium aluminate ($NaAlO_2$, 54 wt% Al_2O_3 and 41 wt% Na_2O, Riedel-de Haen), aluminium nitrate ($Al(NO_3)_3{\cdot}9H_2O$, Riedel-de Haen), nickel nitrate hexahydrate ($Ni(NO_3)_2{\cdot}6H_2O$, Sigma-Aldrich), methane gas (CH_4, AGA), forming gas (10% H_2/N_2, AGA), argon gas (Ar, AGA) and distilled water.

2.6 Zeolite synthesis

2.6.1. Preparation of Ni-containing silica–carbon composite material. The silica–carbon composite was prepared by the following procedure. 0.15 g of $Ni(NO_3)_2{\cdot}6H_2O$ was dissolved in 1.73 g of water. 1.50 g of SiO_2 was impregnated with this solution to incipient wetness. The resulting material was dried overnight at room temperature and then reduced in a flow of 10% H_2/N_2 (with a ramp of 20 °C min^{-1}) at 600 °C for 4 hours, followed by calcination in a flow of Ar until temperature was fallen to 550 °C. Then the obtained materials were subjected to CH_4 flow at 550 °C for 8 hours.

2.6.2. Synthesis of Ni-containing mesoporous MEL-type zeolite. The mesoporous Ni-containing Na-ZSM-11 material was prepared according to the following procedure. In a 100 mL flask, 3.16 g of H_2O, 0.14 g of NaOH and 0.21 g of $Al(NO_3)_3{\cdot}9H_2O$ were added with stirring and mixed with the Ni-containing silica–carbon composite obtained above (Section 2.6.1). Then, 3.18 g of TBAOH was added to this mixture. The composition of the resulting synthesis gel was $1Al_2O_3{:}91SiO_2{:}9.1TBA_2O{:}6.5Na_2O{:}1055H_2O$. The final composite material was placed in a Teflon beaker inside a stainless steel autoclave, containing 15 g of water to produce saturated steam, heated to 175 °C and kept there for 24 h. Then, the autoclave was cooled to room temperature, the product was washed with deionized water (1 L) and filtered by suction. Finally, the product was dried at 90 °C for 10 h, and the organic template and the carbon were removed by controlled combustion in air in a muffle furnace at 550 °C for 24 h.

2.6.3. Synthesis of Ni-containing mesoporous BEA-type zeolite. The mesoporous Ni-containing Na-Beta material was prepared according to the following procedure. In a 100 mL flask, 0.08 g of NaOH, 1.74 g of H_2O, 0.17 g of $NaAlO_2$ and 4.25 g of TEAOH were added with stirring until a clear solution was obtained. After that, the Ni-containing silica–carbon composite obtained above (Section 2.6.1) was impregnated with this mixture. The composition of the resulting synthesis gel was $1Al_2O_3{:}28SiO_2{:}5.6TBA_2O{:}2.4Na_2O{:}278H_2O$. The final composite material was introduced into a stainless steel autoclave, containing 15 g of water to produce saturated steam, heated to 140 °C and kept there for 144 h. Then, the autoclave was cooled to room temperature, the product was washed with deionized water (1 L) and filtered by suction. The zeolite was dried at 90 °C for 10 h, and the organic template and the carbon were removed by controlled combustion in air in a muffle furnace at 550 °C for 24 h.

2.6.4. Synthesis of Ni-containing mesoporous FAU-type zeolite. The synthesis of mesoporous FAU-type crystals was based on the recipe from the patent by Christensen *et al.* Example 9.[34]

In a typical synthesis procedure, the freshly prepared chemicals were used: sodium silicate (200 g L^{-1} SiO_2), sodium aluminate solution (240 g L^{-1} Al_2O_3), sodium hydroxide solution (400 g Na_2O L^{-1}). The mesoporous NaY material was prepared using seed gel according to the following procedure. Seed gel was made by the following recipe: in 100 mL flask 9.3 mL of sodium aluminate solution (240 g L^{-1} Al_2O_3), 19.97 mL of sodium hydroxide solution (400 g L^{-1} Na_2O) and 50 mL of sodium silicate (200 g L^{-1} SiO_2) were added slowly with stirring. After that the mixture was left for 4 hours. Synthesis gel was prepared by the following procedure: in 100 mL flask 4.4 mL of sodium aluminate solution (240 g L^{-1} Al_2O_3), 2.35 mL of sodium hydroxide solution (400 g L^{-1} Na_2O) and 5.46 mL of sodium silicate (200 g L^{-1} SiO_2) were added slowly with stirring. After that, the Ni-containing silica–carbon composite obtained above (Section 2.6.1) and 0.48 mL of seed gel was added slowly. The mixture was left for 1 hour with stirring. The composition of the resulting synthesis gel was $1Al_2O_3$:$7SiO_2$:$5Na_2O$:$85H_2O$. Then the gel was introduced into a stainless steel autoclave, containing 15 g of water to produce saturated steam, heated to 100 °C and kept there for 18 h. Then, the autoclave was cooled to room temperature, the product was washed with deionized water (1 L) and filtered by suction. The zeolite was dried at 90 °C for 10 h, and the carbon template was removed by controlled combustion in air in a muffle furnace at 550 °C for 24 h.

2.6.5. Synthesis of reference conventional zeolite materials. All conventional materials MEL, BEA and FAU were synthesized the same way as the corresponding mesoporous materials using 1.5 g of pure SiO_2 instead of the Ni-containing silica–carbon composite described above (Section 2.6.1).

3. Results and discussion

All X-ray powder diffraction (XRPD) patterns were obtained after the zeolite synthesis and subsequent combustion of the organic template and/or the carbon material. XRPD patterns for the conventional- and mesoporous ZSM-11, Beta and Zeolite Y zeolites are shown in Fig. 2. Based on these data, all obtained zeolites are concluded to be highly crystalline structured materials.

In Fig. 3, the nitrogen adsorption and desorption isotherm of the conventional- and mesoporous ZSM-11, Beta and Zeolite Y materials after combustion of the organic template and/or carbon are shown. In Table 1, the BET surface areas and pore volumes of the obtained ZSM-11, Beta and Zeolite Y samples are summarized. According to the IUPAC classification of physisorption isotherms,[35] all prepared mesoporous zeolites have Type IV isotherms. The isotherms contains a hysteresis loop at relative pressures higher than $p/p_0 = 0.4$, which is indicative for mesoporosity. Moreover, the hysteresis loop has an upward curvature at relative pressures above 0.8. This upward curvature indicates the presence of cylindrical mesopores which are connected to the external surface area.[35] The pore size distribution of the prepared materials, are presented in the ESI.† It is apparent from Fig. 3 and Table 1 that mesoporous ZSM-11 and

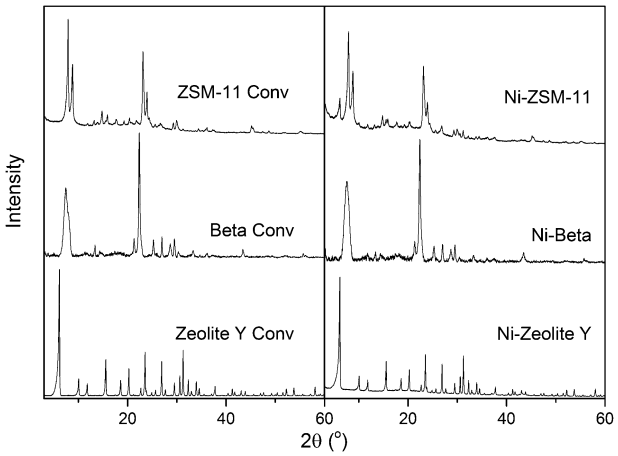

Fig. 2 XPRD patterns of conventional and mesoporous ZSM-11, Beta, and Zeolite Y-type materials.

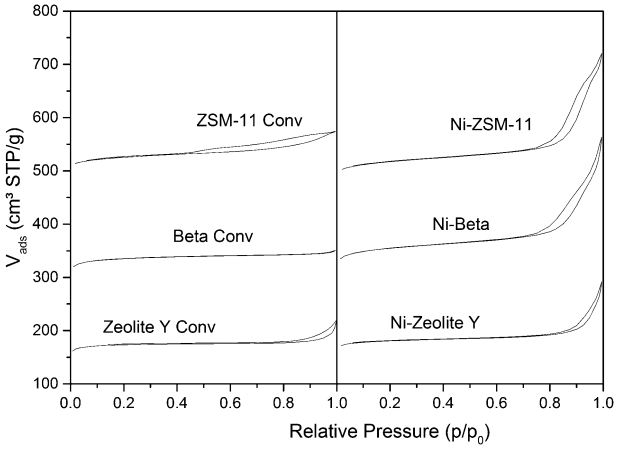

Fig. 3 Nitrogen adsorption and desorption isotherms of the conventional and mesoporous Ni-containing ZSM-11, Beta and Zeolite Y-type materials.

Table 1 Nitrogen physisorption and elemental analysis data

Zeolite	Conv/ Meso	V_{micro} [a] (cm^3 g^{-1})	V_{total} [b] (cm^3 g^{-1})	S_{BET} [c] (m^2 g^{-1})	Si/Al ratio[d]
Ni-ZSM-11	Meso	0.13	0.41	397	88
ZSM-11	Conv	0.14	0.22	409	88
Ni-Beta	Meso	0.18	0.44	522	24
Beta	Conv	0.22	0.27	553	22
Ni-Zeolite Y	Meso	0.32	0.34	853	4.4
Zeolite Y	Conv	0.33	0.35	886	4.6

[a] Calculated by *t*-plot method. [b] Calculated by BJH method. [c] Calculated by BET method. [d] Determined by ICP.

Beta zeolite samples obtained by novel method using *in situ*-generated carbon template have standard pore volumes and are characterized by large surface areas.[28,30] However, mesoporous Zeolite Y sample has a rather moderate degree of mesoporosity[34] and as it is shown in our previous work,[26] it can be improved by varying process parameters in Section 2.6.1. The different and a quite moderate degree of mesoporosity in Zeolite Y compared to ZSM-11 and Beta could be due to the much different procedure

for the preparation of the synthesis gel. As synthesized, Zeolite Y has poor thermal/hydrothermal stability due to the high content of Al and Na in the structure. Therefore, the parent Zeolite Y is subjected to a series of modifications (stabilization) such as ion exchange followed by steam calcination to impart both acidity and stability into the structure. These modifications of Zeolite Y are relatively complicated, since the framework of Zeolite Y has to be partially destroyed in order to remove large amounts of Na and Al. Therefore, the introduction of even moderate degree of mesoporosity during the synthesis could improve the ability for the ion exchange of Zeolite Y and thus lead to an improved and more stable ion exchange process on industrial scale. Moreover, it is seen from Table 1 that by using the presented synthesis method it is possible easily to obtain mesoporous zeolite crystals with desirable acidity (matching the acidity of conventional materials), which is challenging in the case of the conventional carbon templating method.[33]

Representative results of SEM for the conventional and mesoporous ZSM-11, Beta and Zeolite Y zeolites after combustion of the carbon template are shown in Fig. 4. From the SEM images it can be seen that all samples are highly crystalline and that crystals of uniform size are obtained. The average crystal size of both conventional and mesoporous zeolites determined from SEM images in Fig. 4 and are about 3 μm for ZSM-11, 1 μm for Beta and 0.5 μm for Zeolite Y.

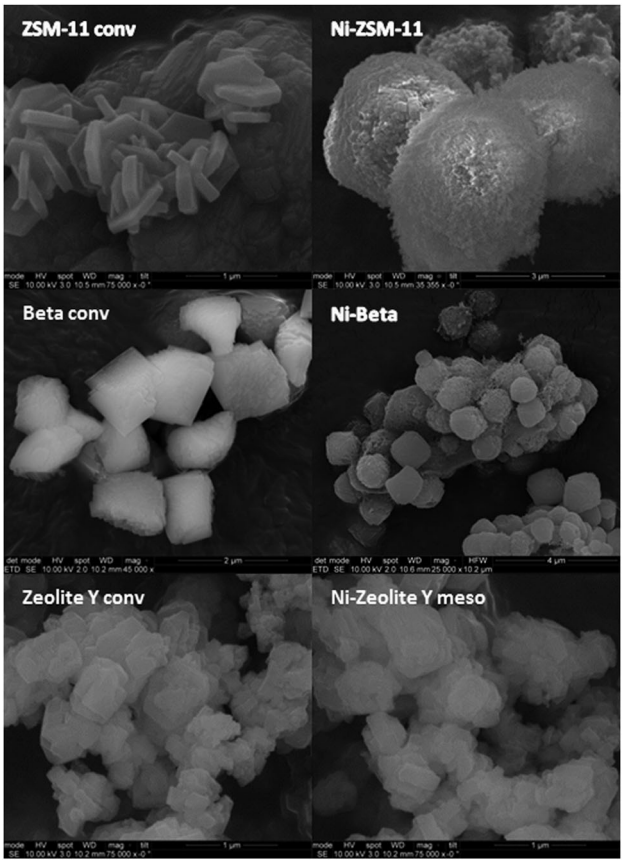

Fig. 4 SEM images of conventional and mesoporous ZSM-11, Beta and Zeolite Y-type materials.

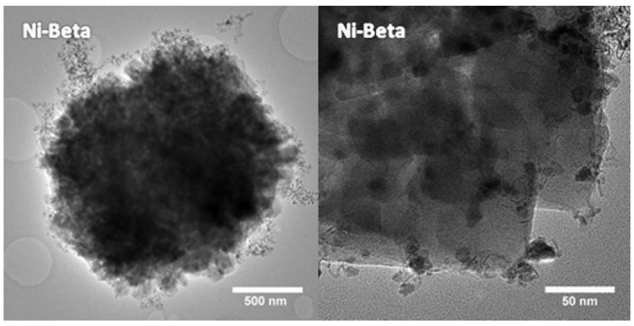

Fig. 5 TEM images of mesoporous Beta-type materials.

The major difference between the conventional and mesoporous ZSM-11 and Beta zeolite crystals, is the presence of non-crystallographic intracrystalline mesopores resulting in the high porosity. The conventional zeolite ZSM-11 has the typical coffin-shape intergrown crystals, and the conventional Beta material has the typical rounded-cube shape. From the SEM images of the mesoporous ZSM-11 and Beta zeolites, it can be seen that the crystals have shapes typical for the mesoporous single crystals. The conventional and mesoporous crystals of Zeolite Y materials look very similar due to rather moderate degree of mesoporosity in the mesoporous sample.

The results of transmission electron microscopy for the mesoporous Beta-type zeolites after combustion of the carbon are shown in Fig. 5. It is easily possible to see the mesoporous zeolite crystal, which clearly features some brighter areas distributed all over. These brighter areas are the mesopores created by removal of the carbon. The sponge-like appearance of the crystal is typical for this kind of mesoporous single crystal materials obtained by using excess of a zeolite gel as described in details by Jacobsen *et al.*[27] The nickel particles incorporated into the zeolite catalyst have an average particle size of 6 nm as it is determined from TEM images. It was shown previously,[30,36] that using the standard carbon templating synthesis procedure in alkaline media it is possible to get only nanosized Beta material. Here, we show that the use of novel synthesis procedure based on the carbon templating method with an *in situ*-generated carbon template allowed us to obtain mesoporous zeolite Beta single crystal materials. TEM images of the mesoporous Ni-ZSM-11 zeolite are presented in the ESI.†

4. Conclusions

In conclusion, the preparation of mesoporous ZSM-11, Beta and Y-type zeolite single crystals modified with Ni-nanoparticles based on the carbon templating method with an *in situ*-generated carbon template is reported for the first time. The obtained zeolite materials combine high crystallinity with an intracrystalline mesopore system with pore volume of up to 0.44 $cm^3\ g^{-1}$. Compared to existing carbon templating procedures, this method does not rely on the availability of special and expensive chemicals, only on the mesoporous silica which is used widely and can be obtained easily by precipitation. Moreover, we show that the use of novel synthesis procedure based on the

carbon templating method with an *in situ*-generated carbon template allowed us to obtain mesoporous zeolite Beta in alkaline media.

Thus, with this novel and simple preparation method, it will be possible that mesoporous zeolites with incorporated nickel nanoparticles could find use in industrial applications.

Acknowledgements

The authors gratefully acknowledge the support of the Danish Council for Independent Research, Grant No. 2-127580 and the support of the Lundbeck Foundation (Lundbeckfonden), Grant No. R141-2013-13244.

Notes and references

1 A. Corma, *Chem. Rev.*, 1995, **95**, 559.
2 C. Martínez and A. Corma, *Coord. Chem. Rev.*, 2011, **255**, 1558.
3 J. Cejka, G. Centi, J. Perez-Pariente and W. J. Roth, *Catal. Today*, 2012, **179**, 2.
4 V. Valtchev, G. Majano, S. Mintova and J. Pérez-Ramírez, *Chem. Soc. Rev.*, 2013, **42**, 263.
5 M. Hartmann, *Angew. Chem., Int. Ed.*, 2004, **43**, 5880.
6 C. H. Christensen, K. Johannsen, E. Törnqvist, I. Schmidt, H. Topsøe and C. H. Christensen, *Catal. Today*, 2007, **128**, 117.
7 K. Egeblad, C. H. Christensen, M. Kustova and C. H. Christensen, *Chem. Mater.*, 2008, **20**, 946.
8 M. E. Davis, C. Saldarriaga, C. Montes, J. Garces and C. Crowder, *Nature*, 1988, **331**, 698.
9 C. C. Freyhardt, M. Tsapatsis, R. F. Lobo, K. J. Balkus, Jr. and M. E. Davis, *Nature*, 1996, **381**, 295.
10 A. Corma, M. J. Diaz-Cabanas, J. L. Jorda, C. Martinez and M. Moliner, *Nature*, 2006, **443**, 842.
11 R. Simancas, D. Dari, N. Velamazán, M. T. Navarro, A. Cantín, J. L. Jordá, G. Sastre, A. Corma and F. Rey, *Science*, 2010, **26**, 1219.
12 L. Tosheva and V. Valtchev, *Chem. Mater.*, 2005, **17**, 2494.
13 R. Chal, C. Gerardin, M. Bulut and S. van Donk, *ChemCatChem*, 2011, **3**, 67.
14 X. Zhang, D. Liu, D. Xu, S. Asahina, K. A. Cychosz, K. V. Agrawal, Y. A. Wahedi, A. Bhan, S. A. Hashimi, O. Terasaki, M. Thommes and M. Tsapatsis, *Science*, 2012, **336**, 1684.
15 W. Chaikittisilp, Y. Suzuki, R. R. Mukti, T. Suzuki, K. Sugita, K. Itabashi, A. Shimojima and T. Okubo, *Angew. Chem.*, 2013, **125**, 3439.
16 H. Awala. J.-P. Gilson, R. Retoux, P. Boullay, J.-M. Goupil, V. Valtchev and S. Mintova, *Nat. Mater.*, 2015, **14**, 447.
17 R. Martínez-Franco, C. Paris, M. E. Martínez-Armero, C. Martínez, M. Moliner and A. Corma, *Chem. Sci.*, 2016, **7**, 102.
18 A. Corma, V. Fornes, S. B. Pergher, T. L. M. Maesen and J. G. Buglass, *Nature*, 1998, **396**, 353.
19 S. Maheshwari, E. Jordan, S. Kumar, F. S. Bates, R. L. Penn, D. F. Shantz and M. Tsapatsis, *J. Am. Chem. Soc.*, 2008, **130**, 1507.
20 D. P. Serrano, J. M. Escola and P. Pizarro, *Chem. Soc. Rev.*, 2013, **42**, 4004.
21 K. Na and G. A. Somorjai, *Catal. Lett.*, 2015, **145**, 193.
22 J. Mielby, J. O. Abildstrøm, F. Wang, T. Kasama, C. Weidenthaler and S. Kegnæs, *Angew. Chem., Int. Ed.*, 2014, **53**, 12513.
23 M. S. Holm, K. Egeblad, P. N. R. Vennestrøm, C. G. Hartmann, M. Kustova and C. H. Christensen, *Eur. J. Inorg. Chem.*, 2008, 5185.
24 P. N. R. Vennestrøm, M. Grill, M. Kustova, K. Egeblad, L. F. Lundegaard, F. Joensen, C. H. Christensen and P. Beato, *Catal. Today*, 2011, **168**, 71.
25 K. Na, M. Choi and R. Ryoo, *Microporous Mesoporous Mater.*, 2013, **166**, 3.
26 J. O. Abildstrøm, M. Kegnæs, G. Hytoft, J. Mielby and S. Kegnæs, *Microporous Mesoporous Mater.*, 2016, **225**, 232.
27 C. J. H. Jacobsen, C. Madsen, J. Houzvicka, I. Schmidt and A. Carlsson, *J. Am. Chem. Soc.*, 2000, **122**, 7116.
28 M. Yu. Kustova, P. Hasselriis and C. H. Christensen, *Catal. Lett.*, 2004, **96**, 205.
29 M. Kustova, K. Egeblad, K. Zhu and C. H. Christensen, *Chem. Mater.*, 2007, **19**, 2915.
30 K. Egeblad, M. Kustova, S. K. Klitgaard, K. Zhu and C. H. Christensen, *Microporous Mesoporous Mater.*, 2007, **101**, 214.
31 A. K. Rovik, S. K. Klitgaard, S. Dahl, C. H. Christensen and I. Chorkendorff, *Appl. Catal., A*, 2009, **358**, 269.
32 S. Takenaka, S. Kobayashi, H. Ogihara and K. Otsuka, *J. Catal.*, 2003, **217**, 79.
33 M. Yu. Kustova, A. L. Kustov and C. H. Christensen, *Stud. Surf. Sci. Catal.*, 2005, **158**, 255.
34 C. H. Christensen, K. Zhu, M. Kegnæs and K. Egeblad, *US Pat.*, 7824657, 2010.
35 C. N. Satterfield, *Heterogeneous Catalysis in Industrial Practice*, McGraw-Hill, New York, 2nd edn, 1991, p. 132.
36 I. Schmidt, C. Madsen and C. J. H. Jacobsen, *Inorg. Chem.*, 2000, **39**, 2279.

Bibliography

[1] J. N. Armor. A history of industrial catalysis. *Catalysis Today* **2011**, *163*, 3–9.

[2] D. Astruc, F. Lu, J. R. Aranzaes. Nanoparticles as recyclable catalysts: The frontier between homogeneous and heterogeneous catalysis. *Angewandte Chemie - International Edition* **2005**, *44*, 7852–7872.

[3] C. A. Witham, W. Huang, C.-K. Tsung, J. N. Kuhn, G. A. Somorjai, F. D. Toste. Converting homogeneous to heterogeneous in electrophilic catalysis using monodisperse metal nanoparticles. *Nature chemistry* **2010**, *2*, 36–41.

[4] M. Rose. Nanoporous polymers: Bridging the gap between molecular and solid catalysts? *ChemCatChem* **2014**, *6*, 1166–1182.

[5] F. Wang, J. Mielby, F. H. Richter, G. Wang, G. Prieto, T. Kasama, C. Weidenthaler, H. J. Bongard, S. Kegnæs, A. Fürstner, F. Schüth. A polyphenylene support for pd catalysts with exceptional catalytic activity. *Angewandte Chemie - International Edition* **2014**, *53*, 8645–8648.

[6] X. Li, J. Zhang, X. Zhao, Y. Zhao, F. Li, T. Li, D. Wang. Trace amount Pd(ppm)-catalyzed Sonogashira, Heck and Suzuki cross-coupling reactions based on synergistic interaction with an asymmetric conjugated pyridinespirofluorene. *Nanoscale* **2014**, *6*, 6473.

[7] M. Thommes, K. Kaneko, A. V. Neimark, J. P. Olivier, F. Rodriguez-reinoso, J. Rouquerol, K. S. W. Sing. Physisorption of gases , with special reference to the evaluation of surface area and pore size distribution (IUPAC Technical Report). *Pure Applied Chemistry* **2015**, *87*, 1051–1069.

[8] A. V. Neimark, K. S. W. Sing, M. Thommes, *Surface Area and Porosity* in *Handbook of Heterogeneous Catalysis*, Wiley-VCH Verlag GmbH & Co., **2008**, pp. 721–738.

[9] P. J. Goodhew, J. Humphreys, R. Beanland, *Electron Microscopy and Analysis 3rd ed.*, Taylor and Francis Books UK, **2001**.

[10] J. C. Yang, M. W. Small, R. V. Grieshaber, R. G. Nuzzo. Recent developments and applications of electron microscopy to heterogeneous catalysis. *Chemical Society Reviews* **2012**, *41*, 8179–8194.

[11] F. Castellino, S. B. Rasmussen, A. D. Jensen, J. E. Johnsson, R. Fehrmann. Deactivation of vanadia-based commercial SCR catalysts by polyphosphoric acids. *Applied Catalysis B: Environmental* **2008**, *83*, 110–122.

[12] J. Liu. Advanced electron microscopy characterization of nanostructured heterogeneous catalysts. *Microscopy and Microanalysis* **2004**, *10*, 55–76.

[13] M. E. Davis. Zeolites from a Materials Chemistry Perspective. *Chemistry of Materials* **2014**, *26*, 239–245.

[14] F. Di Renzo, F. Fajula, *Introduction to molecular sieves : trends of evolution of the zeolite community* in *Studies in Surface Science and Catalysis 157*, J. Čejka, H. van Bekkum (Eds.), Elsevier B.V, **2005**, chapter Introducti, pp. 1–12.

[15] B. Yilmaz, U. Müller. Catalytic Applications of Zeolites in Chemical Industry. *Topics in Catalysis* **2009**, *52*, 888–895.

[16] R. Rinaldi, F. Schüth. Design of solid catalysts for the conversion of biomass. *Energy & Environmental Science* **2009**, *2*, 610–626.

[17] A. Corma. From Microporous to Mesoporous Molecular Sieve Materials and Their Use in Catalysis. *Chemical reviews* **1997**, *97*, 2373–2420.

[18] R. Xu, W. Pang, J. Yu, Q. Huo, J. Chen, *Structural Chemistry of Microporous Materials* in *Chemistry of Zeolites and Related Porous Materials: Synthesis and Structure*, R. Xu, W. Pang, J. Yu, Q. Huo, J. Chen (Eds.), John Wiley & Sons, **2007**, chapter Structural.

[19] *International Zeolite Association*. http://www.iza-online.org.

[20] J. A. Lercher, A. Jentys, *Application of Microporous Solids as Catalysts* in *Handbook of Porous Solids*, *Vol. 2*, F. Schüth, K. S. W. Sing, J. Weitkamp (Eds.), Wiley-VCH Verlag GmbH & Co., Weinheim, **2002**, chapter Applicatio, pp. 1097–1156.

[21] R. J. Gorte, *Surface Acidity* in *Handbook of Porous Solids*, *Vol. 1*, F. Schüth, K. S. W. Sing, J. Weitkarnp (Eds.), Wiley-VCH Verlag GmbH & Co., Weinheim, **2002**, chapter Surface Ac, pp. 432–464.

[22] M. Elanany, M. Koyama, M. Kubo, E. Broclawik, A. Miyamoto. Periodic density functional investigation of Lewis acid sites in zeolites: relative strength order as revealed from NH 3 adsorption. *Applied Surface Science* **2005**, *246*, 96–101.

[23] B. Smit, T. L. M. Maesen. Towards a molecular understanding of shape selectivity. *Nature* **2008**, *451*, 671–678.

[24] P. B. Weisz. Molecular shape selective catalysis. *Pure Applied Chemistry* **1980**, *52*, 2091–2103.

[25] A. Corma, M. T. Navarro, F. Rey, J. Rius, S. Valencia. Pure polymorph C of zeolite beta synthesized by using framework isomorphous substitution as a structure-directing mechanism. *Angewandte Chemie - International Edition* **2001**, *40*, 2277–2280.

[26] E. Verheyen, L. Joos, K. V. Havenbergh, E. Breynaert, N. Kasian, E. Gobechiya, K. Houthoofd, C. Martineau, M. Hinterstein, F. Taulelle, V. V. Speybroeck, M. Waroquier, S. Bals, G. V. Tendeloo, C. E. A. Kirschhock, J. A. Martens. Design of zeolite by inverse sigma transformation. *Nature Materials* **2012**, *11*, 1059–1064.

[27] M. S. Holm, S. Saravanamurugan, E. Taarning. Conversion of Sugars to Lactic Acid Derivatives Using Heterogeneous Zeotype Catalysts. *Science* **2010**, *328*, 602–605.

[28] S. Bordiga, F. Bonino, A. Damin, C. Lamberti. Reactivity of Ti(iv) species hosted in TS-1 towards H2O2–H2O solutions investigated by ab initio cluster and periodic approaches combined with experimental XANES and EXAFS data: a review and new highlights. *Physical Chemistry Chemical Physics* **2007**, *9*, 4854–4878.

[29] G. N. Vayssilov. Structural and Physicochemical Features of Titanium Silicalites. *Catalysis Reviews* **1997**, *39*, 209–251.

[30] R. Saxton. Crystalline microporous titanium silicates. *Topics in Catalysis* **1999**, *9*, 43–57.

[31] M. Hartmann, G. Machoke, W. Schwieger, M. Hartmann. Catalytic Test Reactions for the Evaluation of Hierarchical Zeolites. *Chemical Society Reviews* **2016**, *45*, 3313–3330.

[32] K. Na, M. Choi, R. Ryoo. Recent advances in the synthesis of hierarchically nanoporous zeolites. *Microporous and Mesoporous Materials* **2013**, *166*, 3–19.

[33] J. Pérez-Ramírez, C. H. Christensen, K. Egeblad, C. H. Christensen, J. C. Groen. Hierarchical zeolites: Enhanced Utilisation of Microporous Crystals in Catalysis by Advances in Materials Design. *Chemical Society Reviews* **2008**, *37*, 2530–2542.

[34] L. Tosheva, V. P. Valtchev. Nanozeolites: Synthesis, Crystallization Mechanism, and Applications. *Chemistry of Materials* **2005**, *17*, 2494–2513.

[35] A. Corma, V. Fornes, S. B. Pergher, T. L. M. Maesen, J. G. Buglass. Delaminated zeolite precursors as selective acidic catalysts. *Nature* **1998**, *396*, 353–356.

[36] A. Sakthivel, S. J. Huang, W. H. Chen, Z. H. Lan, K. H. Chen, T. W. Kim, R. Ryoo, A. S. T. Chiang, S. B. Liu. Replication of mesoporous aluminosilicate molecular sieves (RMMs) with zeolite framework from mesoporous carbons (CMKs). *Chemistry of Materials* **2004**, *16*, 3168–3175.

[37] Y. Tao, H. Kanoh, K. Kaneko. {ZSM}-5 Monolith of Uniform Mesoporous Channels. *J. Am. Chem. Soc.* **2003**, *125*, 6044–6045.

[38] H. Katsuki, S. Furuta, T. Watari, S. Komarneni. ZSM-5 zeolite/porous carbon composite: Conventional- and microwave-hydrothermal synthesis from carbonized rice husk. *Microporous and Mesoporous Materials* **2005**, *86*, 145–151.

[39] J. García-Martínez, M. Johnson, J. Valla, K. Li, J. Y. Ying. Mesostructured zeolite Y—high hydrothermal stability and superior FCC catalytic performance. *Catalysis Science & Technology* **2012**, *2*, 987.

[40] K. Möller, T. Bein. Mesoporosity–a new dimension for zeolites. *Chemical Society reviews* **2013**, *42*, 3689–707.

[41] S. Mintova. Mechanism of Zeolite A Nanocrystal Growth from Colloids at Room Temperature. *Science* **1999**, *283*, 958–960.

[42] W. Xu, J. Dong, J. Li, J. Li, F. Wu. A Novel Method for the Preparation of Zeolite ZSM-5. *Journal of Chemical Society - Chemical Communications* **1990**, 755–756.

[43] M. Matsukata, T. Osaki, M. Ogura, E. Kikuchi. Crystallization behavior of zeolite beta during steam-assisted crystallization of dry gel. *Microporous and Mesoporous Materials* **2002**, *56*, 1–10.

[44] M. Matsukata, M. Ogura, T. Osaki, P. Raja, H. P. Rao, M. Nomura, E. Kikuchi. Conversion of dry gel to microporous crystals in gas phase. *Topics in Catalysis* **1999**, *9*, 77–92.

[45] C. Madsen, C. Madsen, C. J. H. Jacobsen. Nanosized zeolite crystals—convenient control of crystal size distribution by confined space synthesis. *Chemical Communications* **1999**, 673–674.

[46] I. Schmidt, C. Madsen, C. J. Jacobsen. Confined space synthesis. A novel route to nanosized zeolites. *Inorganic chemistry* **2000**, *39*, 2279–83.

[47] C. Jacobsen, C. Madsen. Mesoporous zeolite single crystals. *Journal of the American ...* **2000**, *122*, 7116–7117.

[48] C. J. H. Jacobsen, J. Houžvicka, A. Carlsson, I. Schmidt. Mesoporous zeolites. *Studies in Surface Science and Catalysis* **2001**, *135*, 167.

[49] Z. Wang, W. Fan, *Nanofabrication of Hierarchical Zeolites in Confined Space* in *Mesoporous Zeolites: Preparation, Characterization and Applications*, J. García-Martínez, K. Li (Eds.), Wiley-VCH Verlag GmbH & Co., **2015**, pp. 227–258.

[50] I. Schmidt, A. Boisen, E. Gustavsson, K. Ståhl, S. Pehrson, S. Dahl, A. Carlsson, C. J. H. Jacobsen. Carbon Nanotube Templated Growth of Mesoporous Zeolite Single Crystals. *American Chemical Society* **2000**, *13*, 4416 – 4418.

[51] A. H. Janssen, I. Schmidt, C. J. H. Jacobsen, A. J. Koster, K. P. de Jong. Exploratory study of mesopore templating with carbon during zeolite synthesis. *Microporous and Mesoporous Materials* **2003**, *65*, 59–75.

[52] K. Johannsen, A. Boisen, M. Brorson, I. Schmidt, C. J. Jacobsen. Preparation and characterization of mesoporous TS-1 catalyst. *Studies in Surface Science and Catalysis* **2002**, *142A*, 109–115.

[53] M. Y. Kustova, P. Hasselriis, C. H. Christensen. Mesoporous MEL-type zeolite single crystal catalysts. *Catalysis Letters* **2004**, *96*, 205–211.

[54] K. Egeblad, M. Kustova, S. K. Klitgaard, K. Zhu, C. H. Christensen. Mesoporous zeolite and zeotype single crystals synthesized in fluoride media. *Microporous and Mesoporous Materials* **2007**, *101*, 214–223.

[55] Y. Zhang, T. Okubo, M. Ogura. Synthesis of mesoporous aluminosilicate with zeolitic characteristics using vapor phase transport. *Chemical Communications* **2005**, 2719–2720.

[56] M. Ogura, Y. Zhang, S. P. Elangovan, T. Okubo. Formation of ZMM-n: The composite materials having both natures of zeolites and mesoporous silica materials. *Microporous and Mesoporous Materials* **2007**, *101*, 224–230.

[57] A. Dong, Y. Wang, Y. Tang, N. Ren, Y. Zhang, Z. Gao. Hollow zeolite capsules: A novel approach for fabrication and guest encapsulation. *Chemistry of Materials* **2002**, *14*, 3217–3219.

[58] A. G. Machoke, A. M. Beltrán, A. Inayat, B. Winter, T. Weissenberger, N. Kruse, R. Güttel, E. Spiecker, W. Schwieger. Micro/macroporous system: MFI-type zeolite crystals with embedded macropores. *Advanced Materials* **2015**, *27*, 1066–1070.

[59] S. Mintova, J.-P. Gilson, V. Valtchev. Advances in nanosized zeolites. *Nanoscale* **2013**, *5*, 6693–6703.

[60] R. Chal, C. Gérardin, M. Bulut, S. VanDonk. Overview and Industrial Assessment of Synthesis Strategies towards Zeolites with Mesopores. *ChemCatChem* **2011**, *3*, 67–81.

[61] M. Müller, G. Harvey, R. Prins. Comparison of the dealumination of zeolites beta, mordenite, ZSM-5 and ferrierite by thermal treatment, leaching with oxalic acid and treatment with SiCl4 by 1H, 29Si and 27A1 MAS NMR. *Microporous and Mesoporous Materials* **2000**, *34*, 135–147.

[62] a. H. Janssen, a. J. Koster, K. P. D. Jong. On the Shape of the Mesopores in Zeolite Y: A Three-Dimensional Transmission Electron Microscopy Study Combined with Texture Analysis. *J Phys Chem B* **2002**, *106*, 11905–11909.

[63] R. Giudici, H. W. Kouwenhoven, R. Prins. Comparison of nitric and oxalic acid in the dealumination of mordenite. *Applied Catalysis A: General* **2000**, *203*, 101–110.

[64] S. van Donk, A. H. Janssen, J. H. Bitter, K. P. de Jong. Generation, Characterization, and Impact of Mesopores in Zeolite Catalysts. *Catalysis Reviews* **2003**, *45*, 297–319.

[65] D. P. Serrano, J. M. Escola, P. Pizarro. Synthesis strategies in the search for hierarchical zeolites. *Chemical Society Reviews* **2013**, *42*, 4004–4035.

[66] J. A. Martens, P. A. Jacobs. Introduction to acid catalysis with zeolites in hydrocarbon reactions. *Introduction to Zeolite Science and Practice* **1991**, *58*, 445–496.

[67] P. Kortunov, S. Vasenkov, J. Kärger, R. Valiullin, P. Gottschalk, M. F. Elía, M. Perez, M. Stöcker, B. Drescher, G. McElhiney, C. Berger, R. Gläser, J. Weitkamp. The role of mesopores in intracrystalline transport in USY zeolite: PFG NMR diffusion study on various length scales. *Journal of the American Chemical Society* **2005**, *127*, 13055–13059.

[68] J. C. Groen, T. Bach, U. Ziese, A. M. Paulaime-Van Donk, K. P. De Jong, J. A. Moulijn, J. Pérez-Ramírez. Creation of hollow zeolite architectures by controlled desilication of A1-zoned ZSM-5 crystals. *Journal of the American Chemical Society* **2005**, *127*, 10792–10793.

[69] J. C. Groen, W. Zhu, S. Brouwer, S. J. Huynink, F. Kapteijn, J. A. Moulijn, J. Pérez-Ramírez. Direct demonstration of enhanced diffusion in mesoporous ZSM-5 zeolite obtained via controlled desilication. *Journal of the American Chemical Society* **2007**, *129*, 355–360.

[70] J. C. Groen, J. A. Moulijn, J. Pérez-Ramírez. Alkaline posttreatment of MFI zeolites. From accelerated screening to scale-up. *Industrial and Engineering Chemistry Research* **2007**, *46*, 4193–4201.

[71] J. C. Groen, J. C. Jansen, J. A. Moulijn, J. Pérez-Ramírez. Optimal aluminum-assisted mesoporosity development in MFI zeolites by desilication. *Journal of Physical Chemistry B* **2004**, *108*, 13062–13065.

[72] S. Abelló, A. Bonilla, J. Pérez-Ramírez. Mesoporous ZSM-5 zeolite catalysts prepared by desilication with organic hydroxides and comparison with NaOH leaching. *Applied Catalysis A: General* **2009**, *364*, 191–198.

[73] K. Li, J. Valla, J. Garcia-Martinez. Realizing the commercial potential of hierarchical zeolites: New opportunities in catalytic cracking. *ChemCatChem* **2014**, *6*, 46–66.

[74] J. Mielby, J. O. Abildstrøm, S. Pérez-Ferreras, S. B. Rasmussen, S. Kegnæs. Formation of pyridine N -oxides using mesoporous titanium silicalite-1. *Journal of porous materials* **2014**, *21*, 531–537.

[75] J. Datka, K. Tarach, K. Góra-Marek, *Acidic Properties of Hierarchical Zeolites* in *Mesoporous Zeolites: Preparation, Characterization and Applications*, J. García-Martínez, K. Li (Eds.), Wiley-VCH Verlag GmbH & Co., **2015**, pp. 461–496.

[76] J. Lee, U. G. Hong, S. Hwang, M. H. Youn, I. K. Song. Production of light olefins through catalytic cracking of C5 raffinate over carbon-templated ZSM-5. *Fuel Processing Technology* **2013**, *108*, 25–30.

[77] T. W. Ebbesen, P. M. Ajayan. Large-scale synthesis of carbon nanotubes. *Nature* **1992**, *358*, 220–222.

[78] T. Guo, P. Nikolaev, A. Thess, D. T. Colbert, R. E. Smalley. Catalytic growth of single-walled manotubes by laser vaporization. *Chemical Physics Letters* **1995**, *243*, 49–54.

[79] S. Amelinckx, X. B. Zhang, D. Bernaerts, X. F. Zhang, V. Ivanov, J. B. Nagy. A formation mechanism for catalytically grown helix-shaped graphite nanotubes. *Science* **1994**, *265*, 635–639.

[80] M. Perezcabero. Characterization of carbon nanotubes and carbon nanofibers prepared by catalytic decomposition of acetylene in a fluidized bed reactor. *Journal of Catalysis* **2003**, *215*, 305–316.

[81] Á. Kukovecz, Z. Kónya, N. Nagaraju, I. Willems, A. Tamási, A. Fonseca, J. B. Nagy, I. Kiricsi. Catalytic synthesis of carbon nanotubes over Co, Fe and Ni containing conventional and sol–gel silica–aluminas. *Physical Chemistry Chemical Physics* **2000**, *2*, 3071–3076.

[82] R. Sen, A. Govindaraj, C. Rao. Carbon nanotubes by the metallocene route. *Chemical Physics Letters* **1997**, *267*, 276–280.

[83] V. Ivanov, J. B. Nagy, P. Lambin, A. Lucas, X. B. Zhang, X. F. Zhang, D. Bernaerts, G. Van Tendeloo, S. Amelinckx, J. Van Landuyt. The study of carbon nanotubules produced by catalytic method. *Chemical Physics Letters* **1994**, *223*, 329–335.

[84] M. Yudasaka, R. Kikuchi, T. Matsui, Y. Ohki, S. Yoshimura, E. Ota. Specific conditions for Ni catalyzed carbon nanotube growth by chemical vapor deposition. *Applied Physics Letters* **1995**, *67*, 2477.

[85] A. M. Cassell, G. C. McCool, H. T. Ng, J. E. Koehne, B. Chen, J. Li, J. Han, M. Meyyappan. Carbon nanotube networks by chemical vapor deposition. *Applied Physics Letters* **2003**, *82*, 817–819.

[86] H. Dai, A. Rinzler, P. Nikolaev. Single-wall nanotubes produced by metal-catalyzed disproportionation of carbon monoxide. *Chemical Physics ...* **1996**, *4*.

[87] M. S. Holm, E. Taarning, K. Egeblad, C. H. Christensen. Catalysis with hierarchical zeolites. *Catalysis Today* **2011**, *168*, 3–16.

[88] C. H. Christensen, K. Zhu, M. Kegnæs, K. Egeblad, *FABRICATION OF HIERARCHICAL ZEOLITES*, **2010**.

[89] A. McDonald, B. Scott, G. Villemure. Hydrothermal preparation of nanotubular particles of a 1:1 nickel phyllosilicate. *Microporous and Mesoporous Materials* **2009**, *120*, 263–266.

[90] J. Park, H. Lee, J. Bang, K. Park, H. Song. Chemical transformation and morphology change of nickel-silica hybrid nanostructures via nickel phyllosilicates. *Chemical communications (Cambridge, England)* **2009**, 7345–7.

[91] S. Goel, K. K. Pant, K. D. P. Nigam. Extraction of nickel from spent catalyst using fresh and recovered EDTA. *Journal of Hazardous Materials* **2009**, *171*, 253–261.

[92] X. Meng, F. Nawaz, F. S. Xiao, *Templating route for synthesizing mesoporous zeolites with improved catalytic properties*, **2009**.

[93] K. Lascelles, L. G. Morga, D. Nicholls, D. Beyersmann, *Nickel Compounds* in *Ullmann's Encyclopedia of Industrial Chemistry*, Wiley-VCH Verlag GmbH & Co., Weinheim, **2005**, pp. Vol 24. 177–223.

[94] J. Pérez-Ramírez, D. Verboekend, A. Bonilla, S. Abelló. Zeolite Catalysts with Tunable Hierarchy Factor by Pore-Growth Moderators. *Advanced Functional Materials* **2009**, *19*, 3972–3979.

[95] F. Schmidt, S. Paasch, E. Brunner, S. Kaskel. Carbon templated SAPO-34 with improved adsorption kinetics and catalytic performance in the MTO-reaction. *Microporous and Mesoporous Materials* **2012**, *164*, 214–221.

[96] R. Schlögl. The role of chemistry in the energy challenge. *ChemSusChem* **2010**, *3*, 209–222.

[97] H. A. Gasteiger, S. S. Kocha, B. Sompalli, F. T. Wagner. Activity benchmarks and requirements for Pt, Pt-alloy, and non-Pt oxygen reduction catalysts for PEMFCs. *Applied Catalysis B: Environmental* **2005**, *56*, 9–35.

[98] H. A. Gasteiger, N. M. Marković. Just a Dream - Or Future Reality? *Science* **2009**, *324*, 48.

[99] A. Rabis, P. Rodriguez, T. J. Schmidt. Electrocatalysis for Polymer Electrolyte Fuel Cells : Recent Achievements and Future Challenges. *ACS Catal.* **2012**, *2*, 864–890.

[100] H. A. Gasteiger, J. Garche, *Fuel Cells* in *Handbook of Heterogeneous Catalysts*, Wiley-VCH Verlag GmbH & Co., **2008**, chapter Fuel Cells, pp. 3081–3121.

[101] C. Song, J. Zhang, *Electrocatalytic Oxygen Reduction Reaction* in *PEM Fuel Cell Electrocatalysts and Catalyst Layers SE - 2*, Springer, **2008**, pp. 89–134.

[102] X. Yu, P. G. Pickup. Recent advances in direct formic acid fuel cells (DFAFC). *Journal of Power Sources* **2008**, *182*, 124–132.

[103] R. Kothari, D. Buddhi, R. L. Sawhney. Comparison of environmental and economic aspects of various hydrogen production methods. *Renewable and Sustainable Energy Reviews* **2008**, *12*, 553–563.

[104] D. Teichmann, W. Arlt, P. Wasserscheid, R. Freymann. A future energy supply based on Liquid Organic Hydrogen Carriers (LOHC). *Energy & Environmental Science* **2011**, *4*, 2767.

[105] E. Gyenge, *Electrocatalytic Oxidation of Methanol, Ethanol and Formic Acid* in *PEM Fuel Cell Electrocatalysis and Catalyst Layers*, J. Zhang (Ed.), Springer, **2008**, pp. 165–285.

[106] Y. Zhu, S. Y. Ha, R. I. Masel. High power density direct formic acid fuel cells. *Journal of Power Sources* **2004**, *130*, 8–14.

[107] R. Borup, J. P. Meyers, B. Pivovar, Y. S. Kim, R. Mukundan, N. Garland, D. Myers, M. Wilson, F. Garzon, D. Wood, P. Zelenay, K. More, K. Stroh, T. Zawodzinski, X. J. Boncella, J. E. Mcgrath, J. Meyers, J. E. Mcgrath, K. Miyatake, M. Hori, K. Ota, Z. Ogumi, S. Miyata, A. Nishikata, Z. Siroma, Y. Uchimoto, K. Yasuda, K.-i. Kimijima, N. Iwashita. Scientific Aspects of Polymer Electrolyte Fuel Cell Durability and Degradation . *Chemical reviews* **2007**, *107*, 3904–3951.

[108] M. M. Mensch, E. C. Kumbur, T. N. Veziroglu, *Electrochemical Degradation: Electrocatalyst and Support Durability* in *Polymer Electrolyte Fuel Cell Degradation*, Academic Press, **2012**, pp. 89–214.

[109] J. C. Meier, C. Galeano, I. Katsounaros, A. A. Topalov, A. Kostka, F. Schüth, K. J. J. Mayrhofer. Degradation mechanisms of Pt/C fuel cell catalysts under simulated start-stop conditions. *ACS Catalysis* **2012**, *2*, 832–843.

[110] A. Zana, J. Speder, M. Roefzaad, L. Altmann, M. Baumer, M. Arenz. Probing Degradation by IL-TEM: The Influence of Stress Test Conditions on the Degradation Mechanism. *Journal of the Electrochemical Society* **2013**, *160*, F608.

[111] S. Zhang, X. Z. Yuan, J. N. C. Hin, H. Wang, J. Wu, K. A. Friedrich, M. Schulze. Effects of open-circuit operation on membrane and catalyst layer degradation in proton exchange membrane fuel cells. *Journal of Power Sources* **2010**, *195*, 1142–1148.

[112] Y. Shao, G. Yin, Y. Gao. Understanding and approaches for the durability issues of Pt-based catalysts for PEM fuel cell. *Journal of Power Sources* **2007**, *171*, 558–566.

[113] J. C. Meier, C. Galeano, I. Katsounaros, J. Witte, H. J. Bongard, A. A. Topalov, C. Baldizzone, S. Mezzavilla, F. Schüth, K. J. J. Mayrhofer. Design criteria for stable Pt/C fuel cell catalysts. *Beilstein Journal of Nanotechnology* **2014**, *5*, 44–67.

[114] S. Mukerjee, S. Srinivasan, *Handbook of Fuel Cells-Fundamentals, Technology and Applications*, Wiley and Sons, Chichester, **2003**.

[115] P. J. Ferreira, G. J. la O', Y. Shao-Horn, D. Morgan, R. Makharia, S. Kocha, H. A. Gasteiger. Instability of Pt/C Electrocatalysts in Proton Exchange Membrane Fuel Cells. *Journal of The Electrochemical Society* **2005**, *152*, A2256.

[116] Y. Shao-Horn, P. Ferreira, G. la O', D. Morgan, H. A. Gasteiger, R. Makharia, *Coarsening of Pt Nanoparticles in Proton Exchange Membrane Fuel Cells upon Potential Cycling* in *ECS Transactions*, pp. 185–195. http://www.scopus.com/inward/record.url?eid=2-s2.0-33845268204{&}partnerID=tZOtx3y1.

[117] Y. Shao-Horn, W. C. Sheng, S. Chen, P. J. Ferreira, E. F. Holby, D. Morgan. Instability of supported platinum nanoparticles in low-temperature fuel cells. *Topics in Catalysis* **2007**, *46*, 285–305.

[118] W. Sheng, S. Chen, E. Vescovo, Y. Shao-Horn. Size Influence on the Oxygen Reduction Reaction Activity and Instability of Supported Pt Nanoparticles. *Journal of The Electrochemical Society* **2012**, *159*, 96–103.

[119] K. Schlögl, K. J. J. Mayrhofer, M. Hanzlik, M. Arenz. Identical-location TEM investigations of Pt/C electrocatalyst degradation at elevated temperatures. *Journal of Electroanalytical Chemistry* **2011**, *662*, 355–360.

[120] K. Schlögl, M. Hanzlik, M. Arenz. Comparative IL-TEM Study Concerning the Degradation of Carbon Supported Pt-Based Electrocatalysts. *Journal of The Electrochemical Society* **2012**, *159*, B677.

[121] T. W. Hansen, A. T. Delariva, S. R. Challa, A. K. Datye. Sintering of catalytic nanoparticles: particle migration or ostwald ripening? *Accounts of chemical research* **2013**, *46*, 1720–30.

[122] K. J. J. Mayrhofer, J. C. Meier, S. J. Ashton, G. K. H. Wiberg, F. Kraus, M. Hanzlik, M. Arenz. Fuel cell catalyst degradation on the nanoscale. *Electrochemistry Communications* **2008**, *10*, 1144–1147.

[123] K. J. J. Mayrhofer, S. J. Ashton, J. C. Meier, G. K. H. Wiberg, M. Hanzlik, M. Arenz. Non-destructive transmission electron microscopy study of catalyst degradation under electrochemical treatment. *Journal of Power Sources* **2008**, *185*, 734–739.

[124] K. Hartl, M. Hanzlik, M. Arenz. IL-TEM investigations on the degradation mechanism of Pt/C electrocatalysts with different carbon supports. *Energy & Environmental Science* **2011**, *4*, 234–238.

[125] N. Linse, L. Gubler, G. G. Scherer, A. Wokaun. The effect of platinum on carbon corrosion behavior in polymer electrolyte fuel cells. *Electrochimica Acta* **2011**, *56*, 7541–7549.

[126] A. P. Young, J. Stumper, E. Gyenge. Characterizing the Structural Degradation in a PEMFC Cathode Catalyst Layer: Carbon Corrosion. *Journal of The Electrochemical Society* **2009**, *156*, B913–B922.

[127] P. T. Yu, W. Gu, J. Zhang, R. Makharia, F. T. Wagner, H. A. Gasteiger, *Carbon-support requirements for highly durable fuel cell operation* in *Polymer Electrolyte Fuel Cell Durability*, F. N. Buechi, M. Inaba, T. J. Schmidt (Eds.), Springer, **2009**, pp. 29–53.

[128] H. Schulenburg, B. Schwanitz. 3D imaging of catalyst support corrosion in polymer electrolyte fuel cells. *The Journal of Physical Chemistry C* **2011**, *115*, 14236–14243.

[129] G. A. Gruver. The corrosion of carbon black in phosphoric acid. *J. Electrochem. Soc.* **1978**, *125*, 1719–1720.

[130] J. Greeley, I. E. L. Stephens, A. S. Bondarenko, T. P. Johansson, H. A. Hansen, J. T. F., J. Rossmeisl, I. Chorkendorff, J. K. Nørskov. Alloys of platinum and early transition metals as oxygen reduction electrocatalysts. *Nat. Chem.* **2009**, *1*, 552–556.

[131] M. Lefevre, E. Proietti, F. Jaouen, J. P. Dodelet. Iron-based catalysts with improved oxygen reduction activity in polymer electrolyte fuel cells. *Science* **2009**, *324*, 71–74.

[132] G. Prieto, H. Tüysüz, N. Duyckaerts, J. Knossalla, G.-H. Wang, F. Schüth. Hollow Nano- and Microstructures as Catalysts. *Chemical Reviews* **2016**, acs.chemrev.6b00374.

[133] L. de Rogatis, M. Cargnello, V. Gombac, B. Lorenzut, T. Montini, P. Fornasiero. Embedded phases: A way to active and stable catalysts. *ChemSusChem* **2010**, *3*, 24–42.

[134] G. D. Li, Z. Y. Tang. Noble metal nanoparticle@metal oxide core/yolk-shell nanostructures as catalysts: recent progress and perspective. *Nanoscale* **2014**, *6*, 3995–4011.

[135] C. Galeano, C. Baldizzone, H. Bongard, B. Spliethoff, C. Weidenthaler, J. C. Meier, K. J. J. Mayrhofer, F. Schüth. Carbon-based yolk-shell materials for fuel cell applications. *Advanced Functional Materials* **2014**, *24*, 220–232.

[136] L. Qu, Y. Liu, J. Baek, L. Dai. Nitrogen-doped graphene as efficient metal-free electrocatalyst for oxygen reduction in fuel cells. *ACS Nano* **2010**, *4*, 1321–1326.

[137] H. Wang, T. Maiyalagan, X. Wang. Review on recent progress in nitrogen-doped graphene: Synthesis, characterization, and its potential applications. *ACS Catalysis* **2012**, *2*, 781–794.

[138] Y. Guo, J. He, T. Wang, H. Xue, Y. Hu, G. Li, J. Tang, X. Sun. Enhanced electrocatalytic activity of platinum supported on nitrogen modified ordered mesoporous carbon. *Journal of Power Sources* **2011**, *196*, 9299–9307.

[139] Y. Zhou, K. Neyerlin, T. S. Olson, S. Pylypenko, J. Bult, H. N. Dinh, T. Gennett, Z. Shao, R. O'Hayre. Enhancement of Pt and Pt-alloy fuel cell catalyst activity and durability via nitrogen-modified carbon supports. *Energy & Environmental Science* **2010**, *3*, 1437.

[140] Y. Zhou, R. Pasquarelli, T. Holme, J. Berry, D. Ginley, R. O'Hayre. Improving PEM fuel cell catalyst activity and durability using nitrogen-doped carbon supports: observations from model Pt/HOPG systems. *Journal of Materials Chemistry* **2009**, *19*, 7830.

[141] P. Pachfule, V. M. Dhavale, S. Kandambeth, S. Kurungot, R. Banerjee. Porous-organic-framework-templated nitrogen-rich porous carbon as a more proficient electrocatalyst than Pt/C for the electrochemical reduction of oxygen. *Chemistry - A European Journal* **2013**, *19*, 974–980.

[142] D. B. Kim, D. H. Lim, H. J. Chun, H. H. Kwon, H. I. Lee. Nitrogen-containing graphitized carbon support for methanol oxidation Pt catalyst. *Carbon* **2010**, *48*, 673–679.

[143] F. Su, X. S. Zhao, Y. Wang, L. Wang, J. Y. Lee. Hollow carbon spheres with a controllable shell structure. *Journal of Materials Chemistry* **2006**, *16*, 4413.

[144] M. Chisaka, T. Iijima, A. Tomita, T. Yaguchi, Y. Sakurai. Oxygen Reduction Reaction Activity of Vulcan XC-72 Doped with Nitrogen under NH[sub 3] Gas in Acid Media. *Journal of The Electrochemical Society* **2010**, *157*, B1701.

[145] S. Maldonado, S. Morin, K. J. Stevenson. Structure, composition, and chemical reactivity of carbon nanotubes by selective nitrogen doping. *Carbon* **2006**, *44*, 1429–1437.

[146] S. Pylypenko, S. Mukherjee, T. S. Olson, P. Atanassov. Non-platinum oxygen reduction electrocatalysts based on pyrolyzed transition metal macrocycles. *Electrochimica Acta* **2008**, *53*, 7875–7883.

[147] C. L. Sun, L. C. Chen, M. C. Su, L. S. Hong, O. Chyan, C. Y. Hsu, K. H. Chen, T. F. Chang, L. Chang. Ultrarine platinum nanoparticles uniformly dispersed on arrayed CNx nanotubes with high electrochemical activity. *Chemistry of Materials* **2005**, *17*, 3749–3753.

[148] S. Pylypenko, A. Borisevich, K. L. More, A. Corpuz, T. Holme, A. Dameron, T. Olson, H. Dinh, T. Gennett, R. O'Hayre. Nitrogen: Unraveling the secret to stable carbon-supported Pt-alloy electrocatalysts. *Energy & Environmental Science* **2013**, *6*.

[149] K. N. Wood, R. O'Hayre, S. Pylypenko. Recent progress on nitrogen/carbon structures designed for use in energy and sustainability applications. *Energy & Environmental Science* **2014**, *7*, 1212.

[150] Y. Shao, J. Sui, G. Yin, Y. Gao. Nitrogen-doped carbon nanostructures and their composites as catalytic materials for proton exchange membrane fuel cell. *Applied Catalysis B: Environmental* **2008**, *79*, 89–99.

[151] M. Sevilla, A. B. Fuertes. Catalytic graphitization of templated mesoporous carbons. *Carbon* **2006**, *44*, 468–474.

[152] C. Galeano, J. C. Meier, V. Peinecke, H. Bongard, I. Katsounaros, A. A. Topalov, A. Lu, K. J. J. Mayrhofer, F. Schüth. Toward highly stable electrocatalysts via nanoparticle pore confinement. *Journal of the American Chemical Society* **2012**, *134*, 20457–20465.

[153] B. Y. Xia, J. N. Wang, S. J. Teng, X. X. Wang. Durability improvement of a Pt catalyst with the use of a graphitic carbon support. *Chemistry - A European Journal* **2010**, *16*, 8268–8274.

[154] M. K. Debe. Electrocatalyst approaches and challenges for automotive fuel cells. *Nature* **2012**, *486*, 43–51.

[155] P. C. K. Vesborg, T. F. Jaramillo. Addressing the terawatt challenge: scalability in the supply of chemical elements for renewable energy. *RSC Advances* **2012**, *2*, 7933.

[156] Y. J. Wang, N. Zhao, B. Fang, H. Li, X. T. Bi, H. Wang. Carbon-Supported Pt-Based Alloy Electrocatalysts for the Oxygen Reduction Reaction in Polymer Electrolyte Membrane Fuel Cells: Particle Size, Shape, and Composition Manipulation and Their Impact to Activity. *Chemical Reviews* **2015**, *115*, 3433–3467.

[157] J. Knossalla, S. Mezzavilla, F. Schüth. Continuous synthesis of nanostructured silica based materials in a gas–liquid segmented flow tubular reactor. *New J. Chem.* **2016**, *40*, 4361–4366.

[158] T. Zhang, H. Zhao, S. He, K. Liu, H. Liu, Y. Yin, C. Gao. Unconventional route to encapsulated ultrasmall gold nanoparticles for high-temperature catalysis. *ACS Nano* **2014**, *8*, 7297–7304.

[159] J. Górka, A. Zawislak, J. Choma, M. Jaroniec. KOH activation of mesoporous carbons obtained by soft-templating. *Carbon* **2008**, *46*, 1159–1161.

[160] J. Wang, S. Kaskel. KOH activation of carbon-based materials for energy storage. *Journal of Materials Chemistry* **2012**, *22*, 23710.

[161] E. Raymundo-Piñero, P. Azaïs, T. Cacciaguerra, D. Cazorla-Amorós, A. Linares-Solano, F. Béguin. KOH and NaOH activation mechanisms of multiwalled carbon nanotubes with different structural organisation. *Carbon* **2005**, *43*, 786–795.

[162] M. Zhou, F. Pu, Z. Wang, S. Guan. Nitrogen-doped porous carbons through KOH activation with superior performance in supercapacitors. *Carbon* **2014**, *68*, 185–194.

[163] S. Maldonado, K. J. Stevenson. Influence of nitrogen doping on oxygen reduction electrocatalysis at carbon nanofiber electrodes. *Journal of Physical Chemistry B* **2005**, *109*, 4707–4716.

[164] F. Su, Z. Tian, C. K. Poh, Z. Wang, S. H. Lim, Z. Liu, J. Lin. Pt nanoparticles supported on nitrogen-doped porous carbon nanospheres as an electrocatalyst for fuel cells. *Chemistry of Materials* **2010**, *22*, 832–839.

[165] C. Weidenthaler. Pitfalls in the characterization of nanoporous and nanosized materials. *Nanoscale* **2011**, *3*, 792–810.

[166] Z. L. Liu, X. H. Lin, J. Y. Lee, W. Zhang, M. Han, L. M. Gan. Preparation and characterization of platinum-based electrocatalysts on multiwalled carbon nanotubes for proton exchange membrane fuel cells. *Langmuir* **2002**, *18*, 4054–4060.

[167] M. Neurock, M. Janik, A. Wieckowski. A first principles comparison of the mechanism and site requirements for the electrocatalytic oxidation of methanol and formic acid over Pt. *Faraday Discuss.* **2008**, *140*, 363–378.

DTU Chemistry
Department of Chemistry
Technical University of Denmark

Kemitorvet, Building 206
2800 Kgs. Lyngby
Tlf. +45 45 25 24 19

www.kemi.dtu.dk/english